Queen Mary
University of London

Organo-Sensitised Erbium System for Optical Amplification at Telecommunication Wavelength.

Ye, Huanqing

The copyright of this thesis rests with the author and no quotation from it or information derived from it may be published without the prior written consent of the author

For additional information about this publication click this link.
http://qmro.qmul.ac.uk/jspui/handle/123456789/9079

Information about this research object was correct at the time of download; we occasionally make corrections to records, please therefore check the published record when citing. For more information contact scholarlycommunications@qmul.ac.uk

Organo-Sensitised Erbium System for Optical Amplification at Telecommunication Wavelength

Huanqing Ye

School of Physics and Astronomy

Queen Mary, University of London

Supervisors – Dr. Ignacio Hernández, Prof. William Gillin

Thesis submitted to the University of London for the Degree of Doctor of Philosophy

2014

Declaration

All the work contained within this thesis is my own and has not previously been submitted to satisfy any of other degree requirements at this or any other university. This thesis contains no material published or written by another person except where due reference is made in this thesis itself.

Huanqing Ye

Imagination is more important than knowledge, for knowledge is limited while imagination embraces the entire world, pushes improvement and is the source of knowledge evolution

Albert Einstein

Acknowledgement

My first great appreciation is to my parents, Jun Ye and Yujian Huan, who have been patient, supportive and generally good instructors in life. Particularly, I thank my wife, Jiayuan Tian, who has been absolutely supportive and offering me unconditional love all these years.

Secondly, I would express my genuine gratitude to my supervisors, Prof. William Gillin and Dr. Ignacio Hernández. They have invested a significant amount of time in providing me with patient, sufficient and constructive guidance in my Ph.D education. I appreciate even more and have benefitted from their generosity, forgiveness (for the foolishness I sometimes displayed), open minds, enthusiasm and rigorous attitude towards science.

Thanks also go to Dr. Peter Wyatt for his patient and rigorous support in any piece of chemistry. Many thanks go to the members in my research group: Dr. Zhe Li and Yu Peng from Chemistry, they are my best colleagues and friends, and I learnt many interesting points of chemistry from them. Many thanks also to Dr. Filippo Boi and Dr. Maureen William. They were so generous, helpful and shared not only in my research but also in exchanging different points of culture. There are too many academic and research staff in the CCMP group to list, but I would particularly like to thank Prof. David Dunstan, the smartest person I have met, Prof. Martin Dove, the big daddy, Dr. Theo Kreouzis, friendly and cool, and Dr. Andrei

Sapelkin. Mr. Geoff Gannaway deserves great thanks for his patience in technique support and instruction. I would also gratefully thank Dr. Pratik Desai, Dr. Ken Scott and Dr. Phil Baker, who taught me, instructed me and worked with me. In addition, I would thank all the professional and teaching staff in the school: Ms Sarah Cowls, Dr. Terry Arter, Ms Kathy Boydon, Miss Jessica Hnery, Ms Jazmina Moura, Dr. Yiannis Tsapras, to name a few.

Many thanks to all the students in the CCMP group: Carlos Aristizabal, Will Little, David Holford, Min Gao, Hongtao Zhang, Shuo Han, Hang Gu, Haizhou Lu, Mingying Song, Yiwei Sun, Jianxu Hu, Ke Wang, Chenxing Yang, Wenda Shi, Tingting Zhang. Thank you for enabling me to have a good time both in the office and laboratory.

Table of Contents

List of Publications

1: “Organo-erbium systems for optical amplification at telecommunications wavelengths”, H.Q. Ye, Z. Li, Y. Peng, C.C. Wang, T.Y. Li, Y.X. Zheng, A. Sapelkin, G. Adamopoulos, I. Hernández, P.B. Wyatt and W.P. Gillin, *Nature Materials*, **2014**, *13*(4), pp 382-386.

2: “Effect of Fluorination on the Radiative Properties of Er^{3+} Organic Complexes: An Opto-Structural Correlation Study”, H.-Q. Ye, Y. Peng, Z. Li, C.-C. Wang, Y.-X. Zheng, M. Motevalli, P.B. Wyatt, W.P. Gillin and I. Hernández, *J. Phys. Chem. C*, **2013**, *117*(45), pp 23970-23975.

3: “Visible-Range Sensitization of Er^{3+}-Based Infrared Emission from Perfluorinated 2-Acylphenoxide Complexes”, Yu Peng, Huanqing Ye, Zhe Li, Majid Motevalli, Ignacio Hernández, William P. Gillin and Peter B. Wyatt, *The Journal of Physical Chemistry Letters*, **2014**, *5*(9), pp 1560-1563.

4: “Luminescent Zinc (II) Complexes of Fluorinated Benzothiazol-2-yl Substituted Phenoxide and Enolate Ligands”, Zhe Li, Ahmed Dellali, Jahangir Malik, Majid Motevalli, Roger M. Nix, Toyin Olukoya, Yu Peng, Huanqing Ye, William P. Gillin, Ignacio Hernández and Peter B. Wyatt, *Inorg. Chem.*, **2013**, 52(3), pp 1379-1387.

Abstract

The erbium-based optical amplifier (EDFA) plays a vital role in the global fibre-optic telecommunication network. However, there are two main issues with current EDFAs, their bulky size means that they cannot be integrated into silicon-based photonic devices, and they need high pump power to produce optical gain. Here, a potential organo-erbium gain system has been invented, which could be operated under a low pump power and integrated onto a silicon-based device. The fully-fluorinated organic erbium complex [$Er(ftpip)_3$] was mixed with a fully-fluorinated organic zinc complex [$Zn(F\text{-}BTZ)_2$], acting as a chromophore over the visible range. The composite provides extraordinary sensitisation from the $Zn(F\text{-}BTZ)_2$ to $Er(ftpip)_3$ over a broad-visible band, which is compatible with high power LEDs, whilst the erbium ions have a new record of IR emission lifetime of ~ 0.8 ms (quantum yield = ~ 7%). The integrated sensitisation is ~ 10^4 times that of the intrinsic excitation into erbium. This system has been integrated into an organic light emitting diodes (OLEDs) demonstrating that the energy transfer is dominated by triplet states of the $Zn(F\text{-}BTZ)_2$. This is used for explaining the photoluminescence saturation and large pump-rate, with the composite being excited by a low power diode laser on the chromophore units. This composite-system was used to fabricate a slab waveguide, in which an relative gain of 3.4 dB/cm was achieved when

excited by a diode laser with 3 mW. A microscopic-optic setup was designed to measure IR line strengths of erbium ions in crystals of complexes, which were included in theoretical calculation to obtain accurate quantum yield for IR emission of erbium ions. The inclusion of IR line strengths measured from crystals is found to be crucial for Judd-Ofelt parameterisation on organic erbium complexes. It was demonstrated that fluorination could increase the line strengths of hypersensitive transitions and IR transition for 1.5 μm band.

Introduction

The background and challenge

After more than a century of development in the telecommunication industry, modern telecommunication networks are now based around a worldwide backbone of fibre-optic cables that encircle the globe carrying data at the speed of light. The robust growth in connectivity and demand for speed, and continuing innovation in devices and services are among the trends facing the fibre-optic telecommunication industry in the coming years. Fibre-optic communication is a method for transmitting information from one place to another by sending light pulses through an optical fibre. In a typical optical fibre, the signal travelling in the fibre suffers from various losses, such as fibre attenuation losses etc. The early optical fibre in the 1980s operated at 850 nm wavelength, which is the so-called “first window” in silica-based fibre. This window refers to a wavelength region that offers low optical loss. As the technology progressed, the first window became less attractive because of its relative high 3 dB/km loss limit. Then, most companies jumped to the “second window” at ~ 1.3 μm with lower attenuation of ~ 0.5 dB/km. Today, the “third window” at ~ 1.5 μm has become the most attractive because it has the minimum optical loss of ~ 0.2 dB/km for modern silica-based fibres.[1-3] However, over a long distance, despite the wide success of low-loss optical fibres, it is still necessary to

regularly amplifier the optical signals. A key enabler of cost-effective optical amplifier was the development of the erbium-doped fibre amplifier (EDFA). Prior to the development of EFDAs, expensive electronic amplifiers were used to regenerate the optical signals at roughly 40 km intervals and they were limited by the speed of electronic components.[4] In contrast, early EDFAs allowed optical signals to transmit over 500 km before needing to be regenerated, and current EDFAs have increased the distance to 1,500 - 2,500 km with ultra long-haul dense wavelength division multiplexing (DWDM) systems.[2, 3]

The performance of EDFA relies on the photo-physical characteristic of erbium (Er^{3+}) ions, conventionally doped in glass matrixes.[1,4] The Er^{3+} ion, one of the lanthanide ions, has an intrinsic emission at ~ 1.5 μm band compatible with the "third window", and long emission lifetime (~ 10 ms) that means the population inversion of Er^{3+} ions is easier to achieve. So, the erbium-doped glass fibre is suitable for optical amplification[4-7]. However, the absorption coefficient of Er^{3+} ions is low due to its electronic transitions are theoretically forbidden, thus, a powerful laser must be coaxially launched into erbium doped fibres of 10 - 30 m length along with the optical signals in order to achieve population inversion and, thus optical gain.[8] Typically, 980 nm or 1480 nm lasers are used to pump EDFAs, and the power density of the laser can be up to ~ kW/cm^2, though the pump power efficiency can be ~ 75%.[4] These features make EDFAs often bulky

and relative expensive, and not suitable for implanting them into integrated optic devices.[6]

The optical properties of erbium-based amplifiers, in principle, can be boosted by incorporating Er^{3+} ions into organic hosts containing chromophores providing strong and broad optical absorption. These organic chromophores can be coordinated with Er^{3+} ions acting as light harvesting chemical groups, which allow for pumping with lower intensity sources, such as light emitting diodes (LEDs), and amplification at shorter wavelengths.[5,6] This process is called the sensitisation effect or the antenna effect.

However, the attempts to exploit this idea have been hampered because most coordinated organic ligands contain hydrogenated chemical bonds, such as C-H, O-H and N-H bonds, which dramatically quench the infrared (IR) emission of Er^{3+} ions, since some vibrational energy levels of these hydrogenated bonds match the energy of ~ 1.5 μm emission.[9,10] This quenching results in poor quantum efficiencies and photoluminescence (PL) lifetimes orders of magnitude smaller than those required. In the chemical view, replacing hydrogens with heavier halogens, such as F, Cl or Br, is an attempt to reduce the quenching from hydrogenated chemical bonds because their vibrational energy levels mismatch the energy of ~ 1.5 μm emission. Some reported fully fluorinated organic erbium complexes can extend the PL lifetimes of ~ 1.5 μm emission up to hundreds of

microseconds, compared to the PL lifetimes for some hydrogenated organic erbium complexes of just nanoseconds.[10,11]

However, many fluorinated-organic erbium complexes are not thermally stable due to the large electronegativity of fluorination,[15,16] and some fully fluorinated-organic erbium complexes only have some sensitisation effect over short ultra-violet (UV) wavelengths (< 280 nm) without any visible sensitisation effect.[11-13] On the other hand, some quantitative reports of the sensitisation effect for fluorinated organic erbium complexes over visible bands are just a fact of 5, which barely contributes to enhancing the optical properties of Er^{3+} ions, due to the low conjugation level of organic ligands.[14,15]

Moreover, it is believed that the sensitisation effect is mainly attributed to the energy transfer process between the triplet states of organics and the electronic states of lanthanide ions,[16-20] however, there is no experimentally observation of the energy transfer process. Also, the quantum yields of Er^{3+} ions are usually referred to an averaged value derived from one work based on time-dependence study of erbium (III) tris(8-hydroxyquinolate) near-IR PL,[11,21] but there is no method to calculate a specific quantum yield of an organic erbium complex considering specific hosts and molecular structures.

Scope of the project and preliminary strategy

Some fluorinated erbium complexes are derived from the corresponding hydrogenated erbium complexes by replacing hydrogen on organic ligands by fluorine. In order to demonstrate the influence of fluorination on the transitions and electronic configurations of coordinated Er^{3+} ions, some experiments, such as absorption measurement and X-ray diffraction (XRD) measurements, can be comparatively performed on fluorinated erbium complexes and their corresponding hydrogenated erbium complexes, since they could have similarity, such as Er-O, bond lengths and similar molecular structures. In this project, analyses of the absorption spectra, over the full UV-visible-IR band, of fluorinated erbium complexes and their corresponding hydrogenated erbium complexes in the solid state will be undertaken to fit a semi-empirical Judd-Ofelt theory, in order to understand the oscillator strengths of the electronic transitions in each erbium complex. This then allows for providing precise quantum efficiencies of Er^{3+} ions and investigating some correlations between the molecular structures and electronic transitions.

More importantly, in this project, instead of searching for a good visible sensitised fluorinated erbium complex, a novel approach is taken to separate a thermally stable fluorinated organic chromophore, which has strong absorption over visible bands, from a thermally stable-chemical environment for a fluorinated erbium complex with a long emission

lifetime. The organic chromophore and fluorinated erbium complex can be sublimated, and the mixture of these two complexes as thin films is performed via a co-evaporation technique under vacuum. One achievement for this technique is that an extraordinary sensitisation effect over a broad visible band for the Er^{3+} ions and a new record of quantum efficiency are identified in this system. Moreover, owing to the achievement of the sensitization effect, the vacuum evaporation technique is also used to fabricate a slab waveguide containing the mixed system in order to demonstrate the potential of optical gain in this novel organic erbium-doped system.

Thesis outline

Chapter 1, firstly, introduces the electronic configurations and electronic transitions of 4f electrons in lanthanide ions in order to understand the spectroscopic properties of Er^{3+} ions. In addition, a semi-empirical Judd-Ofelt theory, its parameters, and its correlation with the molecular environment and implied optical characteristics of lanthanide ions are explained according to the studies and conclusions found in the literature. Then, the concepts and mechanisms of the organic sensitisation effect are introduced. The brief properties of fluorinated organic complexes are introduced, and their benefits for enhancing the sensitisation effect and quantum yields of Er^{3+} ions are explained. Thirdly, the mechanisms of optical amplifiers are explained, and the challenges of erbium-based gain materials are highlighted

Chapter 2, firstly, introduces the features of the instruments used for the experiments in film deposition, spectroscopy and data analyses. Secondly, the molecular characteristics of materials, which are used in the project, are introduced including molecular structures and crystallographic data. Thirdly, the experimental methodology in the project is explained, such as microscopic absorption measurement on crystals, co-evaporation under vacuum, time-resolved spectroscopy, waveguide fabrication and optical gain measurement.

Chapter 3 presents the experimental data and spectroscopic results on

samples. Firstly, the correlation between molecular environments and electronic transitions in fluorinated erbium complexes is described, and the quantum yields of samples are calculated. Secondly, the sensitisation effect in the novel fully-fluorinated co-doped system is presented and discussed. Then, the mechanisms of the sensitisation effect and the energy transfer processes in the co-doped system are discussed. Thirdly, optical gain properties in the co-doped system, its waveguide properties and gain measurement are presented and investigated.

Chapter 4 summarises the results, breakthroughs and conclusions in the project. Chapter 5 suggests some future work, some new research proposals and new challenges.

Chapter 1. Literature Review and Background

1.1. Electronic configuration of lanthanide elements

1.1.1. Lanthanide element and ions in a ligand field

(1). Lanthanide elements and ions

Lanthanides are a group of elements with atomic numbers ranging from 57 to 71 and have the electron configurations of $[Xe]4f^{n-1}5d^{1}6s^{2}$ or $[Xe]4f^{n}5d^{0}6s^{2}$. The 4f orbitals of lanthanide atoms are occupied from $4f^{1}$ to $4f^{14}$ and there are fully filled electrons on the outer shells $5s^{2}5p^{6}$. In a free lanthanide ion, the 4f electrons are influenced by the nuclear attraction, inter-electronic repulsion and weak spin-orbital coupling.[5,22,23] Therefore, it is challenging to describe rigorously the electronic configuration considering all these interactions. To simplify the treatment of the interactions between electrons, Russell and Saunders have proposed to consider the couplings at the level of overall angular momenta and not for each individual electron[5,22]. In the Russell-Saunders coupling scheme, the orbit-orbit coupling uses L as the total orbital angular momentum that defines the energy state for a system of electrons. These L = 0, 1, 2, 3, 4, 5 and 6 are represented as term-letters S, P, D, F, G, H and I, respectively. The total spin is S and the total angular momentum is J. The spin-orbital coupling can be introduced with the range of $|L - S| \leq J \leq L + S$, where, the 4f orbitals less than half filled gives $J = |L - S|$, otherwise, $J = L + S$. As a

consequence, each term is split further into a number of $^{2S+1}L_J$ levels with $(2J + 1)$ multiplicity. For instance, the ground term of Eu^{3+} is split into $^7F_0$, $^7F_1$, $^7F_2$, $^7F_3$, $^7F_4$, $^7F_5$ and $^7F_6$. In the ground level, the J can be determined with the following rule: if $n < (2l + 1)$, then $J = J_{min}$ but if $n > (2l + 1)$, then $J = J_{max}$, where n is the number of electrons in the orbital l. For instance, the group level of Eu^{3+} ($4f^6$) is $^7F_0$ and the group level of Tb^{3+} ($4f^8$) is $^7F_6$. For higher energy levels, if $n < (2l + 1)$, it is the energy of the levels that increases with increasing values of J, whilst it is inverted if $n > (2l + 1)$. Additionally, if the orbital is half filled, then $L = 0$ and $J = S$, otherwise, J takes half-integer value if S is half integer, for instance, in Er^{3+} ions. It is noteworthy that the Russell-Saunders model is not quite adequate for lanthanide ions since, in heavy atoms, the interaction of electrons is much stronger. However, the Russell-Saunders model is largely used in lanthanide ions for the purpose of simplicity.[5]

In a free Er^{3+} ion, its electron configuration is $[Xe]4f^{11}5d^06s^0$ and the over half filled 4f orbitals give the total angular monument L of 6 presented as I. The $S = 3/2$ for 11 filled 4f orbital and $J = 15/2$ defining the ground state of the Er^{3+} ion as $^4I_{15/2}$. The notation label of an excited state can be defined using the same rule of Russell-Saunders model, for example, the first excited state of the Er^{3+} ion is defined as $^4I_{13/2}$ with one electron is excited and $J = L + S - 1$. The rest of the ground levels of free lanthanide ions in the Russell-Saunders scheme are listed in table 1.1.

$f^{n=0\sim6}$	$f^0(La^{3+})$	$f^1(Ce^{3+})$	$f^2(Pr^{3+})$	$f^3(Nd^{3+})$	$f^4(Pm^{3+})$	$f^5(Sm^{3+})$	$f^6(Eu^{3+})$
Ground Level	$^1S_0$	$^2F_{5/2}$	$^3H_4$	$^4I_{9/2}$	$^5I_4$	$^6H_{5/2}$	$^7F_0$
$f^{n=7\sim14}$	$f^7(Gd^{3+})$	$f^8(Tb^{3+})$	$f^9(Dy^{3+})$	$f^{10}(Ho^{3+})$	$f^{12}(Tm^{3+})$	$f^{13}(Yb^{3+})$	$f^{14}(Lu^{3+})$
Ground Level	$^7F_6$	$^6H_{15/2}$	$^5I_8$	$^4I_{15/2}$	$^3H_6$	$^2F_{7/2}$	$^1S_0$

Table 1.1. Russell-Saunders scheme for ground states of lanthanide free ions.

(2). The lanthanide ions in a ligand-field

In a free lanthanide ion, the 4f orbital is theoretically completely shielded by the fully filled 5s5p and 6s outer shells. When a lanthanide ion is inserted into a ligand environment, the spherical symmetry of its electronic structure is weakly destroyed, and the remaining $(2J + 1)$ degeneracy of its electronic states is partially lifted depending on the symmetry for the ion site or the shape of the coordination polyhedron.[5,22] So, the $4f^n$ electronic wavefunction has just a weak mixture with the surrounding orbitals, resulting in a weak influence of the level splitting (a few hundreds of cm^{-1}) from the ligand environment. Nevertheless, this perturbation of the ligand environment is still responsible for the fine spectral structures[5] and makes the Hamiltonian adequately complex. A simplified concept introduced by H. Bethe in 1929 states that the ligands

considered as (negative) point charges generate a ligand-field (also, crystal-field or Stark splitting).[24] The ligand-field term in the Hamiltonian can be $\sum_{(k,q,j)} B_{kq} C_{kq}$, where the summation involves j on all 4f electrons, B_{kq} represents the ligand-field parameters commonly treated as phenomenological parameters, and C_{kq} represents the components of the tensor operators transforming like a spherical harmonics. The B_{kq} parameters depend on the characteristics of 32 crystallographic symmetry groups, which can be evaluated by k and q with $q \leq k$ in any case. Some non-zero ligand-field parameters for the 4f electronic configurations were reported in some publications.[5]

A partial energy diagram, including the ligand-field splitting based on lanthanide ions doped in a low-symmetry crystal, LaF_3, is given and represented by the Russell-Saunders scheme in figure 1.1.[25] In the diagram, the width or the maximum number of the ligand-field splitting for each electronic level depends on the point group of symmetry.[5,22]

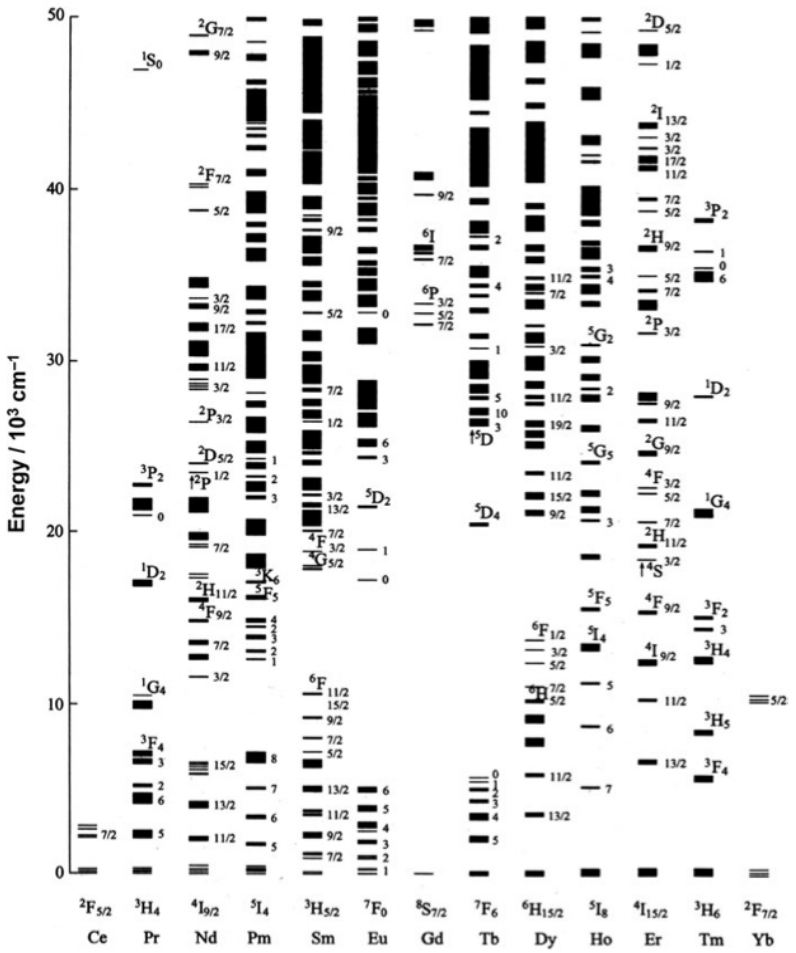

Figure 1.1. Energy level diagram of Ln^{3+} ions doped in a low-symmetry LaF_3 crystal.[25]

(3). Spectral transitions

According to the influence of the ligand-field on the $4f^n$ electronic configuration, the $4f^n$ electronic configurations are weakly varied in different ligand environments around a lanthanide ion, which is reflected from varied absorption of lanthanide ions. The absorption spectra of free lanthanide ions show some narrow fine structures, but the lanthanide ions doped in solutions, glasses or organics have the narrow spectral lines of fine structures broadened.[22] These spectral lines and bands are ascribed to the electronic transitions inside 4f shells. Each fine structural line

corresponds to a ligand-field splitting, and each band corresponds to a transition between two $^{2S+1}L_J$ levels. It is also common that the observation and interpretation of these lines and bands are monochromatic and weak at various ligand environments. The main mechanisms for ascribing the $4f^n$ transitions of lanthanide ions are the magnetic dipole transitions, induced electric dipole (ED) transitions and electric quadrupole transitions.[5,22,23] A magnetic dipole transition is induced by the interaction of a spectroscopic active ion with the magnetic field of light through a magnetic dipole, but the magnetic dipole transition is very weak for most lanthanide ions. An intra-configurational $4f^n$ electric dipole transition is forbidden because states with the same parity cannot be connected by an electric dipole transition, obeying *Laporte's parity selection rule*. However, once a lanthanide ion is doped in a ligand-field, the non-centro symmetric interaction allows the electronic states of the opposite parity to be mixed into the $4f^n$ electronic wavefunctions so that the selection rules are relaxed and the transitions are partially allowed.[22] A quadrupole transition is partially allowed but is much weaker than a magnetic dipole transition and not usually observed.[5]

(4). Dipole transitions

Electric dipole (ED) transition is the interaction of an electron in an atom with the electromagnetic field. In a single electron and single atom

system, the electric dipole transition depends on the dimension of harmonic oscillator momenta between the negative charge and positive charge. The strength of electric dipole transition is evaluated by oscillator strength or line strength, which is a dimensionless quantity, since it is the ratio of an actual intensity to an intensity radiated by one electron oscillating harmonically in three dimensions. So, the line strength reflects the probability of an electric dipole transition. Moreover, when a lanthanide ion doped in a ligand-field, the ligand-field induces the electric dipole transition by mixing a perturbation into the $4f^n$ electronic configurations, so that the transitions are induced to be induced electric dipole transitions.[26-28] There are three types of the induced electric dipole transitions for lanthanide ions: the sharp intra-configurational $4f^n$ transitions, broader $4f^{n-1}5d$ transitions and charge-transfer transitions, where the charge-transfer transition can be a metal-to-ligand charge transfer (MLCT) or a ligand-to-metal charge transfer (LMCT). Although the induced electric dipole transition is partially allowed, some transitions of them are sensitive to a minor change in the ligand-field. They are hypersensitive transitions and apparently follow the selection rules of the ED transitions,[22] in addition to the selection rule of parity, other rules also apply, such as ΔS (the spin electron rule), ΔL (the orbital selection rule) and ΔJ (the total momentum selection rule).[22,23]

1.1.2. Line strengths and Judd-Ofelt theory

(1). Induced electric dipole transitions and Judd-Ofelt theory

Firstly, a single spectral line in an oriented system is considered. If a state of the wavefunction is defined as $\left\langle l^{n}\psi JM\right|$ and another state of the wavefunction is defined as $\left\langle l^{n}\psi' J'M'\right|$, where ψ is the additional quantum number defining a level uniquely (in the Russell-Saunders coupling scheme, it represents *L* or *S*), and *M* is the quantum number of the projection J_z of the total quantum momenta *J*. l^n denotes that the transition occurs between the levels of the same configuration. The electric dipole operator is $\hat{m}$ and the transition operator is $\hat{D} = -\hat{m}/e$. The induced dipole matrix elements are: $\hat{m} = -e\hat{D} = -e\sum_j \hat{r} = -e\sum_j r_j \hat{C}$, where $\hat{r}$ is the position vector of the electron *j* and $\hat{C}$ is the irreducible tensor operator containing the angular coordinates of the electron *j*. The wavefunction of the initial state can be ascribed to a linear combination of all components of the ground levels of the l^n configuration: $\left\langle \chi \right| \equiv \sum_M \left\langle l^{n}\psi JM\right| a_M$, in which χ is a ligand-field level, a_M is a statistic coefficient arising from the ligand-field mixture. Similarly, the final state can be $\left|\chi'\right\rangle \equiv \sum_{M'} \left| l^{n}\psi' J'M'\right\rangle a'_{M'}$. According to Laporte's selection rule, these descriptions cannot work on the intra-configurational $4f^n$ transition because there is no change of the dipole moment of the ion at the same l^n configuration.

Therefore, Judd[29] and Ofelt[28] independently worked out a theoretical

model for the calculation of induced electric dipole transitions. The basic idea is that an admixture of opposite parity can relax the forbidden $4f^n$ electric dipole transitions. The odd part of the ligand-field potential is considered as the perturbation for mixing states of different parity. And, the strength formula of induced electric dipole transition is cast in a form allowing a parameterisation to multiply the reduced matrix elements.

The perturbation, built from the configurations of opposite parity to the l^n electronic states and mixed into $\langle\chi|$ and $|\chi'\rangle$ states, derives the $4f^{n-1}5d$ or so-called f-d mixing due to a non-symmetrical ligand-field. And, the derived perturbing state has a higher excited energy level than the l^n configuration.[22,23] This derives induced electric dipole transitions. In an induced electric dipole transition, the ligand-field can be considered as a first-order perturbation which mixes the states of the excited configuration $|l^n\psi''J''M''\rangle$ with a parity opposite to the l^n into the $\langle\chi|$ and $|\chi'\rangle$ states. Thus, the $\langle\chi|$ and $|\chi'\rangle$ states become the $\langle\Psi|$ and $|\Psi'\rangle$ states, respectively:

$$\langle\psi| = \sum\nolimits_M \langle l^n\psi JM|\, a_M + \sum \langle l^{n-1}\psi''J''M''|\, b$$
$$|\psi'\rangle = \sum\nolimits_{M'} a'_{M'} |\, l^n\psi'J'M'\rangle + \sum b' |\, l^{n-1}\psi''J''M''\rangle$$

where

$$b = \frac{\sum_M a_M \left\langle l^{n}\psi JM \middle| \hat{V}_{odd} \middle| l^{n-1}\psi'' J'' M'' \right\rangle}{E(\psi J) - E(\psi'' J'')}$$

$$b' = \frac{\sum_{M'} a'_{M'} \left\langle l^{n}\psi'' J'' M'' \middle| \hat{V}_{odd} \middle| l^{n-1}\psi' J' M' \right\rangle}{E(\psi' J') - E(\psi'' J'')}$$

The operator $\left\langle \hat{V}_{odd} \right|$ is the odd part of the ligand-field Hamiltonian (k = odd).[22] Then, the matrix elements in the transition operator are $\left\langle \Psi \middle| \hat{m} \middle| \Psi' \right\rangle$. There is a challenge to rigorously solve the matrix elements so that several approximations need be considered in functionalisation. General understanding of approximation can help distinguish which kinds of lanthanide ions are suitable for the Judd-Ofelt theory. There are three approximations:[22]

1st approximation: No ligand-field splitting of the perturbing configuration $\left| l^{n-1}\psi'' J'' M'' \right\rangle$ is considered so J'' and M'' are degenerate. The reason is that the splitting of ${}^{S+1}L_{J''}$ within one scheme of the perturbation level can be negligible compared to the energy difference between the energy of the perturbation level and ground level. Also, the spin-orbital coupling is neglected in the perturbation level.

2nd approximation: Each perturbing configuration is considered to be totally degenerate. So, the energy of each $E(\psi' J')$ level is set equally to be the mean energy of the corresponding configuration so that it assumes the band of each transition to be symmetric. Also, it is invariant with respect to the ψ'' and J'', which means a lanthanide ion with a broad energy level of

the $4f^{n-1}5d$ configuration might not be explained perfectly by the Judd-Ofelt theory.

3rd approximation: The perturbing configurations lie far above the states for the 4f transitions. It is significant that, if the highest levels of the $4f^n$ configuration are close to the average energy of the perturbing configuration, the mixing of the perturbing configuration and $4f^n$ configuration will tend to be cancelled.

Therefore, the final expression of the line strength of the induced electric dipole transition between the Ψ and Ψ′ states is given by:

$$S_{ED} = \sum_{\lambda=2,4,6} \Omega_\lambda \left| \left\langle \Psi \left| U^{(\lambda)} \right| \Psi' \right\rangle \right|^2 \qquad (1\text{-}1)$$

where the term λ (λ = even and $0 < \lambda \leq 6$) is introduced during the calculation of the matrix elements $\left\langle \Psi \left| U^{(\lambda)} \right| \Psi' \right\rangle$. $U^{(\lambda)}$ is the irreducible tensor form of the electric dipole operator and $\Omega_{\lambda=2,4,6}$ are the Judd-Ofelt parameters. The solutions of the electric dipole matrix elements are crucial to estimate the Judd-Ofelt parameters through the line strengths, but it is complicated. Several studies have evaluated the reduced matrix elements for lanthanide ions in both aqueous solutions and LaF_3 crystals.[30] To study Er^{3+} ions, the values of $[U^{(\lambda)}]^2 = \left| \left\langle \Psi \left| U^{(\lambda)} \right| \Psi' \right\rangle \right|^2$ in Er^{3+} ions doped LaF_3 crystals are listed in table 1.2, which refer to the calculation of Carnall et al.[30]

$S'L'J' \leftarrow {}^4I_{15/2}$	Calculated wavelength (nm)	$[U^{(2)}]^2$	$[U^{(4)}]^2$	$[U^{(6)}]^2$
$^4I_{13/2}$	1527.42	0.0195	0.1173	1.4299
$^4I_{11/2}$	982.61	0.0291	0.0004	0.3969
$^4I_{9/2}$	811.36	0	0.1856	0.0122
$^4F_{9/2}$	660.33	0	0.5275	0.4612
$^4S_{3/2}$	546.30	0	0	0.2230
$^2H_{11/2}$	520.54	0.7326	0.4222	0.0927
$^4F_{7/2}$	492.61	0	0.1467	0.6280
$^4F_{5/2}$	455.58	0	0	0.2237
$^4F_{3/2}$	448.27	0	0	0.1256
$^2G_{9/2}$	408.53	0	0.0157	0.2278
$^4G_{11/2}$	378.30	0.8970	0.5123	0.1172

Table 1.2. The reduced matrix elements $[U^{(2)}]^2$, $[U^{(4)}]^2$, $[U^{(6)}]^2$ for the transition in the range of mean wavelengths of 378 nm ~ 1530 nm. The labelled levels are the excited levels. Each row of reduced matrix elements corresponds to the transition between the labelled levels and the ground level of $^4I_{15/2}$. The transitions of $^4I_{15/2} \rightarrow {}^2H_{11/2}$ and $^4I_{15/2} \rightarrow {}^4G_{11/2}$ have dominated values of $[U^{(2)}]^2$ compared to other transitions and the transition of $^4I_{15/2} \rightarrow {}^4I_{13/2}$ has a dominated value of $[U^{(6)}]^2$ compared to other transitions.

(2). Selection rules for induced dipole transitions

In accordance with the calculation of matrix elements and the selection rules of electric dipole transitions, the selection rules of induced electric dipole transitions are:[22]

$$|\Delta L| \leq 6;\ |\Delta J| \leq 6,\ |\Delta J| = 2, 4, 6 \text{ if } J = 0 \text{ or } J' = 0;\ |\Delta S| = 0;$$

The selection rules and the approximations mentioned above give the rank of λ, which has to be 2, 4 or 6[22]. It is noteworthy that the selection rules of

ΔL and ΔS are only applicable in the Russell-Saunders coupling scheme. J remains a good quantum number so that the selection rule of ΔJ is harder to break down since the J-mixing is weak.[22,26]

(3). The Judd-Ofelt parameterisation

Judd-Ofelt parameters are obtained from fitting experimentally measured line strengths to the corresponding theoretically calculated line strengths. In this study, all measured line strengths are extracted from the absorption of samples. The measured line strength for an absorption band is:

$$S_{\mathrm{me}} = \frac{3ch(2J+1)n}{8\pi^3 \bar{\lambda} e^2 N}\left[\frac{9}{(n^2+2)^2}\right]\int \alpha(\lambda)\, d\lambda \qquad (1\text{-}2)$$

where n is the refractive index of the sample or the host medium, c is the light speed in vacuum and h is plank constant. In solutions, this refractive index can be the refractive index of the solvent used due to a much lower concentration of dissolved complex molecules than of solvent molecules. N is the concentration of the lanthanide ions.

$\alpha(\lambda)$ is the absorption coefficient of a single line spectrum. The integral of the absorption coefficient considers the spectral band of the absorption for each transition, whiles the above equation means that the absorption band assumes to be considered symmetrically.[27] The $\bar{\lambda}$ is the mean wavelength of an individual absorption band.

Standard least-squares method for fitting: Ω_λs are usually determined

by the minimum deviation between the calculated line strength and the measured line strength via a standard least-squares method. The standard least-squares method minimises the absolute differences between the experimental and theoretical values. The disadvantages are that a small discrepancy in a large experimental value has the same influence as a large error in a small experimental value.[22] Therefore, the parameters depend largely on the relative magnitudes of the measured line strengths. We can define the measured and calculated line strength of each transition as S^i_{me} and $S^i_{ED} = \Omega_2 [U_i^{(2)}]^2 + \Omega_2 [U_i^{(4)}]^4 + \Omega_6 [U_i^{(6)}]^6$, respectively, where i is the serial number of each transition. Here, $\Delta^{|ED\text{-me}|}$ is defined as the summation of least-squares differences between the calculated and measured line strengths: $\Delta^{|ED-\mathrm{me}|} = \sum^{n'}_{i=1}(S^i_{\mathrm{me}} - S^i_{ED})^2$. The partial differentiation of the summation is derived by Ω_2, Ω_4 and Ω_6 from three equations: $d\Delta^{|ED\text{-me}|}/d\Omega_{\lambda\ (\lambda=2,4,6)} = 0$. The simplification of these equations can be written in matrix form:

$$\begin{bmatrix} \sum_{i=1}^{11}[U_i^{(2)}]^4 & \sum_{i=1}^{11}[U_i^{(2)}]^2[U_i^{(4)}]^2 & \sum_{i=1}^{11}[U_i^{(6)}]^2[U_i^{(2)}]^2 \\ \sum_{i=1}^{11}[U_i^{(2)}]^2[U_i^{(4)}]^2 & \sum_{i=1}^{11}[U_i^{(4)}]^4 & \sum_{i=1}^{11}[U_i^{(4)}]^2[U_i^{(6)}]^2 \\ \sum_{i=1}^{11}[U_i^{(2)}]^2[U_i^{(6)}]^2 & \sum_{i=1}^{11}[U_i^{(4)}]^2[U_i^{(6)}]^2 & \sum_{i=1}^{11}[U_i^{(6)}]^4 \end{bmatrix} \begin{bmatrix} \Omega_2 \\ \Omega_4 \\ \Omega_6 \end{bmatrix} = \begin{bmatrix} \sum_{i=1}^{11}[U_i^{(2)}]^2 S^i_{\mathrm{me}} \\ \sum_{i=1}^{11}[U_i^{(4)}]^2 S^i_{\mathrm{me}} \\ \sum_{i=1}^{11}[U_i^{(6)}]^2 S^i_{\mathrm{me}} \end{bmatrix}$$

(1-3)

If we define the coefficient matrix as **M**, the matrix on the right of the equation as **R**, and the element matrix of Judd-Ofelt parameter as **Ω**, the

matrix equation is consequently written as $\mathbf{\Omega} = \mathbf{M}\mathbf{M}^{-1}\mathbf{R}$. The root-mean-square deviation $\Delta_{\mathrm{rms}} = \sqrt{\sum_{i=\mathrm{n}'}(S_{ED}^{i} - S_{\mathrm{me}}^{i})^2 / \mathrm{n}'(S_{ED}^{\max} - S_{\mathrm{me}}^{\min})^2}$, in which n′ is the number of the accounted measured line strengths, indicates the fitting errors.

(4). Radiative transition and emission quantum yield:

A radiative transition is the transition that will emit electromagnetic radiation. Electrons absorbing the energy from incident photons are excited into the higher energy states and will then go back to the ground states. This transition process, which is also called emission or luminescence, will transfer the energy from the matter into the energy of emitted photons or another radiation field. There are two main emission processes: spontaneous emission and stimulated emission. Stimulated emission can be considered as a continuous spontaneous transition process resulting from population inversion. The quantitative identification for a spontaneous emission is the radiative rate, which defines the probability that electrons transit between two states in order to emit photons. In lanthanide ions, the radiative rate can be obtained from the calculated line strength or measured line strength. The radiative rate between an excited state and the ground state is defined as $\mathrm{A}_{J\leftarrow J'}$

$$\mathrm{A}_{J\leftarrow J'} = \frac{64\pi^4 e^3}{3h(2J+1)\bar{\lambda}^3}\left[\frac{n(n^2+2)^2}{9}\right]S_{ED}(J \rightarrow J') \qquad (1\text{-}4)$$

In a radiative transition process, the radiative lifetime is the time for the population of emitters decay to 1/e (36.5%) of the initial population. A radiative lifetime is the inverse to the radiative rate, and should be the lifetime counting for a process that contains all transitions above the ground states. Hence, the radiative lifetime would be:

$$\tau_r = 1 \Big/ \sum_{J'} A_{J \leftarrow J'} \qquad (1\text{-}5)$$

So, for the $^4I_{13/2} \longrightarrow {}^4I_{15/2}$ transition, the radiative lifetime for 1.5 μm emission is defined as $\tau_{r1.5\mu m} = 1/ A (^4I_{13/2} \rightarrow {}^4I_{15/2})$.

However, the real emission consists of both the radiative transition and the non-radiative transition, since the population could relax from the excited states through non-radiative transitions and, so to convert the energy to heat. The vibration of a ligand-field and the energy transfer between states could cause non-radiative transitions in molecules. Therefore, the total emission lifetime, which is observed through experiments, is the combination of the radiative lifetime τ_r and the non-radiative lifetime τ_{nr},

$$1/\tau_{em} = 1/\tau_r + 1/\tau_{nr} \qquad (1\text{-}6)$$

The emission lifetime can be obtained by fitting the time-resolved luminescence spectrum in experiments. Using the emission lifetime obtained from experiments and the calculated line strength obtained from Judd-Ofelt parameters, the internal emission quantum yield (0% ~ 100%) of each transition of a lanthanide ion can be obtained as:

$$\eta = (\tau_{em} / \tau_{r})\% \qquad (1\text{-}7)$$

1.1.3. The physics of Judd-Ofelt parameters

(1). Judd-Ofelt parameterisation for organic erbium complexes

The Judd-Ofelt theory provides a frame to reflect the parametric information of the electronic configuration of lanthanide ions in a ligand-field and the electron distribution on the erbium-ligand bond. Several studies have been done on inorganic lanthanide complexes, such as lanthanide ions doped fluorinated glasses and nanocrystals.[31-33] Some research has shown that Judd-Ofelt parameterisation for some organic erbium complexes coordinated with hydrogenated ligands can be quantified in various solutions, and indicates that the solvent molecules could be involved in the coordination with lanthanide ions[34-37]. Nevertheless, only a few analyses of organic lanthanide complexes in solid state have been undertaken[13,37], especially for organic fluorinated complexes, since the chemical synthesis and crystallisation are difficult due to the chemical and thermal instability caused by the strong electronegativity of fluorine.

Moreover, the accurate characterisation for the IR transition of Er^{3+} ions in organic systems have barely been investigated, since most organic complexes are researched in hydrogen-contained solutions, in which the IR transitions of Er^{3+} ions are strongly quenched or cannot be observed.[35,37-39]

(2). Hypersensitive transition: Ω_2

As mentioned before, some transitions are very sensitive to the environment of ligand-fields with a variation of the factor of ~ 200 in varied doped matrices.[5,22,23] These transitions, called hypersensitive transitions, obey the same selection rules as other transitions. Much attention has given to the explanation of the phenomenon and the mechanism of the hypersensitive transitions in the literature.[22,23,26,34,36,37,40-42] In Er^{3+} ions, two hypersensitive transitions are usually reported in literature: the $^2H_{11/2} \leftarrow ^4I_{15/2}$ transition and the $^2G_{11/2} \leftarrow ^4I_{15/2}$ transition at the approximate mean wavelength 520 nm and 379 nm, respectively.

Chemical characteristics effect:

The hypersensitive transitions of Er^{3+} ions in solutions have been studied in detail. Some papers suggested that: 1) the number of organic ligands coordinated contributes to varying intensities of the hypersensitive transitions in non-aqueous organic solvents; 2) more solvent molecules coordinated to the Er^{3+} ions, for instance, in strong aqueous chloride

solvents, can boost the intensity of Er^{3+} absorption; and 3) stronger basicity of the coordinated ligands increase the absorption intensities of the Er^{3+} ions due to the stronger electronegativity of the ligands.[36,43,44] These conclusions have been confirmed and supported by a number of publications, which performed many studies on erbium doped glasses, erbium doped nano-particles and erbium doped hydrogenated complexes over years[22,43,45,46]. However, in most publications, only a few studies were performed on fluorinated organic erbium complexes in solutions or solid state.[12,13] No study discusses the effects of fluorination on the hypersensitive transitions of Er^{3+} ions by comparing the Judd-Ofelt parameterisation, spectroscopy and molecular structures between fluorinated and corresponding non-fluorinated organic complexes, despite some types of fluorinated erbium organic complexes have been reported to have efficient spectroscopic characteristics.[11,13,20]

Site symmetry:

The suggestion that the intensity of hypersensitive transition is strongly correlated with the site symmetry for the central lanthanide ion is based on the fact that the intensity of hypersensitive transition theoretically equals zero when the lanthanide ion sits in the centre of symmetry. Many studies of Nd^{3+}, Eu^{3+}, Ho^{3+} and Er^{3+} ions doped in crystalline hosts, like Y_2O_3 or fluorinated doped glasses, show that the higher site-symmetry causes a lower intensity of hypersensitive transition.[47-49] Further studies on the series

of hydrogenated erbium organic complexes in solutions determined that an increasing number of coordinated ligands reduces the symmetry so that the intensities of hypersensitive transitions decrease.[22,50,51]

Ω_2 relates to hypersensitive transitions:

Judd originally suggested that hypersensitive transitions are related to the reduced matrix element of $U^{(2)}$, mainly described by Ω_2 parameters, if the $U^{(4)}$ and $U^{(6)}$ matrix elements for the hypersensitive transitions are small.[29,52] However, the essential mechanism for the relationship between Ω_2 and the hypersensitive transition is not well explained by the original Judd-Ofelt theory, because not all the metal-ligand interactions can be taken into account for the explanation of Ω_2.[22,29] Another reason why the Judd-Ofelt theory is not exactly suitable for the hypersensitive explanation is that the transitions of a lanthanide ion are induced directly by the electric dipole moment of the ligands, with the assumption that each ligand is a static charge point and not influenced by the external potentials. This is also the reason that the Judd-Ofelt theory is also known as the static-coupling model.[22] The static-coupling model requires that the lanthanide ions are centred at an electric equilibrium position in any environment, so that the perturbation is from the negative charge field of ligands surrounding the electronic configuration of lanthanide ions. However, Judd observed that the ligand-field parameter B_{kq}, which implies there is no equilibrium for the centred lanthanide ions, could change the Ω_2

parameter, particularly since it ascribes the contribution of ligand-fields to the central lanthanide ions. Judd later modified the theory for including ligand-field parameters and pointed out that hypersensitive transitions could only be observed in point groups of $C_{(s, 1, 2, 3, 4, 6, 2v, 3v, 4v \text{ and } 6v)}$, since the electrons of the lanthanide ions could produce a non-vanishing electric field at the centre nucleus in these point groups.[41] Nevertheless, there are several exceptions[22,53], such as the holmium tris(methylcyclopentadienyl) complex having the fine structure of the ligand-field but without a compatible B_{kq} from calculation.

Furthermore, a bond model of hypersensitive transitions was proposed because charge-transfer transitions occur in lanthanide complexes, and are very sensitive to the types of ligands and lanthanide ions. The energy of the ligand-to-metal charge transfer transition is functionalised by the metal orbital energy, inter-electronic correlation and ligand energy.[44,54] Conveniently, the charge-transfer energy might be expressed as the difference between the optical electronegativity of a ligand and metal ion.[27,55] This matches the fact that the energies of charge-transfer transitions are even increased by increasing the number of coordinated ligands, and by the nature of coordinated ligands.[27,56] Then, the Judd-Ofelt theory was modified to include charge-transfer states as perturbing states into the $4f^n$ configuration, in addition to the perturbing configurations of $4f^{n-1}5d^1$.[56] Besides, another noticeable point is found that the nephelauxetic

effect has a direct contribution to hypersensitive transtions.[44] The nephelauxetic effect implies that the inter-electronic repulsion between electrons on the metal-ligand bond in a formed complex is less than the corresponding inter-electronic repulsion on the free metal ions. This effect increases with increasing the degree of the coordination bond between the lanthanide ions and ligands due to the red-shift of the f-f transitions.[27] All the above evidences and observations show that the electron interaction or redistribution on the coordinated bond of the lanthanide ion and ligand contributes to the intensities of hypersensitive transitions. Therefore, a dynamic-coupling model or ligand-polarisation model was additionally brought to describe hypersensitive transitions. In this model, the dipoles are induced by the charge distribution caused by the f-f transition, so that the ligand wavefunctions are perturbed by the lanthanide ion. The dynamic-coupling model includes more point groups that can cause hypersensitive transitions with respect to the groups that Judd pointed out.[53,57-61] Nevertheless, some exceptions of lanthanide ions did not match the pure dynamic-coupling model complexes. For example, the Ω_2 parameters have been found to have no variation in the series complexes of Ln(Ho, Er, Eu)$(DBM)_3H_2O$, which are opposite to the predicted by the dynamic-coupling model.[62]

Therefore, a combined statistic-coupling/dynamic-coupling theory is used and the intensities are directly calculated without introducing intensity

parameters.

(3). Ω_4 and Ω_6

The variations of Ω_4 and Ω_6 parameters have been considered, since the 1980s, as having an association with the composition and properties of host matrices.[27] A comparative study of the intensity parameters for Er^{3+} doped glasses concluded that the Ω_4 and Ω_6 parameters are related to the rigidity of the medium where the lanthanide ions are doped,[63] and Ω_6 of Er^{3+} ions is related more to its infrared $^4I_{15/2} \rightarrow {}^4I_{13/2}$ transition.[64] The parameters increase over a series of increasing mean displacements from equilibrium distances to the nearest-neighbour ion, or the parameters increase with the increasing of the vibrational amplitude of the lanthanide ion-to-ligands distance.

Generally, the complex of organic ligands possesses a higher rigidity with respect to other host matrices such as glasses, crystalline-mixed oxides and viscous solutions. Also, further studies have shown that the Ω_6 parameter is sensitive to the radial integral of the 4f and 5d orbitals, $\left\langle 4f \left| \hat{r}^k \right| 5d \right\rangle$, and has more sensitivity than Ω_2.[65] The radial integral of the 4f and 5d orbitals is supposed to increase with decreasing the density of 6s electrons since its repulsion on 5d electrons are decreased.[27] For example, a study of Er^{3+} ion doped alkai borate glasses showed that the variations of the Ω_4 and Ω_6 parameters were related to the local basicity of the

lanthanide sites.[66] And, another implication is that the Ω_4 and Ω_6 parameters of Eu^{3+} doped silicate glasses were reported not only related to the coordinated bond of Eu-O but also the structural change.[67]

In Er^{3+} ions, the Ω_6 parameter is significant to the $^4I_{15/2} \rightarrow {}^4I_{13/2}$ transitions.[68] The calculate line strength of the $^4I_{15/2} \rightarrow {}^4I_{13/2}$ transition is $S_{ED}{}^{1.5\mu m} = \Omega_2 [U^{(2)}{}_{1.5\mu m}]^2 + \Omega_4 [U^{(4)}{}_{1.5\mu m}]^2 + \Omega_6 [U^{(6)}{}_{1.5\mu m}]^2$, where 1.5 μm is the wavelength for the $^4I_{15/2} \rightarrow {}^4I_{13/2}$ transition. In this expression, the Ωs and reduced matrix elements are independent so that the deviation of the line strength on each Ω parameter can be expressed by $dS_{ED}{}^{1.5\mu m} / d\Omega_\lambda = [U^{(\lambda)}{}_{1.5\mu m}]^2$. In table 1.1, the reduced matrix element $[U^{(6)}]^2$ of the $^4I_{15/2} \rightarrow {}^4I_{13/2}$ transition is bigger than all elements of the remaining transitions, and is dramatically bigger than $[U^{(2)}]^2$ in the factor of ~ 70 and $[U^{(4)}]^2$ in the factor of ~ 12. These values mean that the line strength of the $^4I_{15/2} \rightarrow {}^4I_{13/2}$ transition has the biggest variation with changing Ω_6, or is mainly determined by the value of Ω_6.

Unfortunately, for organic erbium complexes, it is more difficult measuring the absorption for the $^4I_{15/2} \rightarrow {}^4I_{13/2}$ transition because the IR absorption cannot be seen in solution due to the presence of C-H, O-H or N-H absorption. Thus, the line strength and the radiative lifetime at 1.5 μm emission are often estimated through fitted Judd-Ofelt parameters resulting from the absorption over just the UV-visible bands.[41-44]

1.2. Organic sensitisation enhances the luminescence of erbium

1.2.1. The organic sensitisation and energy transfer

(1). Sensitising erbium ions using organic chromophores

When an Er^{3+} ion emits photons, emission displays the IR 1.5 μm line for the $^4I_{13/2} \rightarrow {}^4I_{15/2}$ transition rather than spectral lines, such as the visible 520 nm line for the $^2H_{11/2} \rightarrow {}^4I_{15/2}$ transition, or the IR 980 nm line for the $^4I_{11/2} \rightarrow {}^4I_{15/2}$ transition. The radiative transitions of Er^{3+} ions generally have long lifetimes, owing to that their narrow absorption or emission cross-section in most inorganic and organic hosts are as weak at 10^{-22} to 10^{-20} cm^2 for a wavelength, because the internal 4f transitions are naturally forbidden by the selection rules of both parity and spin, despite the selection rules are partially relaxed by the ligand-fields.[6,23] So, a very powerful exciting source, like a laser, is required to produce a bright emission, even though many erbium doped inorganic systems have very high quantum yields.[1,6,8,69,70]

In contrast, organic chromophores generally have a large absorption cross-section (up to 10^{-15} to 10^{-17} cm^2 for a wavelength) and broad absorption (hundreds of nano-meter bandwidth), therefore, an idea to downgrade the exciting power is to implant coordinated Er^{3+} ions into organic chemical groups which can provide the sensitisation effect or "antenna effect".[5,71-78] The sensitisation process obeys three distinct

processes. Firstly, the light or electric fields are strongly absorbed by the attached chromophores or coordinated organic ligands. Secondly, the absorbed energy is transferred into some higher-excited states of Er^{3+} ions. Finally, the energy at the higher-excited states of Er^{3+} ions decays to some lower-excited states of Er^{3+} ions to produce the intense luminescence.

The energy transfer process covers multiple energy-migration paths. In organic chromophores, the main energy-migration path implies the Laporte- and spin-allowed ligand-centred absorptions, from which the excited singlet states (states with the total spin 0) are converted partially to the long-lived triplet states (states with the total spin 1) by an intersystem crossing. Then, the excited $4f^n$ states of lanthanide ions accept the energy transferred from the triplet states in organic chromophores. This was suggested by initial research showing that the energy levels of triplet states are broader and match better the energy levels of excited states of several lanthanide ions.[17] The energy transfer process consists of many mechanisms, such as Föster energy transfer, Dexter energy transfer, charge-transfer (the inter-ligand charge transfer: ILCT, the ligand-metal charge transfer: LMCT, and the metal-ligand charge transfer: MLCT.[23] Consequently, if the entire energy-migration mechanisms are necessarily considered, 20 - 30 rate constants are required to describe a workable model, which renders this method complicated for a precise simulation of the mechanisms.[5,15]

However, in most organic sensitisation process, because the charge-transfer energy is usually very high,[5] the focus is on the common model that the energy is transferred from the ligand-centred excited triplet states, which are derived from the excited singlet states, to the excited states of lanthanide ions via the Föster energy transfer mechanism.

(2). Fluorescence process

The electronic states of an organometallic chromophore can be grounded into a singlet state and a triplet state coupling with the widely vibrational energy states of the molecules. A singlet state is one, in which all of the electrons in one molecule have their paired spins, and a triplet state is one, in which one set of electron spins have become unpaired. A triplet state also lies lower in energy than the corresponding singlet state. When organics absorb the incident photons or injected electrons, the singlet excitons are formed by the transition from the ground S^0 states to the first excited S^1 states, obeying the selection rules of no spin change for the dipole-dipole transition. This process is fast because it is allowed and the rate depends on the photon density of the incidence. Afterwards, the non-radiative relaxation will redistribute the excited electrons over all vibrational levels that couples with the corresponding vibrational splitting. The vibrational relaxation is quite rapid and efficient, even at room temperature, so the process is as short as 10^{-13} to 10^{-11} sec. This means that

a vibrational relaxation is necessary before an excited molecule can emit a photon in 10^{-9} to 10^{-7} sec, and then the photon emission will occur from the lowest vibrational level of an excited state.[79] Once a molecule sits at the lowest vibrational level of an excited S^1 state, it can return to the ground S^0 state by emitting a photon. This process is called fluorescence, and its lifetime is in the order of nanoseconds to microseconds.[79] The redistribution of electrons over the vibrational splitting can induce a Stokes Shift. This consists of the shifts of fluorescence spectrum to longer wavelengths with respect to the absorption spectrum.[79]

An excited molecule could encounter non-radiative processes, in which an excited singlet state returns to the ground state without emitting a photon, but converts the energy into heat. However, measuring this process is difficult since the non-radiative processes are usually of short time scales and strongly influenced by the environment.

(3). Intersystem crossing and phosphorescence

Contrary to the mechanism necessary to achieve the population of excited singlet states, a direct absorption from the ground S^0 state cannot populate the triplet states, since the dipole transition obeys the rule of no spin-change. However, there exists one efficient process that allows for populating triplet states from the lowest excited singlet states. This is a spin-dependent internal conversion process called intersystem crossing

(ISC), which requires the interaction of the vibrational coupling between the excited singlet state and triplet states.[80-82] Nevertheless, the intersystem crossing is still less probable than the process of a singlet-singlet transition. The intersystem crossing requires approximately 10^{-8} to 10^{-7} sec for a spin-forbidden vibrational process, which is the same order of magnitude with the lifetime of an excited singlet state. Therefore, the process of the intersystem crossing can be completed in the timescale of fluorescence, but is incapable of occurring within the timescale of the vibrational relaxation process between the vibrational splitting in an excited singlet state. Moreover, the intersystem crossing process is a non-radiative transition and makes the triplet state lower in energy than the corresponding excited singlet state. So, the vibrational coupling between the triplet state and the ground S^0 state is enhanced for an internal conversion. The internal conversion can relax the spin forbidden transition, but the lifetime of a triplet state is still as long as ~ 10^{-4} to 10 sec, which is much longer than the typical lifetime of a fluorescence. Therefore, the non-radiative loss for the triplet states through the collision or energy transfer is generally magnified. If a molecule is placed in an environment where the loss of non-radiative energy is minimised, a radiative transition between the lowest triplet state and the ground state will occur, and this process is the phosphorescence. The lifetime of the phosphorescence is also as long as the lifetime of the triplet state.

The long lifetime of a triplet state could also lead to a long lifetime of the interaction between several triplet excitons. This process produces much quenching of the triplet excitons, of which some mechanisms have been investigated, such as the triplet-triplet annihilation where two molecules both in a triplet state interact to produce one molecule in an exited singlet state and another in its ground singlet state[83-86] If it is assumed that the excited singlet state of the molecule is rapidly and efficiently transferred to the triplet state via the intersystem crossing, and only the guest molecules contribute to the triplet-triplet annihilation, then the energy of a donor molecule can be exchanged via energy transfer (dipole-dipole or electron exchange) to an excited acceptor molecule, due to overlapping the energy states of the donor and acceptor molecules. This interaction would lead to a set of new excited singlet states, which could emit photons faster than the phosphorescence. This process is called delayed-fluorescence and is mainly dominated by the concentration of the triplets in the excited molecules.

(4). Heavy metallic ion and fluorination enhanced intersystem crossing

The heavy-atom has been observed to make contribution to the intersystem crossing route. For example, the sulphur atoms enhance the intersystem crossing of the thiophene-based conjugated materials.[80,81,86,87] Generally, the interaction between the spin and orbital momenta of an electron induces a mixing between the singlet and triplet excitons. The

spin-orbital Hamiltonian writes: $H_{SO} = \alpha_{fs}^2 \sum_{\mu}^{N} \sum_{\mu}^{n} \frac{Z_\mu}{r_{i\mu}^3} \vec{L}_i \vec{S}_i$, where Z_μ is the charge or effective charge for the nucleus μ, and L and S are the orbital and spin momenta, respectively. This Hamiltonian represents the coupling between the spin and orbital momenta of an electron i, under the interaction with the nuclear field of the nucleus μ. So, $r_{i\mu}$ represents the distance between an electron i and a nucleus μ. The intersystem crossing rate can be obtained by functionalising this spin-orbital Hamiltonian on the final triplet state and on the initial singlet state. To compute the intersystem crossing rate, k^{IF}_{ISC}, between an initial singlet state I and a final triplet state F, we can use the golden-rule expression for radiationless transitions: $k^{IF}_{ISC} = \frac{2\pi}{\hbar} \left\langle {}^1\Psi_I^0 \middle| H_{SO} \middle| {}^3\Psi_F^0 \right\rangle^2$ [FCWD] and the Frank-Condon weighted density of states,[80] $\mathrm{FCWD} = \frac{1}{\sqrt{4\pi E_M RT}} \exp\left[-\frac{(\Delta E + E_M)^2}{4\lambda RT} \right]$, ie., the density of vibrational states in the triplet times the Franck-Condon vibrational overlap. E_M is the Marcus reorganisation energy, ΔE is the energy difference between the initial and final states and T is temperature.[80]

The Hamiltonian and intersystem crossing rate expressions imply: i) Spin-orbital interaction between the singlet and the close triplet state is obvious due to lower energy difference ΔE, ii) Spin-orbit interaction is highly sensitive to the atomic number Z so that the substitution of the conjugated chains with the heavy-atom-containing groups would enlarge

the intersystem crossing rate.

As for fluorinated organics, the fluorination of the chemical group can increase the spin-orbital coupling compared to the corresponding hydrogenated chemical group, since the fluorination increases the effect of the nuclear charge in organics. This evidence has been investigated in many π-conjugated organic molecules in experimental and theoretical calculations.[87,88] For instance, the optical absorption and emission spectra of several fluorinated organics like oligomers have been reported to have the spectral red-shift compared to the un-substituted species, and the spectral blue-shift is also observed in other per-fluorinated oligothiophenes or thiophenes et al.[87] In addition, either blue- or red-shifts are observed depending on the position of fluorine substitution, like in benzenes, azulene, distryrylbenzene and benzothiazolate species.[87]

The enhanced spin-orbital coupling in the fluorinated organometallic chromosphores could enlarge the rate of intersystem crossing so as to populate more triplet states contributing to transferring the energy into the lanthanide emitters. Moreover, the spectral red-shift can be achieved by controlling the position of fluorinated substitution and can move the excitation energy of the energy transfer for longer visible wavelengths.

1.2.3. Non-radiative energy transfer

(1). Dexter energy transfer

There are two main energy transfer mechanisms: Förster resonant energy transfer and Dexter energy transfer. The Förster mechanism extends over long distances (up to 1 nm) while the Dexter mechanism operates within a short distance (30 to 50 pm).[5]

Dexter energy transfer is a short-distance effect and obeys the electron exchange rules between electron orbitals, which is more complicated to understand since it is associated to a "many body" problem. This mechanism is implied by one experimental phenomenon that the sensitised phosphorescence or the energy transfer between the triplet excitons can arise from the exchange mechanism.[89] And, this mechanism differs from the dipole-dipole transfer since the transfer rate depends strongly on the donor-acceptor distance and is much shorter than the r^{-6} dependence.[5] Also, the efficiency of this mechanism is independent of the oscillator strength of the acceptor. The schematic diagram for the Dexter energy transfer is displayed in figure 1.2.

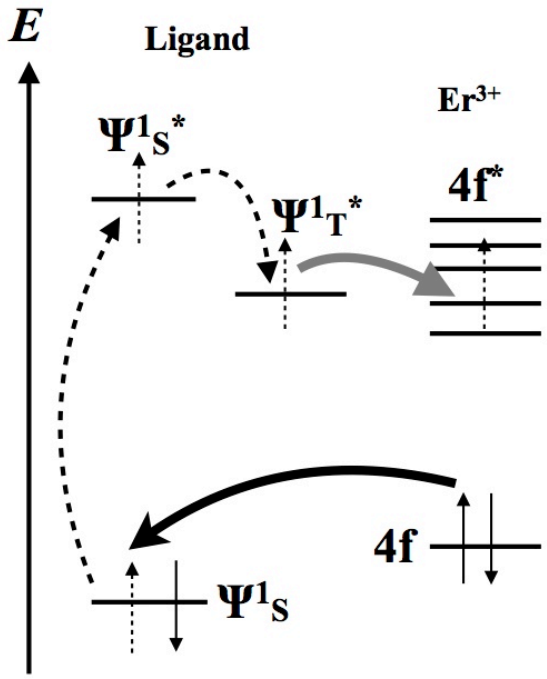

Figure 1.2. Dexter energy transfer

In an organic lanthanide system, owing to the shielding effect imposed by the outer shells on the 4f electrons, there would be the less Dexter energy transfer possible between the organic chromophores and lanthanide ions. So, it usually considers a pair of the isolated ligand- and metal-excited states in organic erbium complexes.

(2). Förster resonant energy transfer

Förster resonance energy transfer (FRET) refers to the non-radiative transfer process of an electronic excitation from a donor molecule *D* to an acceptor molecule *A*. The process is $D^* + A \rightarrow D + A^*$. This transfer arises from a dipole-dipole interaction between the electronic states of the donor

and the acceptor, and involves no emission and re-absorption. The transfer happens when the oscillations of an optically induced electronic coherence on the donor are resonant with the electronic energy gap of the acceptor after the excited donor absorbs the light. The acceptor is involved in the vibrational relaxation and luminescence, which is spectrally shifted from the fluorescence of the donor. This energy transfer process is displayed in figure 1.3.

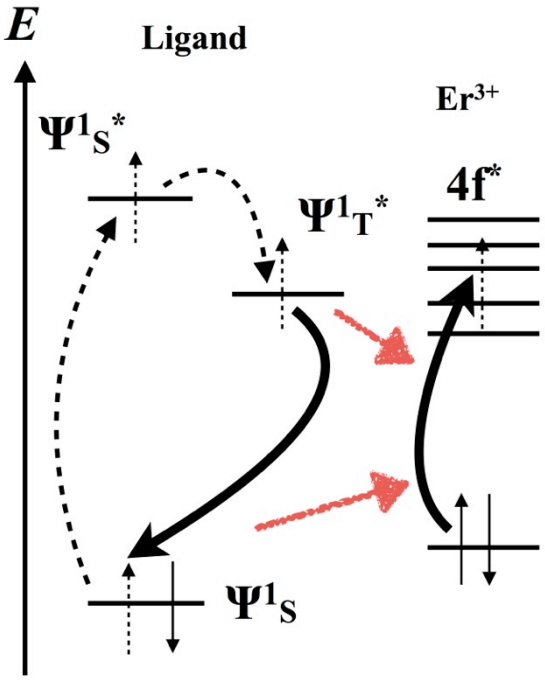

Figure 1.3. Förster resonance energy transfer

The Hamiltonian for the energy transfer process between the donor and acceptor can be defined by a combination of the Hamiltonian of the excited donor and the Hamiltonian of the excited acceptor. The perturbation calculation has been done and shows that the rate of the energy transfer is

proportional to r^{-6}, and depends on the oscillation strengths of the electronic transitions of the donors and acceptors.[5] The resonance for the energy transfer requires that the absorption, fluorescence and phosphorescence bands of organic chromophores or the coordinated ligands to overlap with some intrinsic absorption of the lanthanide ions.

1.2.4. Yield enhancement and sensitisation to erbium

(1). Examples of the sensitisation effect

In a sensitisation process, the Er^{3+} ion can be treated as an acceptor, and the organic chromophores can be treated as donors. Some organic chromophore-coordinated complexes of erbium have demonstrated the sensitisation effect at short UV wavelengths. For example, quinolinolate ligands have been known to be an efficient agent toward trivalent lanthanide ions, and have employed to prepare the materials for electroluminescence (EL) applications.[77,90,91] The emission of quinolinolate ligands was reported in AlQ_3 (Q is 8-hydroxyquinolinolate), of which the broad green-visible emission performed the extensive work for organic light-emitting diodes (OLED).[92] ErQ_3 based OLEDs were used to demonstrate the first electrically pumped Er-based on IR emitter at 1.5 μm wavelength. Besides, the terphenyl-based ligands,[24,93] polyaminocarboxylates[24,94], tropolonates[24], imidophosphinates[24,95] and other chelating agents have been investigated and demonstrated there is a

sensitisation effect for Er^{3+} ions.[23] And, some fluorinated complexes have been found for sensitising Er^{3+} ions, such as fluorinated β-diketonate,[96] tetrafluoronitrophenoxide,[97] and bis(pentapfluorophenyl)phosphinate.[98] In addition, a novel system with the energy transfer occurring from some isolated decafluorobenzophenone molecules into Er^{3+} ions has been found.[99] In this system, the erbium complexes and the organic chromophores are separately filled in the neighboured zeolite nano-channels.[99] These fluorinated organics provide the UV-sensitisation (< ~ 400 nm) for the coordinated Er^{3+} ions, or coordinated Er^{3+} show short lifetimes (< 100 μs).

(2). Hydrogenated quenching and fluorination

Most of organic erbium complexes provide very low quantum yields (< 0.01%) as the observed short lifetimes of the 1.5 μm emission (ns or μs), compared to the ~ 10 milliseconds of the theoretical lifetimes.[9] Such low efficiency is can be due to many mechanisms. In one mechanism, the energy migration between the excited $^4I_{13/2}$ levels of some neighboured Er^{3+} ions could occur in a way of non-radiative transitions to quench the excited states.[100,101] This quenching depends on the concentration of Er^{3+} ions, and the dilution technique could reduce this concentration quenching.[101,102] For example, it was observed that the lifetime at 1542 nm of Er^{3+} ions increased by ~ 7 times at 0.5% erbium concentration compared to the lifetime at 100%

erbium concentration, by diluting the concentration of Er^{3+} ions in the erbium bis(perfluoro-*p*-tolyl)-phosphinate complexes through doping variable concentrations of optically neutered coordinated yttrium ions.[101] Lower erbium concentration can isolate the neighboured Er^{3+} ions to a longer average distance between the Er^{3+} ions, so that the concentration quenching can be reduced. On the other hand, C-H, N-H or O-H bonds, in hydrogenated organic ligands, dramatically relax the energy of the excited state, because the IR emitting energy matches the second-order vibrational energy level of these hydrogenated chemical bonds.[103] This quenching can be also reduced by a deuteration process or by replacing coordinated hydrogen atoms with fluorine atoms. This is because the vibrational energies of C-D, O-D or C-F bonds are lower, and their second order or third order of vibrational energy levels do not match the IR emitting energy.[10,104] It has been reported that replacing C-H with C-D bond can increase the lifetime of Er^{3+} ions in the deuterated (hexafluoroacetylacetone) hfa^- ligands to 10 μs compared to ~ 2 μs for the Er^{3+} ions in the un-deuterated hfa^- ligands.[103] Fluorination is another common approach for removing the hydrogenated quenching by chemical syntheses upon keeping the stability of chemical structures. For instance, the fully fluorinated imidodiphosphinate ligands dramatically increase the lifetime of the Er^{3+} ions up to ~ 224 μs. And, the erbium complex of the bis(pentafluorophenyl)phosphinate ligands reaches the lifetime of ~ 440 μs

without any dilution.[11,98]

1.3. Organic erbium-doped gain medium

1.3.1. Telecommunication and erbium-doped fibre amplifier (EDFA)

Silica-based optical fibres have been widely used for modern telecommunication systems. Light, carrying data, propagates through the optical fibres over long distances, but will attenuate due to some optical losses, such as absorption or light scattering. A typical optical fibre has the Rayleigh scattering from visible bands to IR band, and there are some broad absorption bands allocating at ~ 0.95 μm, ~ 1.25 μm and ~ 1.4 μm wavelengths due to impurity absorption. The modern telecommunication wavelength is allocated in a third-window (conventional band or C-band) between ~ 1.5 μm and ~ 1.55 μm wavelengths, where the scattering and absorption losses are at their the lowest.[105] Despite the improved technique of modern optical fibres that have reduced the optical losses, the loss of the light power can still be 0.2 dB/km.[78] Therefore, an optical amplification is necessary and has been achieved by the erbium-doped fibre amplifiers (EDFA). EDFAs have been used for around 40 years and operate in the C-band because the Er^{3+} ion has an intrinsic emission over ~ 1.5 μm to 1.54 μm wavelength. The Er^{3+} ions in EDFAs are usually excited at 980 nm wavelength for the $^4I_{11/2}$ level and 1480 nm wavelength for the metastable ligand-field sub-level of the $^4I_{13/2}$ level, because the absorption

cross-sections of these transitions are relatively high.[4] The typical schematic diagram of an EDFA is shown in figure 1.4. The input signal is conveyed and coupled with the pump laser by the coaxial fibres into the erbium doped fibre amplifier.

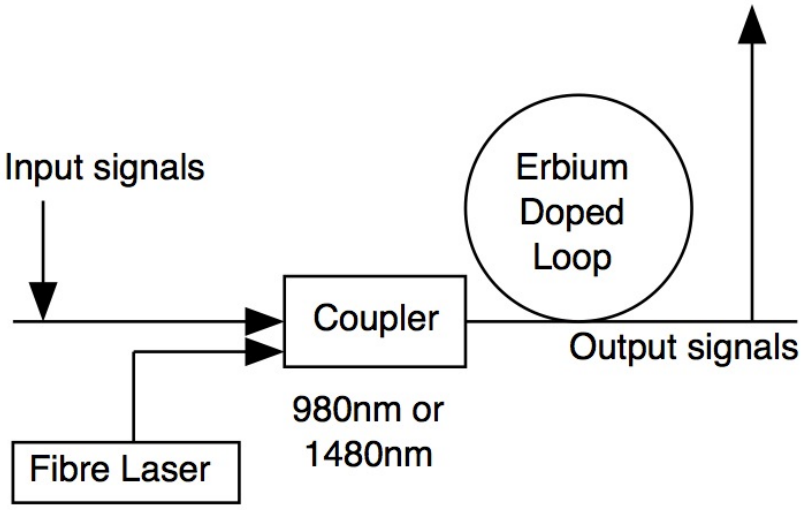

Figure 1.4. A typical EDFA

However, the low absorption cross-section of Er^{3+} ions must require a powerful laser with the power density of ~ kW/cm^2 to coaxially couple into a long length (1-3 meters) of erbium doped optical fibre, along with signal, to achieve population inversion, and then optical gain. A solution is to resort to polymer fibre in which the organic erbium complexes are doped in polymer organics. The advantages of the polymer fibre are more flexible, larger diameters, better coupling into an external facility, higher concentrations and enhanced absorption, and as a sequence, lower pump threshold.[105] For instance, the hydrogenated aromatic cyclic ligand provides

a 660-smaller pump-power threshold for optical gain. However, there are two disadvantages of polymers: the dispersion of the doped Er^{3+} ions could cause concentration quenching, and the existing C-H bonds quench the IR luminescence of the Er^{3+} ions.[105]

Another solution of erbium-doped silicon nano-crystals has drawn much attention, since the silicon nano-crystals, which are randomly dispersed in the matrix and spaced in the 2-5 nm distance, may have very low non-radiative internal recombination if properly prepared. So, there would be a sensitisation effect for the implanted Er^{3+} ions from the silicon nano-particles.[8,106,107] The erbium-doped silicon nano-crystal offers a visible sensitisation effect, however, only one or two gain measurements have been reported, and the effective absorption cross-section for Er^{3+} ions was estimated to be only a factor of 10 larger than the intrinsic absorption cross-section of Er^{3+} ions. Therefore, it is barely possible to achieve the optical gain with low exciting power in this system.[69,108]

1.3.2. Population inversion

In a two-level system, the population inversion occurs if the excited population at the high-excited state is more than the un-excited population at the ground state. The population inversion is necessary to obtain a stimulated emission contributing to optical gain. In a simulation emission, one molecule staying at the high-excited state could be perturbed by

another incident photon with the coherent energy so that it relaxes to the ground state by emitting a photon with the coherent energy coupled with the incident photon. So, the intensity of the incidence is magnified by the stimulated emission. Stimulated emission is the process by which an excited molecular state interacting with an incident photon of a certain frequency would relax to emit a new photon, and this new photon has the same phase, frequency, polarization and direction of incidence as the incident photon. As for the erbium-doped fibre amplifier, the pump laser is launched into the fibre in order to achieve the population inversion of the Er^{3+} ions, in order to amplify the input signal. The population inversion and optical gain with a low pump threshold (< 1 W/cm^2) for an erbium-doped amplifier require a long emission lifetime (milliseconds) and a large effective absorption cross-section (10^{-17} cm^2).

1.3.3. Optical waveguide

An optical waveguide is used to guide a light along a distance. The optical waveguide has two parts: there is a core part that has a higher refractive index and a cladding part that has a lower refractive index outside the core part. The propagating light undergoes total internal reflection at the interface between the core and cladding part so that the light can be guided.

Most materials for fabricating optical waveguides are generally

dielectric media because the dielectric media have high transparency, low absorption and isotropy. The dielectric slab waveguide is the easiest structure for guiding propagating light. The behaviour of the propagating light in the waveguide can be understood by the distribution of an electromagnetic field. The electric field and magnetic field of the wave are expressed, respectively, in the core part and cladding part according to the Maxwell equations[109] or Helmholtz equations[109], both of which are a set of partial differential equations from the foundation of classical electrodynamics, classical optics and electric circuits. The electromagnetic fields in the space have to satisfy the continuous boundary conditions at the interface between the core and cladding part. The propagating phase constant and transverse phase constant can be obtained by the continuous boundary conditions.[109] A transverse wave propagates through the core part and decays in the cladding part.

In addition, the behaviour of the propagating light can be investigated via an optical ray approach. The light is propagating through the core part by the internal total reflection. The phase shift at the interface has to satisfy the continuous boundary conditions.

Chapter 2. Instruments, Materials and Methodology

2.1. Instruments:

2.1.1. Film and waveguide fabrication

(1). Vacuum film deposition evaporator

The vacuum film deposition evaporator shown in figure 2.1 consists of a load-lock chamber loading the substrate, and one main chamber. The main chamber is separated with the load-lock chamber by a gate valve. Both the load-lock chamber and main chamber are pumped down to vacuum by an oil free Scroll vacuum pump and a turbo molecular pump. The transfer arm is used to transfer the substrates into the main chamber when the vacuum of the main chamber and load-lock chamber are down to ~ 10^{-5} to 10^{-7} mbar.

The mask cassette has three shelves and is designed to move vertically and rotate. Square or rectangular masks are designed and can be moved to each shelf. Both organic and metal source materials are filled into cylinder crucibles, which are usually made from alumina. Four crucibles are arranged below the mask cassette as organic sources, each of which is wrapped with circular metal heating wires. The temperature of the crucible is measured by a thermocouple touching the base outside the crucible. The sublimation of organics or metal will accelerate when the temperature rises, and sublimated molecules will deposit on the substrate placed on the mask

cassette. A quartz crystal sensor is used to monitor the deposition rate of thin film by measuring the frequency of quartz crystal lattice vibration, whilst both the rate and thickness data are displayed in a thickness and rate monitor. The heating power used is manually controlled. The shutter arm is used to cease the film deposition onto the substrate. The schematic of the vacuum film deposition evaporator is displayed in figure 2.1.

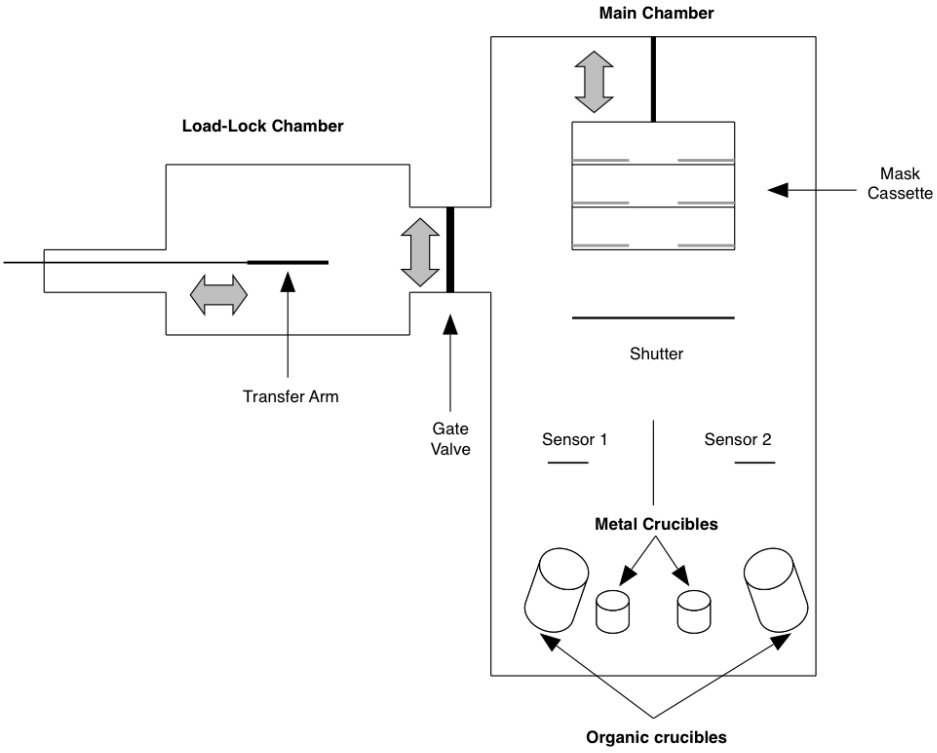

Figure 2.1. Vacuum film deposition evaporator

2.1.2. Laser and light resource

(1). Nd: YAG laser

The crystal Nd:YAG (neodymium-doped yttrium aluminium garnet: Nd:$Y_3Al_5O_{12}$) is a lasing medium for pulsed solid state lasers. Generally,

the crystalline YAG host is doped with around 1% neodymium by atomic ratio. Nd:YAG typically emits light at 1064 nm wavelength and absorbs light strongly at 739-760 nm and 790-820 nm wavelengths. Normally, a low current-density krypton flash-lamp is used to pump Nd:YAG to cause the 1064 nm emission and, in the Q-switching mode through the laser cavity, a pulse of 5 ns is achieved. The second harmonic and third harmonic generator crystals are used to generate the higher oscillator modes at a radiation of 532 nm and 355nm wavelength. The mode of the pump laser is adjusted with a repetition rate of 10 Hz and a maximum power of 100 mJ at 355 nm wavelength.

(2). Optical parametric oscillator system operator

The optical parametric oscillator system operator (OPO) is a high performance optical parametric converter for generating separated radiation over the visible and near IR spectral region. An optical parametric process is a three-photon interaction based on non-linear optics, where one photon (the pump photon) from a laser beam is converted into a pair of less energetic ones that generally have different energy. The higher energetic output beam is the “Signal” and the less energetic output beam is the “Idler”.

The optical parametric process occurs through an anisotropic crystal like Beta-Barium Borate, a transparent material that has different refractive

indices for different polarisations of light. The energy and polarisation of a photon can be symbolised by the wave vector **k**. The photon propagates through the crystal so that the signal and idler satisfy the relationship, like $\mathbf{k}_P = \mathbf{k}_S + \mathbf{k}_I$. The signal or idler can be filtered off via a polariser outside.

The spectral bandwidth of the generated radiation in an OPO process is determined by the energy conservation and momentum conservation relation. For example, in a Fabry-Perot-type OPO cavity, one of simplest optical cavities consisting of two opposing flat mirrors without any intra-cavity spectral narrowing elements, the spectral bandwidth primarily depends on the linewidth of the pump beam, angular divergence of the pump beam, phase-matched angular acceptance angle, phase matching type, output wavelength, proximity to the degenerate point, number of round trip inside the cavity and crystal length. In the case of type-I collinear phase matching, where the $\mathbf{k}_P = \mathbf{k}_S + \mathbf{k}_I$, the bandwidth of the generated radiation can be determined by the relation:

$$\Delta\omega_S \cong \frac{\pi}{L} \Big/ \left[\frac{\partial}{\partial \omega_S} \Delta(k_P - k_S - k_I) \right] \qquad (2\text{-}1)$$

The spectral linewidth of the generated radiation in an OPO process can be reduced by an injection seeding process, where a very narrow linewidth continuous wave or pulsed source is injected into an oscillator cavity and a few nJ of energy can control the linewidth of the generated radiation with several mJ output. Using spectral narrowing elements like diffraction grating in Littrow configuration or Fabry-Perot etalon alone or in

combination with grating in the OPO cavity, the spectral linewidth of the OPO output can be reduced.

Panther EX OPO provides excellent beam quality and low divergence, with the benefits, such as linewidth down to < 2.5 cm^{-1}, signal energies to > 100 mJ per pulse, full tuning range of 205 nm to 2550 nm, and scan speeds up to 10 nm/sec. The Panther OPO is designed to be attached directly to Continuum Powerlite series (injection seeded) pump lasers or it can be used in a stand-alone configuration with Surelite lasers. This compact and stable platform has separate output ports for the signal and idler output beams.

(3). Apex Arc lamp sources

A xenon arc lamp is a specialised type of gas discharge lamp, an electric light that produces light by passing electricity through ionised xenon gas at high pressure. Xenon arc lamps are usually used in research to stimulate sunlight. A Newport Apex Arc lamp source has a stable xenon lamp source of 150W white light output as a white light source. The collimated output diameter is 33 mm. A fused silica aspheric lens, which is transmissive from 200 nm to 2500 nm wavelengths, collects and collimates the radiation.

(4). Diode laser: 378/405 nm and 655 nm

Two Stradus^{TM} diode laser modules were used in the project, which operate at 378 nm or 405 nm wavelength. The transverse spatial mode is TEM_{00}. The linewidth is typically ~ 1 nm. The maximum digital modulation is 200 MHz and the digital rise time is < 2 ns. The beam diameter is ~ 0.8 mm to ~ 1.3 mm. The maximum output powers are 16 mW and 100 mW for 378 nm and 405 nm laser, respectively. The output power is adjusted using user interface software of Stradus^{TM} on PC where the minimum adjusting step is 1 mW.

A MRL-III-655 nm red diode laser was also used, which has a linwidth of ~ 10 nm. The transverse spatial mode is near TE_{00}. The maximum output is > 1000 mW. TTL modulation is in the range of 2-30 kHz. The mean diameter at aperture is ~ 5 × 8 mm.

(5). Function generator

TG1010 programmed 10M Hz DDS function generator can provide maximum 20Vp-p modulation function for TTL /COMS output. The rise and fall time of both positive and negative pulse is < 25 ns. The output impedance is 50/60 Ω. The function generator is used for modulating a diode laser beam at a frequency with the TTL/COMS output. The function generator provides the waveform types of sine, square, triangle, pulse, noise or programing arbitrary shape.

(6). Optical Chopper

An optical chopper is a device that uses a rotating blade to periodically interrupt the light beam in order to modulate the light beam to a specific frequency. Model 197 Dual Aperture Light Chopper has an outer sector f_1 that is set from 150 Hz to 3000 Hz, and an inner sector f_2 that is set from 15 Hz to 300 Hz. There are two Sync Out f_1 and Sync Out f_2, which employ 10 Vp-p square-wave output. The output impedance is 10K Ω.

2.1.3. Spectrograph and microscopic setup

(1). Spectrometer, monochromator and diffraction gratings

An ideal spectrometer consists of an entrance aperture, a collimating element, a dispersing element, a focusing element and an exist aperture. In a conventional spectrometer, the entrance aperture consists of a long narrow slit, and the shape and size depend on the particular means used to disperse the light. The collimating element is to make parallel all the rays passing through one point of the entry slit or field-stop. This element may be a lens or a mirror. The dispersing element is to alter the intensity that passes through the system, in a way that depends on the wavelength, such as diffraction gratings. The focusing element is to form an image of the entry field-stop at some convenient focal plane. And, the exit aperture is a stop at the focal plane, which transmits the light from the image that the

focusing system has formed. The exit field-stop could be defined by a detector. An ideal monochromator consists of mainly the same components as a spectrometer, while the difference is that the exit aperture in a monochromator is a real exit slit.

Diffraction gratings are manufactured either with the use of a ruling engine by burnishing grooves with a diamond stylus or holographically with the use of interference fringes generated at the intersection of two lasers beams.[110] Ruled gratings may be plano or concave, and possess grooves each parallel with the next. Holographic grating grooves may be either parallel or of unequal distribution in order to optimise system performance. Holographic gratings are generated on plano, spherical, toroidal and many other surfaces. The fundamental grating equation is given by

$$10^{-6} km\lambda = \sin\alpha + \sin\beta = 2\sin\left[\frac{\alpha+\beta}{2}\right]\cos\left[\frac{\beta-\alpha}{2}\right] \qquad (2\text{-}2)$$

where α is the angle of incidence, β is the angle of diffraction, k is the diffraction order, m is the groove density and λ is the wavelength in vacuum. If we define an angle $D_V = \beta - \alpha$, and D_V is known, β and α can be determined through the equation (2-2). The schematics of the grating configurations in a monochromeatic and a spectrometer are displayed in figure 2.2.

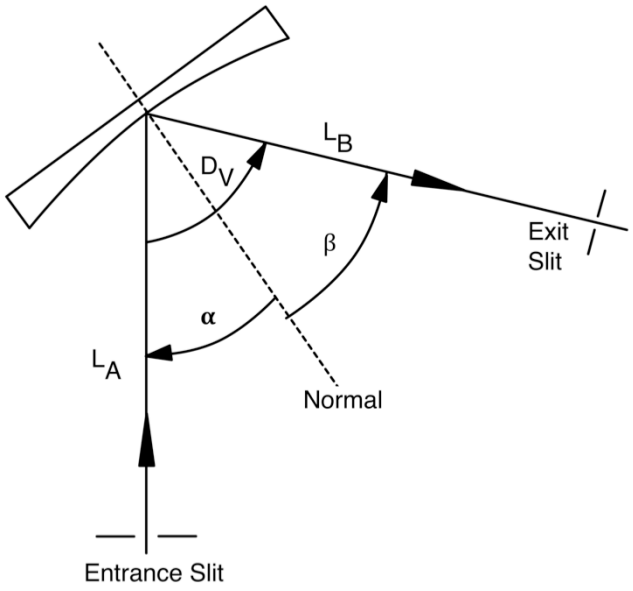

Figure 2.2.a. Monochromatic configuration

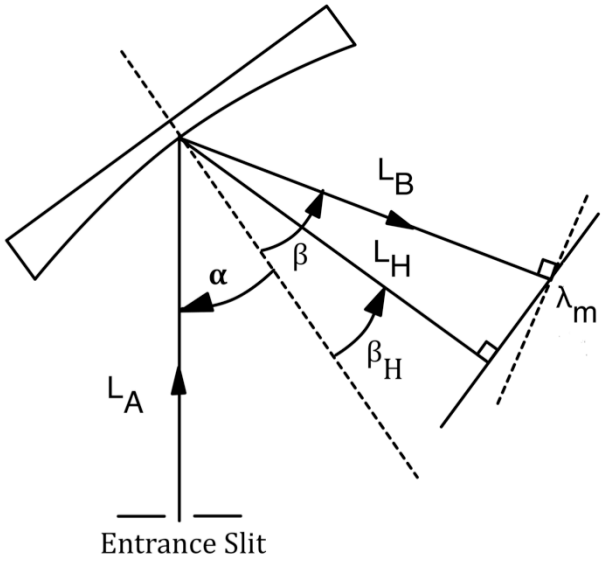

Figure 2.2.b. Spectrometer configuration

In figure 2.2, L_A is the entrance arm length, L_B is the exit arm length at λ_m, β_H is the angle between the perpendicular to the spectral plane and the grating normal, and L_H is the perpendicular distance from the spectral plane to grating.

Blazed gratings are manufactured to produce maximum efficiency at

designated wavelengths. Blaze is defined as the concentration of a limited region of the spectrum into any order other than the zero order. A grating may, therefore, be described as “blazed at 520 nm” etc. by appropriate selection of groove geometry.

(2). Linear dispersion, order, spectral ghost and spectral resolution

Linear dispersion defines the extent to which a spectral interval is spread out across the focal field of a spectrometer. The linear dispersion perpendicular to the diffracted beam at a central wavelength is given by

$$\frac{d\lambda}{dx} = \frac{10^6 \cos\beta}{km\mathrm{L}_\mathrm{B}} \ (\mathrm{nm/mm}) \qquad (2\text{-}3)$$

The equation suggests that linear dispersion varies directly with cos β, and inversely with the exit path length $\mathrm{L_B}$ (mm), diffraction order *k* and groove density *m* ($\mathrm{mm^-}$ or 10^{-6} $\mathrm{nm^-}$). In a spectrometer, the linear dispersion for any wavelength other than the wavelength normal to the spectral plane will be modified by the difference of the angles β_H and β, for the example, the spectral plane showing a flat field used with a linear diode array derives the linear dispersion

$$\frac{d\lambda_m}{dx} = \frac{10^6 \cos\beta \cos^2(\beta_\mathrm{H} - \beta)}{km\mathrm{L}_\mathrm{H}} \ (\mathrm{nm/mm}) \quad (2\text{-}4)$$

If the angles of α and β, the grating of given groove density are given, the relation of the equation (2-2) turns to be *k*λ = constant, so that if the diffraction is doubled, λ is halved. For example, a light source emits a

continuum of wavelengths from 20 nm to 1000 nm, at the physical location of 600 nm wavelength in first order, the wavelengths of 300 nm, 200 nm and 150 nm will also be present and available to the same detector. In order to monitor only 800 nm wavelength, filters must be placed to eliminate the higher order.

If the diffraction grating has periodic ruling errors, a ghost will be focused in the dispersion plane, and the ghost intensity is given by $I_G \propto m^2k^2e^2\pi^2$, where e is the error in the position of the grooves. Generally, holographic gratings show weak ghosts because there are less periodic ruling errors and often represent the best solution to ghost problems.

Bandpass and resolution are used to qualify the ability of a monochromator or spectrometer to separate adjacent spectral lines. The bandpass is the spectral interval that may be isolated. This depends on many factors including the width of the grating, system aberrations, spatial resolution of the detector and entrance and exit slit widths. In reality, spectrometers are not perfect and produce an apparent spectral broadening of the purely monochromatic wavelength. The line profile has finite width and is known as the instrumental bandpass. The shape of the bandpass is a function of various parameters, such as the width of the entrance slit, the width of the exit slit or of one pixel in the case of a detector and the diffraction phenomena. For example, the smaller slit width will make the spectral interval to spread less and reduce the spectral bandpass. This

means the observed peak height is less than the true peak height. However, as for lanthanide ions, most absorption peaks are monochromatic, so the variation from observed peak height to true peak height is less than 0.5% even at large slit width.[22]

(3). Jobin Yvon Horiba Triax series spectrometers and Hitachi U-3000 spectrometer

The Jobin Yvon Horiba Triax 550 spectrometer is used for dispersing monochromatic lights. The grating of 600 lines/mm, blazed at 1 μm wavelength, is used for the dispersion over IR bands, and the grating of 1200 lines/mm, blazed at 550 nm wavelength, is used for the dispersion over UV/Visible bands. The slit width of the entrance and exit are usually adjusted to be the same. The slit width can be adjusted from 20 μm to 2 mm. The linear dispersion is 1.55 nm/mm at 1200 lines/mm grating.

The Jobin Yvon Horiba Triax 180 spectrometer is used as a monochromator for dispersing monochromatic lights. The grating of 1200 lines/mm, blazed at 550 nm wavelength, is also used for dispersing UV-Visible monochromatic lights. The slit width of both entrance and exit are adjusted to the maximum width of 2 mm. The linear dispersion is 3.6 nm/mm at 1200 lines/mm grating.

The Hitachi U-3000 spectrometer has a measurable wavelength range of 190 nm to 900 nm. The wavelength accuracy is ± 0.1 nm after 656.1 nm

wavelength calibration. The spectral bandpass can be 0.1, 0.5, 1, 2, 4, 5 nm, and the wavelength scan speed can vary from 1.5 nm/min to 2400 nm/min. The photometric range is from – 3.8 to 3.8 abs with the minimum accuracy of ± 0.006 abs. The light source is a deuterium lamp for UV region and a tungsten iodine lamp (50W) for visible region. The light signals are detected by the internal photomultiplier. The spectra were extracted using the software on a PC.

(4). Home-made single-beam micro-absorption setup

In this home-made single-beam micro-absorption setup, the optical setup is built from some microscopic objective lens for focusing the light beam to be size of micro-meter squares. A xenon or tungsten lamp is used as the light source in absorption measurements. The 190 Model optical chopper is used to modulate the light beam. The randomly oriented sample crystal is flatly deposited on a quartz substrate and focused by a Cassegrain reflective objective lens (f = 13 mm, 15 × magnification, 24 mm working distance). A Mitutoyo objective lens (f = 10 mm, 20 × magnification, 20 mm working distance) captures the light passing through the sample, which is focused into the slit entrance of a Triax 550 spectrometer. The microscopic setup is displayed in figure 2.2.

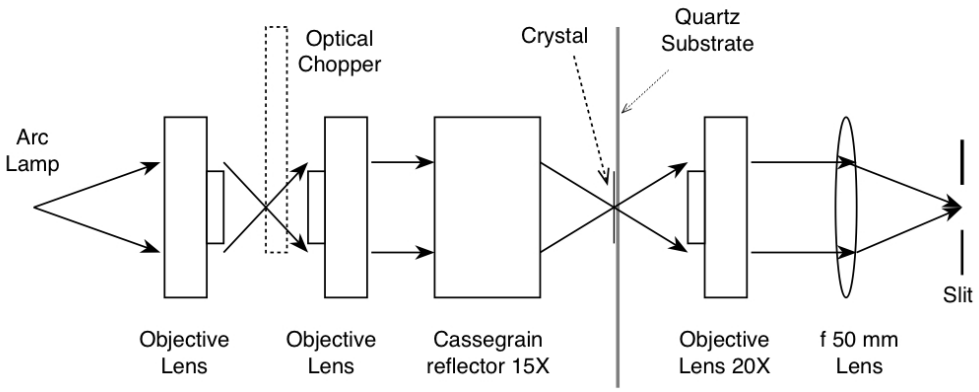

Figure 2.2. Home-made single-beam micro-absorption setup

(5). Ellipsometer

An ellipsometer is an optical instrument used to investigate the dielectric characteristics of a thin film. The ellipsometer measures the complex reflectance ratio, ρ, of a system, which is parameterised by the amplitude component Ψ and the phase difference Δ. The two polarisations of incident and reflected light beam are decomposed into *s* and *p* components. The amplitudes of the *s* and *p* components, after reflection and normalisation to their initial value, are denoted by r_s and r_p, respectively. The ellipsometer measures the ratio of intensities, where $\rho = r_p / r_s = \tan(\Psi) \exp(i\Delta)$. Thus, tan(Ψ) is the amplitude ratio upon reflection and Δ is the phase shift.

Generally, the measured Ψ and Δ cannot be converted directly into the optical constants unless the measured film is isotropic, homogeneous and infinitely thick. Therefore, usually, a proper model is required for fitting the results in order to obtain the reasonable thickness parameters and

optical constants of the sample.

The UVISEL spectroscopic ellipsometer has a spectral range from VUV (vacuum UV) to NIR, which is from 142 nm to 2100 nm wavelength consisting of five configurations. The instrument consists of a xenon light source, HR460 monochromator, MWL spectrograph, HV power supply, graphics monitor, autocollimator and motorised stage. The thickness measuring range for thin film is 1 Å to 30 μm. The angles of the incident light and spectrograph are fixed to 70º to the horizontal. The UVISEL is controlled by the DeltaPsi2 software platform that provides a complete measurement and modelling package to address both routine and advanced thin film applications.

2.1.4. Photon detector

(1). Photomultiplier tube (PMT)

A photomultiplier tube is an instrument for converting a photon signal into electricity by the photoelectric effect in a photocathode. Generally, photomultipliers consist of a photocathode, an electron multiplier and an anode. The electron multiplier consists of some electrodes called dynodes. Incident photons strike the photocathode material, with electrons being produced as a sequence of the photoelectric effect. These electrons are directed by focusing electrodes toward the electron multiplier. The signal is magnified between the dynodes and the anode.

A Hamamatsu 9113B PMT is used for multiplying the photoelectric signal at visible range from 350 to 800 nm wavelength. The output resistance is 10 MΩ. A Hamamatsu R5509-72 nitrogen-cooled detector, which is cooled to –80°C, is used for signals in the IR range of 800 nm to 1650 nm wavelength. The output resistance can be separately set to 50 Ω, 1 KΩ, 100 KΩ and 10 MΩ.

(2). Silicon Photodiode Detector

A silicon photodiode is a photo-detector, converting light into a current signal based on the mechanism of inner photoelectric effect in a silicon semiconductor. The Newport 818-UV enhanced silicon detector is used to measure the intensity of light from 200 - 1100 nm wavelength. The calibration of responsivity, which is a relationship between converted current versus wavelength over the whole spectral range, is provided by the supplier. The linearity of the response to the capacity of measuring light power is ± 0.5 %. Its maximum measurable power density is ~ 30 W/cm^2.

2.1.5. Data extractor and analyser

(1). Oscilloscope

The oscilloscope is used for recording the time-resolved spectra in this thesis. The reason that we can obtain stable time-resolved spectra is based on the “Trigger” function. The trigger gives a referenced time point for the

oscilloscope so that the observed signal can be locked by the reference signal. The reference with a frequency can lock an observed signal that is modulated with the same or integer frequency of the reference. The trigger level coupled with the “slope” defines the pattern that must be sensed by the trigger circuit before it will start the trace. A “positive slope” means that the trigger level must be crossed going from a lower to a higher voltage, and a “negative slope” means that the trigger level must be crossed going from a higher to a lower voltage.

RC-circuit response is an artificial phenomenon that needs to be avoided for correcting real time-resolved data. The simplest RC circuit is a capacitor and resistor in series. When the RC circuit is charged, the voltage across the capacitor is time dependant, since the current through capacitor and resistor needs to be equivalent in the series. If the input is a low-frequency square wave, the ratio of the output amplitude V_{out} to the input amplitude V_{in} would depend on the frequency f according to the relation of $V_{out} / V_{in} = [\ 1 + (\ 2\pi f \mathrm{RC}\ )^2]^{-1/2}$. The can be obtained in the way of measuring the lifetime of the decay. And, this RC constant is associated with impedance of the detector, the external electric amplifier and impedance of the oscilloscope.

The vertical resolution of an oscilloscope can be identified by bit number, which refers to the conversion of an analog voltage to a digital value in a computer. For example, the 2-bit digital value can represent 2^2

different numbers, and the voltage input range of 0 to 10 volts is divided into 4 pieces giving a voltage resolution of 2.5 volts per bit.

The oscilloscope employed in experiments is a LeCroy Waverunner LT372 with 500 MHz maximum (20 ns/div time-base minimum). The vertical resolution can be 8-bits, and the minimum vertical sensitivity is 2 mV/div, in which it can represent 2^8 different numbers. The RC response time is measured as < 5 ns, ~ 50 ns, ~ 4 μs and 70 μs for 50 Ω, 1K Ω, 100K Ω and 10M Ω resistors of PMT with 1M Ω impedance on the oscilloscope, respectively.

Another oscilloscope employed in gain measurement is the LeCroy Waverunner HD4000 with 5 GHz maximum (20 ps/div time-base minimum). The vertical resolution can be up to 15-bits, and the minimum vertical sensitivity is 1 ms/div, in which it can represent 2^{15} different numbers.

(2). Lock-in amplifier

A lock-in amplifier consists of a RC circuit filter, phase-sensitive Detector (PSD) and signal amplifier. It is designed to extract a signal that has a specific frequency based on the Fourier transfer process.

The lock-in measurement requires a frequency reference. Typically, a signal is modulated at a fixed frequency and the lock-in amplifier detects the intensity of the modulated signal at the reference frequency. It is

reasonable to explain the mathematical process through a sine-function input signal, whilst the square-wave signal follows the same mathematical mechanism.

If the signal is $V_{sig}\sin(\omega t + \theta_{sig})$, of which V_{sig} is the amplitude of input voltage, ω is the modulated frequency of input signal and θ_{sig} is the phase of signal, the lock-in amplifier generates the reference signal with external or internal reference ω_r by $V_L\sin(\omega_r t + \theta_r)$. Simply, a lock-in amplifier magnifies the signal and then multiplies it by lock-in reference using a PSD. The output of the PSD is the product of a multiple sin-function: $V_{psd} = V_{sig} V_L \sin(\omega t + \theta_{sig})\sin(\omega_r t + \theta_r) = 1/2\ V_{sig} V_L \cos([\omega - \omega_r]t + \theta_{sig} - \theta_r) - 1/2\ V_{sig} V_L \cos([\omega - \omega_r]t + \theta_{sig} + \theta_r)$. So, the output of the PSD is two AC signals, of which one is at the difference of frequencies and the other is at the sum of frequencies. The two AC signals pass through a low pass RC circuit filter in order to remove all AC signals. Once the modulated frequency is equal to the reference frequency, the difference in frequencies goes to zero so that there is a DC signal left that would not be removed by a low-pass RC filter. The magnitude of DC is proportional to the magnitude of input signal. The model 5029 single phase lock-in amplifier and model 7265 DSP lock-in amplifier are used in the measurements.

2.2.Materials

2.2.1. Acetyacetonate and hexafluoroacetylacetonate series

(1). Erbium(III) acetylacetonate dihydrate: $Er(acac)_3(H_2O)_2$

97% purified $Er(acac)_3(H_2O)_2$ powder and ethanol were obtained commercially from Sigma-Aldrich Chemicals. 51 mg $Er(acac)_3(H_2O)_2$ powder was dissolved in 20 mL 99.8% ultra-gradient ethanol (Sigma-Aldrich). 44mg Pink needle-like crystals of $[Er(acac)_3(H_2O)_2](H_2O)(CH_3CH_2OH)$ were formed via slow solvent evaporation at room temperature.

(2). Erbium(III) (hexafluoroacetylacetonate)-dihydrate: $Er(hfa)_3(H_2O)_2$

118 mg $Er(hfa)_3(H_2O)_2$ powder synthesised by Dr. Rendy Tan according to the literature[103] was dissolved in 10 mL 99.8% ultra-gradient methanol. 100 mg pink needle-like crystals were formed via slow evaporation at room temperature.

(3). Cesium tetrakis (hexafluoroacetylacetonate)-Erbium(III): $CsEr(hfa)_4$

51 mg $CsEr(hfa)_4$ powder synthesised by Dr. Rendy Tan according to the literature[103] was dissolved in 20 mL 99.8% ultra-gradient methanol (Sigma-Aldrich). 44 mg pink flaky crystals were formed via slow evaporation at room temperature.

2.2.2. (Phenyl)imidodiphosphinate and (fluorophenyl)imidodiphosphinate series

(1). Erbium(III) (tetraphenylimidodiphosphinate): $Er(tpip)_3$

$Er(tpip)_3$ was synthesised by Dr. Yu Peng in Chemistry, QMUL according to the instruction in the literature.[95] 15 mg $Er(tpip)_3$ powder was dissolved in 4 mL 99.8% ultra-gradient acetonitrile. 10 mg pink flaky crystals were formed via slow evaporation at room temperature.

(2). Erbium(III) tetrakis(pentafluorophenyl)imidodiphosphinate:$Er(ftpip)_3$

$Er(ftpip)_3$ was synthesised and purified under vacuum as performed by Prof. Youxuan Zheng in Chemistry, Nanjing University in the literature.[11,20] 52.4 mg pure $Er(ftpip)_3$ powder was dissolved in 3 mL dimethyl sulfoxide (DMSO) (Sigma-Aldrich). 52 mg pink crystals precipitated at room temperature after slow evaporation for a week and then were filtered off.

2.2.3. Zinc(II) tetrafluoro(dydroxyphenyl)tetrafluorobenzothiazoles: $Zn(F\text{-}BTZ)_2$

The chemical, structural and optical characteristics of $Zn(F\text{-}BTZ)_2$ have been investigated and reported in the literature.[111] The yellow purified powder of $Zn(F\text{-}BTZ)_2$ was synthesised and was obtained by Dr Zhe Li through sublimation under the vacuum of 10^{-6} mbar at the temperature of ~

170 °C -270 °C.

2.2.4. The strategy to prepare samples

(1). The non-fluorinated and perfluorinated erbium complexes

The study for spectral transitions of Er^{3+} ions doped in acetylacetonate-related ligand groups via Judd-Ofelt theory has been undertaken by some researchers, and the relationship among the corresponding Judd-Ofelt parameters, the number of coordination ligands and covalent bonds have also been discussed.[36] The hexafluoroacetylacetonate (hfa^-) ligand is the fluorinated version of acetylacetonate ($acac^-$), in which there is the same coordinated erbium-oxide bond. The proper crystallisation would obtain the same amount of crystal hydrate for the $acac^-$ and hfa^- related complexes. $CsEr(hfa)_4$ has four coordinated hfa^- ligands without coordinated hydrates. $Er(ftpip)_3$ is one of the organic fluorinated erbium complexes, which can be sublimated under vacuum and has long-lived lifetime at ~ 1.5 μm emission.[11] Again, $Er(tpip)_3$ is the non-fluorinated version of $Er(ftpip)_3$. Chemical, structural and spectral characteristics of $Er(ftpip)_3$ and $Er(tpip)_3$ complexes have been reported in the literature.[20,95]

(2). Crystals in erbium complexes

Solvents with hydrogenated molecules do not give accurate absorption

measurements for Er^{3+} ions in the IR band because these hydrogen-correlating molecules have an intense IR absorption background, meaning the IR absorption of Er^{3+} ions can barely be resolved. A compressed potassium bromide salt (KBr et al) pellet is a solid-method for IR absorption measurement, but light scattering is large, particularly for UV-visible bands, due to the non-uniform distribution of the sample powder and KBr powder in the compressed pellets. Furthermore, the concentration of Er^{3+} ions in the optical path is difficult being estimated due to the non-uniform and uncertain distribution of the sample powder in the pallets, and the concentration value being crucial to calculate the absolute line strengths of the electronic transitions. On the contrary, if the crystal samples are used for the absorption measurement and Judd-Ofelt analysis, the concentration of Er^{3+} ions in specific chemical and crystal structures can be calculated precisely from x-ray crystallographic data, in order to identify the spectral characteristics related to the corresponding chemical structure.

(3). Selection of solvents

The selection of solvents used to dissolve organic erbium complexes for absorption measurements needs consideration in terms of the solubility for the individual complex. Methanol, dimethyl sulfoxide (DMSO) and tetrahydrofuran (THF) were used to prepare solutions of dissolved

$Er(acac)_3(H_2O)_2$, $Er(hfa)_3(H_2O)_2$ and $CsEr(hfa)_4$. Chloroform was chosen to dissolve $Er(tpip)_3$ and DMSO was chosen to dissolve $Er(ftpip)_3$.

The acidity or basicity of solvent must be a consideration. Methanol, DMSO and chloroform are similar neutral solvents, and THF is a strong Lewis basic solvent. Moreover, the cut-off wavelength of a solvent is also a consideration. Each organic solvent has a UV-visible cut-off wavelength, below which the solvent absorption may be unacceptable, since a charge-transfer can occur between dissolved molecules and solvent molecules. The cut-off wavelengths for methanol, DMSO, THF and chloroform are below ~ 300 nm, which is lower than the $^4I_{15/2} \rightarrow {}^4G_{11/2}$ transition at ~ 378 nm wavelength for an Er^{3+} ion.

(4). $Zn(F\text{-}BTZ)_2$ acting as an organic sensitiser

Zinc(II) bis(hydroxyphenyl)benzothiazolate has been established as an excellent electroluminescence material when used in an organic light-emitter device (OLED). The molecular structure, electronic characteristic and electron transport properties of the complex have been investigated.[111] The electronic π-π^* stacking is on the two benzothiazolate ligands, contributing to the optical and electronic spectroscopy of the complex.[112] In order to employ the substituted complexes for sensitising an Er^{3+} ion without introducing IR quenching, the fully fluorinated substituted $Zn(F\text{-}BTZ)_2$ complex was used. The molecular, electronic and

photo-physical characteristics of $Zn(F\text{-}BTZ)_2$ have been studied recently in the literature.[111] The chemical synthesis and the x-ray crystallographic data for the complex have been well introduced[111, 113]. The chemical formula of $Zn(F\text{-}BTZ)_2$ is displayed below, which is taken from the literatures[111, 113].

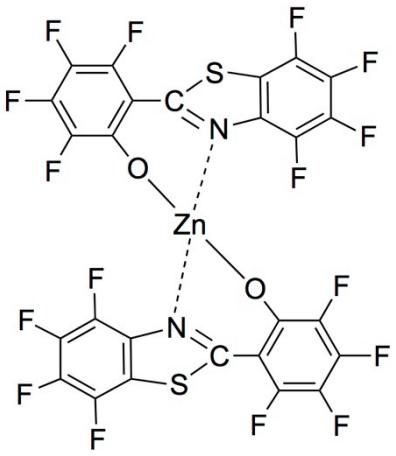

The fluorescence and phosphorescence characterisation of $Zn(F\text{-}BTZ)_2$ have been reported by the electroluminescence in OLEDs.[113] In an electroluminescence that is different with photoluminescence, both singlet and triplet excitons are formed immediately since the lowest unoccupied molecular orbital (LUMO) and the highest occupied molecular orbital (HOMO) are populated by electronic transportation in OLEDs through the injected electrons and holes. Statistically three triplet excitons will be formed for each singlet excitons as electrons and holes are fermions with half integer spin. The fluorescence and phosphorescence can occur through the combination of electrons and holes in singlet and triplet excitations, respectively. The enhanced π-π_F stacking in this complex provides lower LUMO and HOMO levels, lower the energy gap between LUMO and HOMO and enhanced intersystem crossing etc. These give broader

luminescence bandwidth, lower energies of luminescence, and stronger triplet emissions for $Zn(F\text{-}BTZ)_2$, compared to the hydrogenated substitutions. The reported quantum yield of fluorescence decreased with fluorination. The possible reason could be that the fluorination-enhanced triplet population quenches the emission of singlet states.

2.2.4. X-ray diffraction data, crystallography and refractive indices

(1). X-ray diffraction data

Single crystal x-ray diffraction (XRD) studies were performed on all crystals prepared by re-crystallisation and the data is summarised in table 2.1. Molecular and crystal structures were solved and refined using the Bruker SHELXTL Software. The quality of the refined structure is based on the final R indices factor. Generally, the smaller R-factor and wR2-factor means a better quality of refined model. The x-ray crystallographic data of $Cs[Er(hfa)_4]$, $Er(hfa)_3(H_{2O})_2$, $Er(tpip)_3$, $Er(ftpip)_3$, $Zn(F\text{-}BTZ)_2$ and $[Er(acac)_3(H_2O)_2](H_2O)(CH_3CH_2OH)$ crystals are listed in table 2.1. In the tables, the parameters a, b, c are three lattice constants (the lengths of the basis vectors **a**, **b**, **c**), and the parameters α, β, γ are the angle between the basis vectors **b** and **c**, the angle between the basis vector **a** and **c**, and the angle between the basis vector **a** and **b**. V is the lattice volume and Z is the molecular number in a lattice.

Formula	$C_{20}H_4CsErF_{24}O_8$	$C_{15}H_7ErF_{18}O_8$	$C_{17}H_{33}ErO_{10}$
	$Cs[Er(hfa)_4]$	$Er(hfa)_3\ (H_2O)_2$	$[Er(acac)_3(H_2O)_2]$ (H_2O) (CH_3CH_2OH)
Formula weight	1128.40	824.47	564.69
Temperature	160(2) K	120(2) K	100(2) K
Crystal system	Orthorhombic	Triclinic	Monoclinic
Space group	Pbcn	P-1	P21/n
a	8.534(3) Å	9.90590(10)Å	10.4187(6) Å
b	21.189(5) Å	11.5257(2)Å	19.6076(9) Å
c	17.251(8) Å	12.3039(2)Å	10.9402(6) Å
α	90˚	67.9090(10)˚	90˚
β	90˚	73.7910(10)˚	91.2350(10)˚
γ	90˚	76.0860(10)˚	90˚
V	3119(2) $Å^3$	1235.32(3) $Å^3$	2234.4(3) $Å^3$
Z	4	2	4
Density (calculated)	2.403 mg/cm^3	2.217 mg/cm^3	1.679mg/cm^3
Absorption coefficient	4.027 mm^{-1}	3.572 mm^{-1}	3.803 mm^{-1}
Reflections collected	3057	27543	28813
Independent reflections	2890 [R(int) = 0.0102]	5641 [R(int) = 0.0382]	5517 [R(int) = 0.0170]
Final R indices [I > 2 s(I)]	R1 = 0.0430 wR2 = 0.1044	R1 = 0.0265 wR2 = 0.0670	R1 = 0.0149 wR2 = 0.0312

Table 2.1.a. X-ray diffraction data of $[Er(acac)_3(H_2O)_2](H_2O)(CH_3CH_2OH)$, $Cs[Er(hfa)_4]$ and $Er(hfa)_3(H_2O)_2$,

Formula	$C_{72}H_{60}ErN_3O_6P_6$	$C_{72}ErF_{60}N_3O_6P_6$	$C_{28}F_{16}N_6S_4Zn$
	$Er(tpip)_3$	$Er(ftpip)_3$	$Zn(F\text{-}BTZ)_2$
Formula weight	1416.31	2495.83	917.95
Temperature	100(2) K	100(2) K	100(2) K
Crystal system	Triclinic	Monoclinic	Triclinic
Space group	P-1	P2/n	P-1
a	14.3290(3) Å	12.3554(5) Å	10.281(5) Å
b	14.82674(4) Å	13.8738(6) Å	10.321(5) Å
c	17.7919(4) Å	23.3920(10) Å	14.776(5) Å
α	89.8600(10)˚	90˚	79.798(5)˚
β	76.1180(10)˚	90.9740(10)˚	88.735(5)˚
γ	62.7920(10)˚	90˚	89.951(5)˚
V	3238.21(16) $Å^3$	4009.2(3) $Å^3$	1542.7(12) $Å^3$
Z	2	2	2
Density (calculated)	1.453 mg/cm^3	2.067 mg/cm^3	1.976 mg/cm^3
Absorption coefficient	4.251 mm^{-1}	1.363 mm^{-1}	4.887 mm^{-1}
Reflections collected	39012	25558	14955
Independent reflections	10829 [R(int) = 0.0289]	9877 [R(int) = 0.0148]	5201 [R(int) = 0.0282]
Final R indices [I > 2 s(I)]	R1 = 0.0222 wR2 = 0.0587	R1 = 0.0232 wR2 = 0.0562	R1 = 0.0269 wR2 = 0.0690

Table 2.1.b. X-ray diffraction data of $Er(ftpip)_3$, $Er(tpip)_3$ and $Zn(F\text{-}BTZ)_2$

(2). X-ray crystallography

The crystallographers and structural formulas of the studied crystals are displayed in figure 2.3.

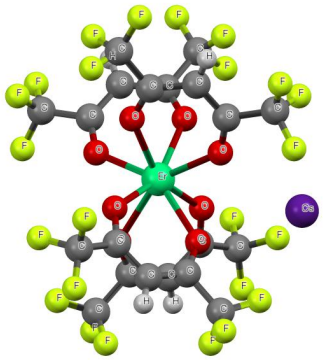
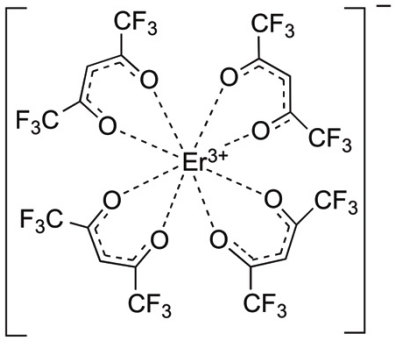

Figure 2.3.a. Molecular structure and chemical formula of $[Er(hfa)_4]^-$ in Cs^+ ion environment. Cs^+ ion has coordination with Er^{3+} but electrostatic force with $[Er(hfa)_4]^-$

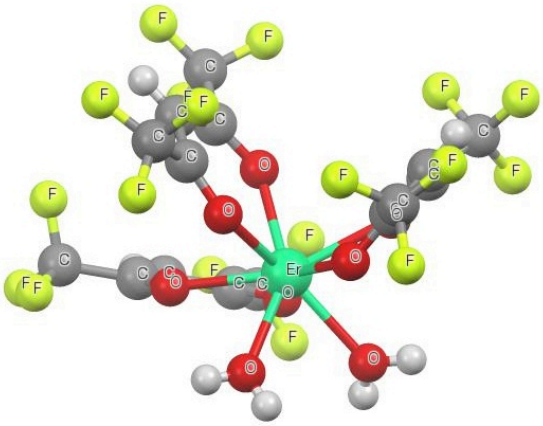
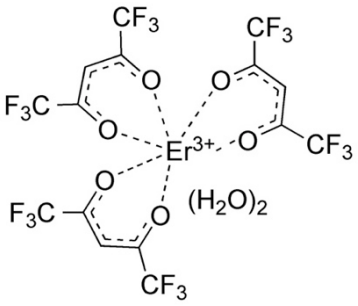

Figure 2.3.b. Molecular structure and chemical formula of $Er(hfa)_3(H_2O)_2$

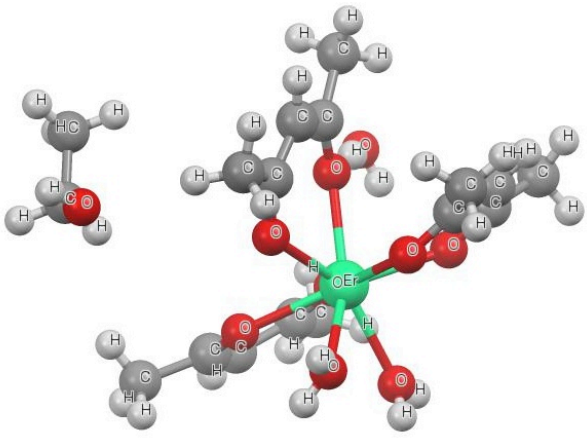
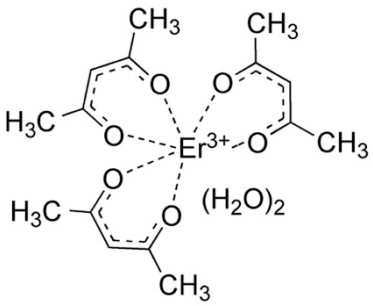

Figure 2.3.c. Molecular structure and chemical formula of $Er(acac)_3(H_2O)_2$

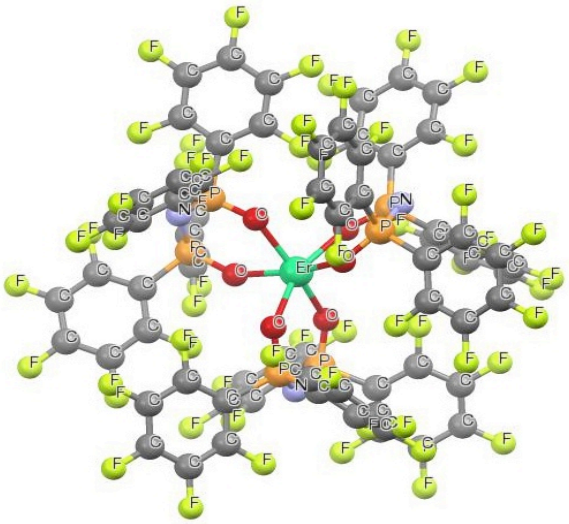

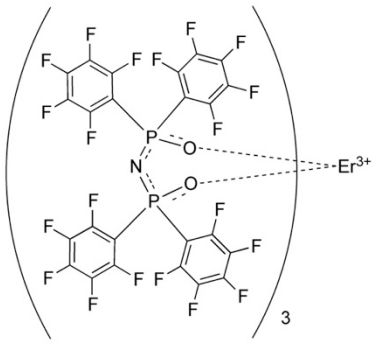

Figure 2.3.d. Molecular structure and chemical formula of $Er(ftpip)_3$

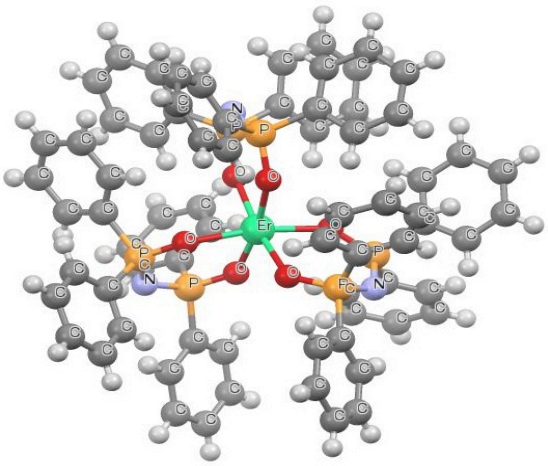

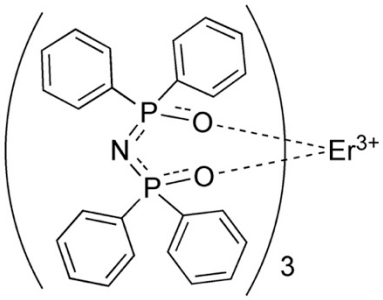

Figure 2.3.e. Molecular structure and chemical formula of $Er(tpip)_3$

(3). Refractive indices of samples

In Chapter 1, the dipole strength of an induced electric dipole transition is proportional to the square of the electric field at the lanthanide site. However, in absorption studies, the lanthanide ions are embedded in a dielectric medium, and they not only feels the radiation field of the incident light, but also the field from the dipoles in the medium. The total field

consisting field of the dipoles and the electric field E of the incident light is called the effective field E_{eff}. Therefore, the dipole strength of the lanthanide ions in a dielectric medium needs be multiplied by a factor $(E_{\text{eff}} / E)^2$. The factor $(n^2 + 2)^2 / 9$ is the Lorentz local field correction,[27] which is the first approximation of $(E_{\text{eff}} / E)^2$, and accounts for dipole-dipole transition. For an absorption process, the transition probability has to be divided by the photon flux. The flux in dielectric medium is $(v / 4\pi)n^2E_0^2$, compared to $(c / 4\pi)E_0^2$ in vacuum, where n is the refractive index, c is the speed of light in vacuum, v is the speed of light in dielectric medium, and $v = c / n$. Therefore, an additional factor $1/n$ has to be included in the expression the correction factor χ_{ED} for induced electric dipole transitions, so that the correction factor becomes $\chi_{ED} = (n^2 + 2)^2/ 9n$ for absorption, which also refers to the equation (1-1) and (1-4)[22]. The correction factor is valid for lanthanide ions in an isotropic dielectric medium. It is assumed that the centres are not in resonance with the host medium, and the lanthanide ions are so far apart that interactions among them can be neglected. Each lanthanide ion can be treated as an isolated centre in a medium characterised by a real refractive index. For n, the value of the refractive index n_{D} for the sample illuminated by the sodium D line (589.3 nm).[22]

Refractive indices of solvents and samples need to be reported or measured, since the refractive index is involved in calculating Judd-Ofelt

parameters and designing optical waveguides.

The refractive indices of prepared solutions take the values of the corresponding solvents at room temperature. In solutions, solvent molecules are populous compared to the dissolved complex molecules, so that the dielectric permittivity of the solvent should be equivalent to the corresponding solution. The refractive indices of solvents and the variation < 5% for the refractive index of each solvent are referred from the supplier (Sigmal-Aldrich).

As for crystal samples, the average refractive indices were estimated by the Becke line test with calibrated liquid (Cargille), where the variation of estimation is < 3%. The Becke line test is a technique that helps determine the relative refractive index of two materials. For dipping the crystal in the calibrated liquid of which the refractive index is known, it is done by increasing the focal distance of the petrographic microscope and observing which direction the light appears to move toward. This movement will always go into the materials of a higher refractive index. Changing calibrated liquids of various refractive indices and observing the movement determines a range of refractive indices of dipped crystal. The refractive indices were taken by measuring samples illuminated by the sodium line (598.3 mm). The refractive indices for solvents and studied crystals are listed in table 2.2.

Solvent	Methanol	THF	DMSO		Chloroform
Refractive index	1.33	1.47	1.48		1.44
Crystal	$Cs[Er(hfa)_4]$	$Er(hfa)_3(H_2O)_2$	$Er(acac)_3(H_2O)_2(H_2O)(CH_3CH_2OH)$	$Er(tpip)_3$	$Er(ftpip)_3$
Refractive index	1.50	1.55	1.55	1.64	1.65

Table 2.2. Refractive indices of methanol, THF, DMSO and chloroform. Averaged refractive indices of $Cs[Er(hfa)_4]$, $Er(hfa)_3(H_2O)_2$, $Er(acac)_3(H_2O)_2(H_2O)(CH_3CH_2OH)$, $Er(tpip)_3$ and $Er(ftpip)_3$ crystals as determined by the Becke line test using the D line.

The refractive index of $Zn(F\text{-}BTZ)_2$ was measured in film format using ellipsometry. The 180 nm-thick film of pure $Zn(F\text{-}BTZ)_2$ was thermally deposited, under the vacuum of 10^{-6} mbar, on a 128 nm thermal-grown SiO_2 layer grown on a flat silicon substrate. The thickness was monitored by a thickness-sensor in the vacuum-film-deposition evaporator and calibrated by the stylus profilometer Dektak 3. The stylus profilometer is used to measure the thickness of thin film and the roughness of surface. The thickness of thermal-grown-SiO_2 silicon substrate was measured and obtained using the UVISEL ellipsometer with internal modelling.

In order to characterise optical constants, the measured data are used to describe a fitting model. The model uses a mathematical dispersion formula that evaluates the thickness and optical properties of the material by adjusting specific fitting parameters. The refractive indices of the multi-layer film (180 nm $Zn(F\text{-}BTZ)_2$-128 nm SiO_2-silicon) were fitted

using the Hartmann dispersion formula, n (λ) = A + C / (λ – B), in the DeltaPsi2 software. The Hartmann dispersion formula works for transparent films to derive the refractive index. A (> 1) is a dimensionless parameter and B and C have the dimension of nm. All three parameters have no specific physical meaning.

When measuring the multi-layer film, a wavelength range longer than 450 nm wavelengths was chosen in order to avoid intense absorption of $Zn(F\text{-}BTZ)_2$. The important refractive index for $Zn(F\text{-}BTZ)_2$ is at ~ 1.5 μm wavelength, as we hope to design an optical waveguide working at 1.5 μm wavelength. The fitted thickness using the Hartmann dispersion formula is 172.19 ± 5.03 (nm). Parameters A = 1.696 ± 0.038, B = 301.653 ± 0.007 (nm) and C = 20.915 ± 0.544 (nm) were obtained as well. The fitted refractive index of thin $Zn(F\text{-}BTZ)_2$ film is 1.66 ± 0.05 at 1.54 μm with the error of ~ 6%.

2.3. Methodology

2.3.1. Microscopic absorption measurement for crystals

(1). Absorption and light scattering

In absorption, it is convenient to consider the incident light as an electromagnetic (EM) wave in order to present the interaction between light and matter. The electric and magnetic components in an EM field are perpendicular to each other and to the propagation direction, as well as

oscillating in space and time. The electrons around the atom nucleus are sensitive to the variation of the EM field. For the UV-visible-near IR optical band, the wavelength is much larger than the spatial extension of an atom, ion or small molecule and, therefore, the spatial variation of the fields over the atom, ion or small molecule under the fields can be neglected. When atoms, ions and molecules are illuminated in an EM wave, the electrons circulate around the nucleus and will accept energy by oscillating in space and time. The kinetic and potential energy of the quantum system will be enhanced. The enhanced energy will be relaxed through radiative relaxation (radiation) and non-radiative relaxation.

If the frequency of the light is close to the intrinsic frequencies of the atomic, ionic or molecular system, the interaction is termed resonant. In this case, there is a maximum energy transfer from the EM wave to the system, and the electrons are excited to reach a maximum absorption.

(2). *Absorption-relating physics parameters*

Transmittance is the fraction of incident light at a specified wavelength that passes through a sample. If we define the intensity of incident light as I_0 and transmitted light as I, the transmittance $T = I / I_0$. Absorbance is a quantity related to transmittance by a common logarithmic expression. The absorbance $A = -\mathrm{Log}_{10}(T)$.

The absorption coefficient, α, is a quantity that characterises how easily

the incident light can penetrate into a material or medium. According to Beer-Lambert Law, $T = e^{-\alpha d}$ so α can be obtained from a natural logarithmic expression $\alpha = -\mathrm{Ln}(T) / d$, where d is the optical path through a material or medium. The penetration depth is determined as α^{-1}, at which point the intensity of light decays to 36%. The skin depth is determined as $(2\alpha)^{-1}$, at which point the intensity of light decays to 13%.

The absorption cross-section, σ, characterises the probability of a certain particle-photon interaction. The absorption cross-section $\sigma = \alpha/N$, where N is the concentration of a material or a medium and the unit is cm^{-3}.

(3). *Light scattering*

When the frequency of light mismatches the intrinsic frequency, the interaction is non-resonant. In this case, the dipole moment is induced so the excess energy received by atoms, ions or molecules is quite small and the radiative relaxation is quite efficient. The direction of radiative relaxation does not need to be the same as the incident direction of the light. This non-resonant interaction is called light scattering. The scattering process is dominant in many real systems.

Rayleigh scattering is one of common light scattering in nature, and is the elastic scattering of light by particles, such as individual atoms or molecules much smaller than the wavelength of the light. It could occur when light travels through transparent solids and liquids. If we define one

small particle as a sphere of diameter d, the wavelength of un-polarised light is λ and the refractive index is n, the Rayleigh scattering cross-section is $\sigma_s = (2\pi^5 / 3)(d^6 / \lambda^4)[(n^2 - 1) / (n^2 + 1)]^2$. So, the Rayleigh scattering is stronger with increasing the sizes of particles and shortening the wavelength of incident light.

Strong light scattering will cause a background in the spectroscopic spectra, which will impact on the absolute shape of spectra, for instance, the dispersed distribution of the host medium can cause stronger light scattering. Therefore, a homogenously distributed sample is necessary to obtain an absorption spectrum.

(2). Absorption measurement: solution format and solid format

(2)-1. *Measuring optical path*

As for absorption measurement of solutions, the optical bands are only in the range of the UV-visible band, and the UV-cuvette (Newport Optics) is used to contain solutions. The optical path is 1 cm, as wide as the cuvette.

As for absorption measurement for crystals, the crystal samples are flatly deposited on quartz substrates vertical to the direction of incident light ray, so that the optical path is the thickness of the crystal. The thicknesses of crystal samples were measured by a graduated microscope equipped with a microposition stage (accuracy = 5 μm).

(2)-2. *Concentration of Er^{3+} ions in samples*

The concentrations of Er^{3+} ions in solution samples were estimated by the mass densities (mg/cm^3) of dissolved erbium complexes in solutions. The amounts of powder were weighed on the electric scale with an accuracy of 2 micrograms, and the volumes of solvents were measured with a measuring cylinder with the accuracy of 0.2 ml. The concentrations of Er^{3+} ions in crystals are referred to reported mass densities from x-ray crystallographic data in table 2.1.

(3)-3. *Absorption measurement in solution and crystal samples*

UV-visible absorption spectra of solutions in quartz cuvettes (Newport Optics) were taken by a Hitachi U-3000 spectrometer. The spectra were extracted in steps of 2 nm.

UV-visible-IR absorption spectra of crystal samples were measured using the home-made single-beam micro-absorption setup. The crystal samples were deposited on a quartz substrate using static electric force. Absorption spectra of the UV-visible region were taken using the Arc lamp and Hamamatsu 9113B PMT, and the IR absorption spectra were taken by using a tungsten lamp and the Hamamatsu R5509-72 nitrogen cooled PMT detector. The John Yvon Traix 550 spectrometer equipped with 1200 and 600 lines/nm gratings was employed for UV-visible and IR bands, respectively. The slit width for all measurements on crystals was 2 mm.

Signals were recorded by the 7265 DSP Perkin Elmer lock-in amplifier and extracted on a PC in steps of 2 nm.

2.2.2. Mixture of $Er(f\text{-}tpip)_3$ and $Zn(F\text{-}BTZ)_3$

(1). Cleaning procedure

The substrate was cleaned before loading it into the vacuum chamber. The cleaning procedure aimed to remove any dust, liquid impurities or organic impurities. The substrate was washed using detergent and distilled water. Then, the substrate was placed in an ultrasonic bath combining detergent dissolved in distilled water for 20 minutes. After that, the substrate took an ultrasonic bath in distilled water for 5 minutes. This procedure was repeated three times. Then, the substrate was placed in an ultrasonic bath in ultra-gradient acetone solvent (Sigma-Aldrich) for 5 minutes, repeating this twice. Finally, the substrate was placed in an ultrasonic bath in ultra-gradient chloroform solvent (Sigma-Aldrich) for 5 minutes, again repeating this twice. The substrate was dried using a pure nitrogen gas gun before loading it into the vacuum chamber.

(2). Co-evaporation

The vacuum film deposition evaporator was controlled to have a vacuum background lower than 5 (10^{-6}) mbar to deposit organic molecules on a substrate (glass or silicon) as a uniform thin film at room temperature.

Two organic sources were located diagonal to each other and separated thickness-sensors recorded the depositing rate for each source. The depositing rate of molecules was controlled to be < 5 Å/s, which is around the dimension of a single molecule.

(3). Ratios of two molecules and calibration

The ratios of two molecules were estimated by the densities of $Er(ftpip)_3$ and $Zn(F\text{-}BTZ)_2$ derived from x-ray diffraction data. The atomic ratio of two molecules in a co-doped system was calibrated by a grown co-doped film with 78 nm $Zn(F\text{-}BTZ)_2$ and 240 nm $Er(ftpip)_3$. The calibration of molecule ratio in co-doped film was confirmed using energy dispersive x-ray analysis (EDX) on a FEI Quanta 3D ESEM, a research facility for EDX measurement. Energy dispersive x-ray analysis is an analytical technique used for elemental analysis of the x-ray spectroscopic characteristics of a sample. The measurements for this co-doped film were taken at 7 different spaces over the whole film, with a spatial resolution of 20 × 20 μm. Each measurement was integrated and averaged 4 times. The analysed atomic ratio between erbium element and zinc element was 1.18 ± 0.15 in the co-doped film containing mixed 240 nm $Er(ftpip)_3$ and 78 nm $Zn(F\text{-}BTZ)_2$. So, the atomic ratio between $Er(ftpip)_3$ and $Zn(F\text{-}BTZ)_2$ is ~ 1, which means there was 50% $Er(ftpip)_3$ molecules doped in the co-doped film, whilst the growth rate ratio of $Er(ftpip)_3$ and $Zn(F\text{-}BTZ)_2$ is 3 : 1. In

this thesis, each ratio reported is the atomic ratio of $Er(ftpip)_3$ in the co-doped system.

2.2.3. Time-resolved photoluminescence

(1). Measuring time-resolved photoluminescence

The setup for measuring time-resolved photoluminescence using the Nd:YAG-OPO laser is shown in figure 2.4. The polariser is used to remove the polarised "Idler" beam, and the intensity of the "Signal" pulse is measured using a multifunction optical meter. The laser beam is collimated and reflected onto the sample after a 385 nm absorbing filter is positioned for removing leaked 355 nm light. The sample is positioned on a home-made sample stage. The luminescence from the sample is collimated into the entrance slit of the Triax 550 spectrometer. The probed photoelectric signals are magnified by specific PMT detectors. The time-resolved spectra of output signals are displayed on an oscilloscope and the spectra data are collected by PC.

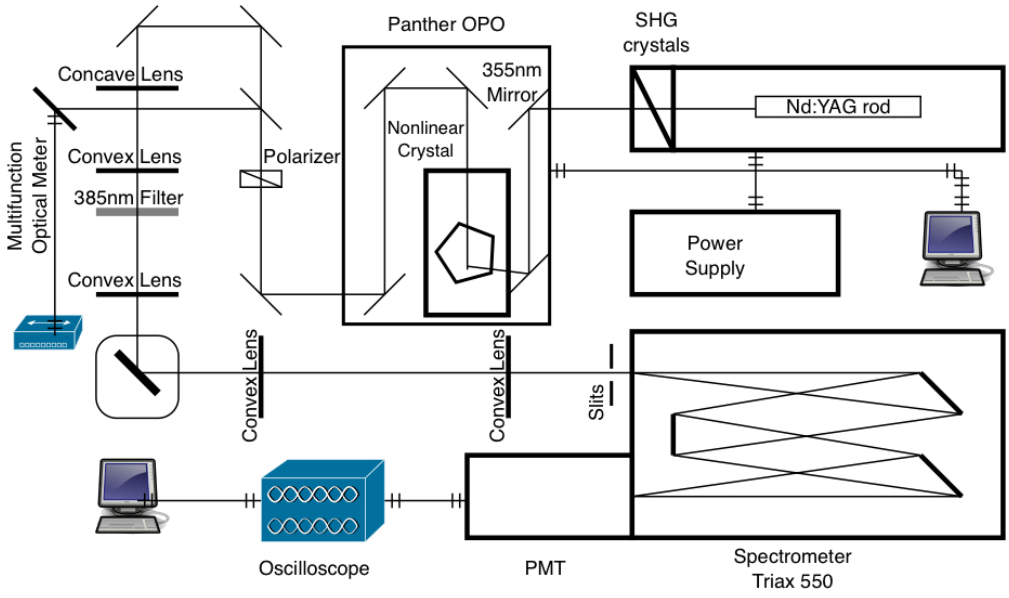

Figure 2.4. Photoluminescence measurement using the Nd:YAG-OPO laser system

(2). Analytical solution to the rate equation of the three-level system

The time-resolved photoluminescence spectroscopy is a tool to measure the decay lifetime and rise-time of luminescence because there is a rate-constant dependence for the time-response of observed luminescence. The spontaneous emission can be simply described as a two-level system where there is an excited state and a ground state. The time-differential population for spontaneous emission is expressed by $dN / dt = - \mathrm{R}\, N$, where N is the population in excited state and R is the total rate of the transition between the two states.

The investigation of the sensitisation process through an analytical solution to the rate equation is very complicated for modelling statistic and time-resolved rate equations, since there are up to more than 20 rate constants to consider.[5] As mentioned before, the non-radiative relaxation is

known to be fast during the vibrational splitting of one excited molecule state, and the fluorescence occurs from the lowest excited state to the ground state. As for Er^{3+} ions, each spectral transition is nearly monochromic since each energy state is narrow, so that the non-radiative relaxation is extremely fast in each state. Therefore, it is reasonable to describe a spectral transition between two ${}^{S+1}L_J$ levels of an Er^{3+} ion using a two-level system.

In an EDFA, the ${}^4I_{11/2}$ level of Er^{3+} ions are excited for populating ${}^4I_{13/2}$ level to provide the 1.5 μm emission of the ${}^4I_{13/2} \rightarrow {}^4I_{15/2}$ transition. Generally, the Er^{3+} ions are excited onto higher excited states, such as the ${}^2H_{11/2}$ level using 520 nm wavelength, and the population could non-radiatively decay to the ${}^4I_{13/2}$ level. These transition processes can be described as three-level system. Here we take the ${}^4I_{13/2}$ level as the middle excited state and define a hypothetical upper excited level above the ${}^4I_{13/2}$ level, which is not a specific real excited level of an Er^{3+} ion, since there is a complicated distribution of excited states above the ${}^4I_{13/2}$ level. And, if the interaction of excited states between molecules (splitting and the different isolated molecule) is not considered, a simplified three-level system could be used to model the dynamic transition process, as seen in figure 2.5.

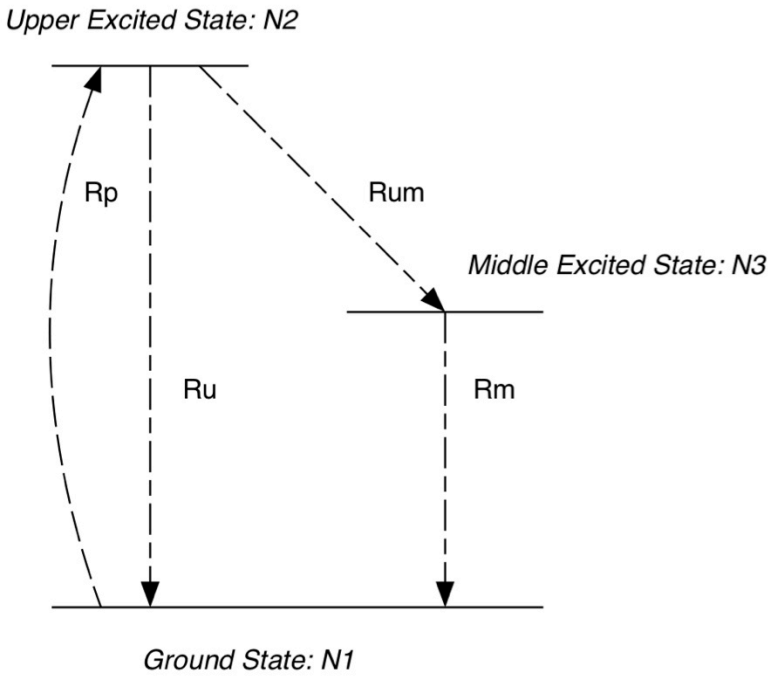

Figure 2.5. The simplified three-level system for spectral transition

In the three-level system, we define the population at the ground state, the upper excited state and the middle excited state as $N1$, $N2$ and $N3$, respectively. The rate of each transition between any two states is defined respectively: the pump rate for populating the upper excited state from the ground state is R_P, the decay rate for depopulating the upper excited state to the ground state is R_u, the transfer rate for the transferring process from the upper excited state to the middle excited state is R_{um}, and the decay rate for the decaying process from the middle excited state to the ground state is R_m. The back transfer from the middle excited state to the upper excited state is ignored because the energy gap between them is wider than the vibrational splitting of each level.

(3). Short pulse-laser source

The optical source absolutely decides the time-resolved solutions of the rate equations. The short laser-pulse just maintains the pump rate for a very short time (~ ns), but the decay rate would remain much longer since the decay lifetime could be long due to some weakly allowed transitions like lanthanide ions. If the pulse lasts for a much shorter time than any time for the decay rate, and the total population of molecules $N_{tot} = N1 + N2 + N3$, the rate-equation can be counted for after the pulse, so that the rate-equation for the excitation by 5 ns pulse laser is:

$$\frac{dN3(t)}{dt} = \mathrm{R}_{um} N_{tot} - R_m N3(t)$$
$$\frac{dN2(t)}{dt} = -(\mathrm{R}_u + \mathrm{R}_{um}) N_{tot}$$
$$\frac{dN1(t)}{dt} = (\mathrm{R}_u + \mathrm{R}_{um}) N_{tot} + \mathrm{R}_m N3(t)$$

With initial conditions $N2(0) = 0$, $N3(0) = 0$ and $N1(0) = N_{tot}$, the time-resolved solution of the population at the middle excited state is solved:

$$N3(t) = \frac{\mathrm{R}_{um} N_{tot}}{\mathrm{R}_{um} + \mathrm{R}_u - \mathrm{R}_m} e^{-\mathrm{R}_m t} \left[1 - e^{-(\mathrm{R}_{um} + \mathrm{R}_u - \mathrm{R}_m) t} \right] \qquad (2\text{-}5)$$

As for the situation that the Nd:YAG-OPO pulse laser excites the Er^{3+} ions in co-doped films both through direct excitation and sensitisation, the pulse just lasts 5 ns, shorter than the lifetime of the Er^{3+} ion at 1.5 μm emission, i.e > 250 μs for $Er(ftpip)_3$, so the rate R_m will be the decay rate for ~ 1.5

μm emission. The equation (2-5) indicates that the rise-rate for 1.5 μm emission excited at short pulse laser is associated with the decay rate of the upper excited state, the transfer rate to the middle excited level and the decay rate for 1.5 μm emission. Moreover, this expression could also describe the sensitisation because, in such a short pump time, the energy transfer is mainly from the singlet states in an organic sensitiser to the Er^{3+} ions and a fast non-radiative process.

(4). Long pulse-laser source

When the existing source is a long pulse-laser longer, than the luminescence lifetime, and the power of the laser is much lower than the Nd:YAG pulse laser, for instance, a semiconductor diode laser with the power lower than 1 W, the pump rate would be continuous and longer than the luminescence lifetime. The long pulse-laser excitation complicates the expression of rise-rate, and the rate equation needs to be modified to:

$$\frac{dN3(t)}{dt} = \mathrm{R}_{\mathrm{um}} N2(t) - R_{\mathrm{m}} N3(t)$$
$$\frac{dN2(t)}{dt} = \mathrm{R}_{\mathrm{p}} N1(t) - (\mathrm{R}_{\mathrm{u}} + \mathrm{R}_{\mathrm{um}}) N2(t)$$
$$\frac{dN1(t)}{dt} = -\mathrm{R}_{\mathrm{p}} N1(t) + \mathrm{R}_{\mathrm{u}} N2(t) + \mathrm{R}_{\mathrm{m}} N3(t)$$
$$N_{\mathrm{tot}} = N1(t) + N2(t) + N3(t)$$

The initial populations at these states were $N1(0) = N\mathrm{t}$ and $N2(0) = N3(0) = 0$. The analytical solution for the time-resolved population at the middle state is:

$$N3(t) = b/a + de^{-\frac{1}{2}(R_p+R_u+R_{um}+R_m-c)t} - (b/a+d)e^{-\frac{1}{2}(R_p+R_u+R_{um}+R_m+c)t} \qquad (2\text{-}6)$$

The *a*, *b*, *c* and *d* are rate constant-associated parameters:

$$a = R_p R_{um} + R_m(R_u + R_{um} + R_p)$$
$$b = R_p R_m N t$$
$$c = \sqrt{(R_u + R_{um} + R_p - R_m)^2 - 4R_p R_{um}}$$
$$d = -\frac{b(R_p + R_u + R_{um} + R_m + c)}{2ac}$$

At the excitation of the long-pulse laser, the time of the pulse should be long enough to equilibrate the population at the middle excited state, so that experimental observation for the intensity of luminescence is equilibrium. In this model, the R_m can be considered as the decay rate for 1.5 μm emission, if the middle excited state is the long-lived excited state for 1.5 μm emission.

There are some conditions that $d > 0$ and $-(b/a + d) > 0$ so that the expression has a combination of the decay component, $e^{-\frac{1}{2}(R_p+R_u+R_{um}+R_m+c)t}$, and the rise component, $-e^{-\frac{1}{2}(R_p+R_u+R_{um}+R_m-c)t}$. So, the rise-rate is $R_P + R_u + R_{um} + R_m - c$, which is much smaller that the decay rate $R_P + R_u + R_{um} + R_m + c$. Therefore, in Er^{3+} ions, this suggests that the rise-time for 1.5 μm emission would be shorter than the decay lifetime for 1.5 μm emission, since the pump-rate R_P would be larger than the decay-rate R_m. It is noteworthy that we consider the R_P to be a static rate constant while populating the states for 1.5 μm emission. This case would occur for the

energy transfer from the singlet states since the population of singlet states rapidly equilibrate with time. However, if we consider the energy transfer from the triplet states, the rate constant R_P needs to be a dynamic factor that will increase against time, because the population of triplet states needs longer to equilibrate, so that it is more challenging to get analytical solutions.

(5). Exponential fitting and multi-exponential fitting

In accordance to the time-resolved solution for rate equations, the same result occurs for the equilibration of the long-pulse pump and short-pulse pump: the process for the spectral transition between the middle excited state (like the $^4I_{13/2}$ level) to ground state obeys a single exponential decay process by $e^{-R_m t}$, which is the spontaneous emission.

In the equation (1-6), the decay-rate $R_{1.5\mu m}$ for an Er^{3+} ion is the sum of the radiative and non-radiative rate, and the distant quenching groups like hydrated impurities changes the non-radiative rate so that the observed $R_{1.5\mu m}$ is varied. If we hypothesise the rate $R_{1.5\mu m}(i)$ for an individual group (i) of Er^{3+} ions sitting in a specific quenching environment, the total observed rate would be $\sum_i R_{1.5\mu m}(i)$ for the whole groups of Er^{3+} ions in the bulk. Thus, it is reasonable to distinguish the series of decay rates by one fast-decay rate $fR_{1.5\mu m}$ and one long-decay rate $sR_{1.5\mu m}$, so the intensity of emission can be expressed as $I(t) = I_1(t)e^{-fR_{1.5mm}} + I_2(t)e^{-sR_{1.5mm}}$. Therefore, a

single-exponential decay process and a double-exponential decay process are considered for fitting the time-resolved photoluminescence spectra. If we take the relationship $\tau = R^{-1}$, the fitting equation would be:

Single exponential fitting equation: $I = I_0 + I_1 e^{-t/\tau}$;

Double exponential fitting equation: $I = I_0 + I_1 e^{-t/\tau_1} + I_2 e^{-t/\tau_2}$ (2-7)

The double exponential fitting equation usually produces a short lifetime and a long lifetime. In a double exponential fitting equation, the intensity is decaying with a combination of two exponential decay curves. The integration for I over infinite time is

$$\int_0^\infty (I - I_0)\,dt = \int_0^\infty I_1 e^{-t/\tau_1}\,dt + \int_0^\infty I_2 e^{-t/\tau_2}\,dt = I_1\tau_1 + I_2\tau_2$$

This equation means integrated intensity of the time-resolved luminescence contains two part integrated components of $I_1\tau_1$ and $I_2\tau_2$ for the lifetime scale. Therefore, the percentages of the components of lifetimes can be obtained by $I_1\tau_1 / (I_1\tau_1 + I_2\tau_2)$ and $I_2\tau_2 / (I_1\tau_1 + I_2\tau_2)$. So, the average lifetime can be understood as

$$<\tau> = \left[I_1\tau_1 / (I_1\tau_1 + I_2\tau_2)\right]\tau_1 + \left[I_2\tau_2 / (I_1\tau_1 + I_2\tau_2)\right]\tau_2 \qquad (2\text{-}8)$$

2.3.4. Emission spectra and excitation spectra

(1). Photoluminescence spectra

The photoluminescence of films or powder can be produced by using a frequency-modulated continue-wave diode laser or the Nd:YAG-OPO laser. The optic-setup for measuring photoluminesnce spectra has been

introduced in the section 2.2.3. The modulation of diode lasers can use the Model 190 Optical Chopper or rely on the internal integrated TTL modulation model connected to TTL/COMS output in the function generator. The luminescence from samples was aligned into the Triax 550 spectrometer, the intensities were probed by PMT detectors, and the signals were analysed by the lock-in amplifier (model 5029 or model 7265) or an oscilloscope. The spectra were extracted by using Spectroscopy Software from the supplier on a PC. An appropriate slit width is necessary when considering probing low-noise intensity of the signal and the bandpass of spectra. The UV-visible spectrum was detected by the Hamamatsu 9113B PMT, and the IR spectrum was detected by the Hamamatsu R5509-72 nitrogen-cooled PMT detector. In order to avoid the light scattering produced by exciting lasers and avoid the higher orders, the reflected laser beams have to avoid being incident to the entrance slit and some absorbing filters have to put in front of the entrance slit to remove the scattered lasers and specific short wavelengths. The corrections for the photoluminescence spectra were done using the internal correction spectra of the gratings and types of detectors in the software.

(2). Excitation spectra

An excitation spectrum is the identification for various intensities of a monochromatic emission at varied continuous exciting wavelengths. For

example, for the 1.5 μm emission of Er^{3+} ions, the $^4I_{13/2}$ level can be populated from any higher $^{S+1}L_J$ level, such as, through the $^2H_{11/2} \rightarrow {}^4I_{13/2}$ and $^4I_{11/2} \rightarrow {}^4I_{13/2}$ transitions, and each intensity of the transitions is proportional to the intensity of the 1.5 μm emission at the corresponding exciting wavelength. So, the continuous excitation wavelengths for the 1.5 μm emission produce the excitation spectrum. In the measurement, the Triax 550 spectrometer was equipped with 600 lines/mm gratings, and the Hamamatsu R5509-72 nitrogen-cooled PMT probed the 1.5 μm emission.

The excitation spectra can be obtained using the optical-setups in section 2.2.3 with the continuous Nd:YAG-OPO lasers or with the continuous monochromatic lights dispersed from the modulated lamp sources. The John Yvon Triax 180 monochromator was used for dispersing monochromatic lights in the range of 350 nm to 700 nm wavelength, with both the entrance and exit slit width set maximally to 2 mm in order to obtain the maximum intensity of light beams. The Newport Apex Arc Lamp source with a xenon lamp of 50 W output was aligned and focused into the entrance of the monochromator. The dispersed output light was focused and reflected onto the sample with a diameter of ~ 4 mm.

The correction for the intensity spectrum of the monochromatic light beam has to be done for the extracted spectrum of the 1.5 μm emission. The intensity spectrum of the monochromatic lights, incident on the sample, was measured using the Newport 818-UV enhanced silicon detector, and

the intensity spectrum was extracted by the lock-in amplifier with subtracting the responsivity to wavelengths of the detector from the supplier (Continuum Surelite Laser). In an excitation measurement using continuous Nd:YAG-OPO lasers, the excitation was done using the pulse energy of each exciting wavelength to correct the measured data. Some absorbing filters have to put in front of the entrance slit of the Triax 550 spectrometer in order to remove the short wavelengths for avoiding the higher order.

2.2.5. Waveguide fabrication and gain measurement

(1). Planar waveguide fabrication and measurement

The planar waveguide was fabricated by using the vacuum film deposition evaporator. A 2 μm thickness film was deposited on top of a flat 720 nm SiO_2 film on a silicon substrate. The co-doped film is doped with 30% $Er(ftpip)_3$ and 70% $Zn(F\text{-}BTZ)_2$. The size of the surface of the planar waveguide was 8×10 mm^2.

The gain measurement was undertaken using a probe and pump method. A probing laser beam was shone at one edge of the planar waveguide with a modulation of f_1 Hz. The frequency of the probing laser beam was modulated using optical chopper 1, which was a Model 197 Dual Aperture Light Chopper. The pumping laser beam was focused by a f = 150 mm cylindrical lens to be a stripe line cross over the waveguide with a

modulation of f_2 Hz. The frequency of the pumping laser beam was modulated using optical chopper 2, which was another Model 197 Dual Aperture Light Chopper. These two optical choppers were synchronised so that $f_1 = 10\ f_2$. The photoluminescence from the other edge of the waveguide was aligned and focused into the entrance slit of the Triax 550 spectrometer. The time-resolved photoluminescence output from the waveguide was extracted on an oscilloscope triggered by f_2. The schematic diagram of the probe and pump method is displayed in figure 2.6.

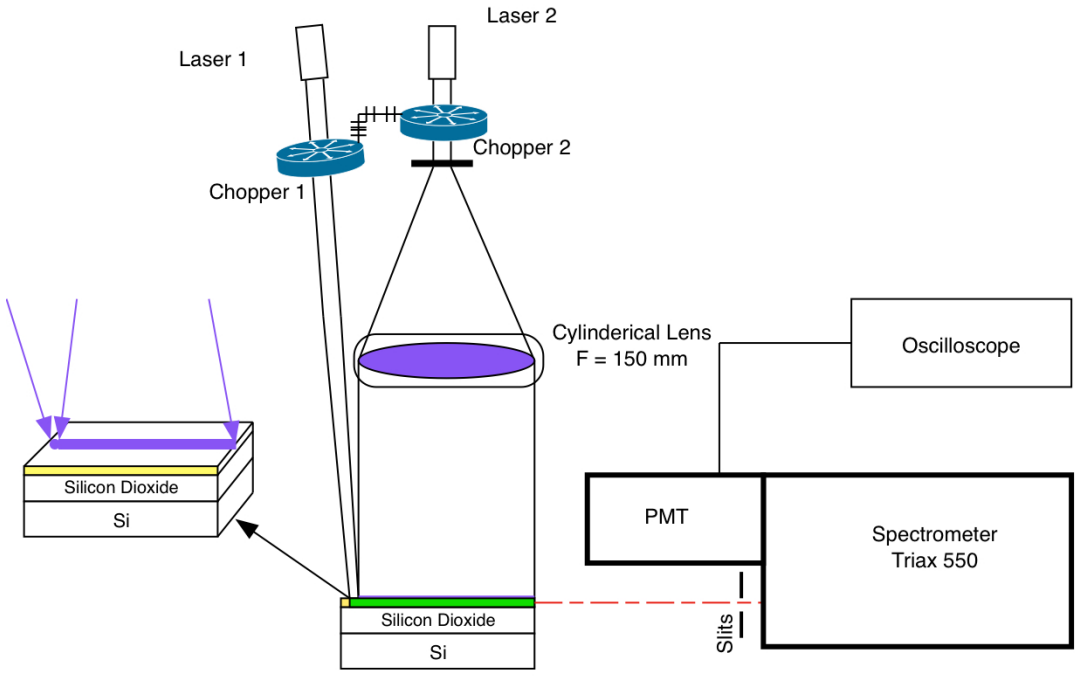

Figure 2.6. Schematic diagram of the probing and pumping method used for measuring optical gain

(2). Optical simulation in planar waveguide

The fabricated co-doped waveguide can be modelled as a

low-absorbing dielectric slab waveguide. The cladding layer (layer 3) is air with a refractive index of n_3, the core layer (layer 1) of the b thickness is co-doped organics with a refractive index of n_1, and the substrate (layer 2) is a SiO_2 layer with a refractive index of n_2. The optical propagation behaviour in the slab waveguide can be investigated using the optical ray approach. A schematic of the slab waveguide is displayed in figure 2.7.

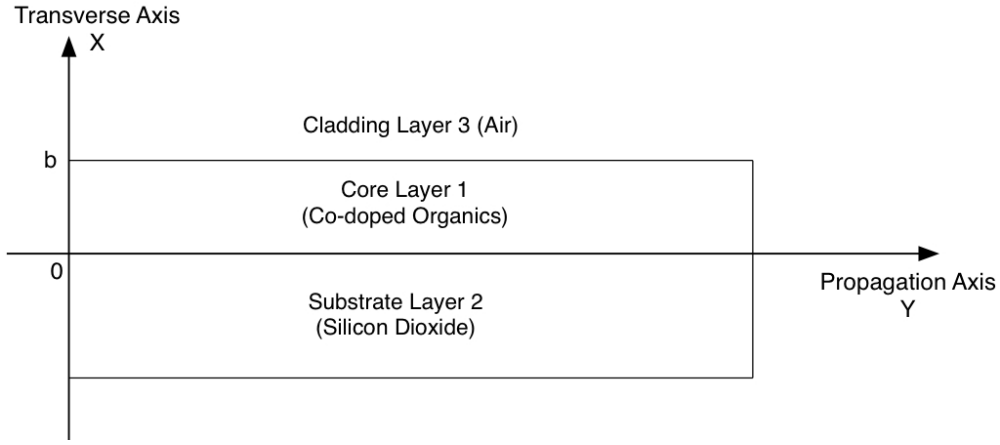

Figure 2.7. Schematic of the co-doped slab waveguide

A three-layer asymmetrical slab dielectric waveguide structure consists of an upper interface of 13 between the cladding layer and core, and a lower interface of 12 between the core and substrate layer. The reflective angle at interface 12 is θ_1, the refractive angle at interface 12 is θ_2 and the refractive angle at interface 13 is θ_3. The relationship among them is $n_1 \sin\theta_1 = n_2 \sin\theta_2 = n_3 \sin\theta_3$. In the case that $n_1 > n_2 > n_3$, the situation of total internal reflection in both interfaces will cause the phase shift $-2\Phi_{12}$ and $-2\Phi_{13}$, where $2\Phi_{12} = 2\arctan[(n_1^2\sin^2\theta_1 - n_2^2) / (n_1 \cos\theta_1)]^{1/2}$ and, for

interface 13, $2\Phi_{13} = 2\arctan[(n_1^2 \sin^2\theta_1 - n_3^2) / (n_3 \cos\theta_1)]^{1/2}$.

Here, we define that T_2 and T_3 are $T_2 = \gamma_2 / \gamma_1$ and $T_3 = \gamma_3 / \gamma_1$, and expressions of parameters are $\gamma_1 = k_0 (n_1^2 - n_{eff}^2)^{1/2}$, $\gamma_2 = k_0 (n_{eff}^2 - n_2^2)^{1/2}$, $\gamma_3 = k_0 (n_{eff}^2 - n_3^2)^{1/2}$ and the effective index n_{eff}. The simplification gives that $- 2\Phi_{12} = - 2\arctan T_2$ and $- 2\Phi_{13} = - 2\arctan T_3$. The eigenvalue function or dispersion relation is used to define the distribution constant of propagation modes in the waveguide. The total phase shift, which happens both in the interface 12 and the interface 13, satisfies $2\gamma_1 b - 2\Phi_{12} - 2\Phi_{13} = 2m\pi$ (m is an integer including zero), so the eigenvalue function is obtained: $\gamma_1 b = m\pi + \arctan T_2 + \arctan T_3$. Here, T_2 and T_3 are modified to separate expressions for TE and TM: $T_2 = (n_1^2 / n_2^2)^s (\gamma_2 / \gamma_1)$, and $T_2 = (n_1^2 / n_3^2)^s (\gamma_3 / \gamma_1)$ with conditions of $s = 0$ for TE mode and $s = 1$ for TM, respectively.

In general, the normalised parameters P, V and Q are employed to generalise the eigenvalue function. P is the normalised propagation constant, V is the normalized core thickness, and Q is the asymmetrical factor:

$P = (\beta^2 - k_0^2 n_2^2) / [k_0^2 (n_1^2 - n_2^2)]$, $V = k_0 (n_1^2 - n_2^2)^{1/2} b$

$Q = (n_1^2 - n_3^2) / (n_1^2 - n_2^2)$

The normalised eigenvalue function is:

$(1 - P)^{1/2} V = m\pi + \arctan[P / (1 - P)]^{1/2} + \arctan[(P + Q) / (1 - P)]^{1/2}$

β is the propagation constant along the waveguide. The penetration depth in the cladding layer and SiO_2 substrate layer is defined as $\Delta x = \Delta z / \tan\theta_1$,

where Δz is the displacement at the interface due to the phase shift. Thus, Δz is expressed by $\Delta z = d\Phi / d\beta$. By employing the relative expression above, the penetration depth of cladding layer 3 and substrate layer 2, and the effective thickness of the guide core can be obtained in the view of TE and TM modes, respectively:

For TE mode:

$\Delta x_{2TE} = \gamma_2^{-1}$, $\Delta x_{3TE} = \gamma_3^{-1}$, $b_{effTE} = b + \Delta x_{2TE} + \Delta x_{3TE}$;

For TM mode:

$\Delta x_{2TM} = [n_1^2 n_2^2 (\gamma_1^2 + \gamma_2^2)] / [\gamma_2 (n_2^4 \gamma_1^2 + n_1^4 \gamma_2^2)]$,

$\Delta x_{3TM} = [n_1^2 n_3^2 (\gamma_1^2 + \gamma_3^2)] / [\gamma_3 (n_3^4 \gamma_1^2 + n_1^4 \gamma_3^2)]$,

$b_{effTM} = b + \Delta x_{2TM} + \Delta x_{3TM}$; (2-9)

The distribution fields for TE and TM modes are expressed as:

$$\frac{E_y(x)}{H_y(x)} = \begin{cases} A\exp(\gamma_2 x) & (-\infty < x \le 0 : \text{substrate}) \\ A\left[\cos(\gamma_1 x) + T_2 \sin(\gamma_1 x)\right] & (0 \le x \le b : \text{core}) \\ A\left[\cos(\gamma_2 b) + T_2 \sin(\gamma_2 b)\right]\exp\left[-\gamma_3 (x-b)\right] & (b \le x \le +\infty : \text{cladding}) \end{cases}$$

(2-10)

The similar expressions are suitable for $E_y(x)$ of TE mode and $H_y(x)$ of TM mode. The energy flux density propagating along the waveguide can be obtained due to the Poynting rule:

For TE mode: $\vec{S} = \frac{\beta}{2\omega\mu_0} \left|E_y(x)\right|^2 \vec{z}$

For TM mode: $\vec{S} = \frac{\beta}{2\omega\varepsilon_0\varepsilon_1} \left|H_y(x)\right|^2 \vec{z}$ (2-11)

(3). Optical loss and population inversion

Optical loss in the co-doped fabricated waveguide is mainly due to attenuation loss in the propagation constant. The attenuation loss for the propagation constant is complicated: dominated by absorption and anisotropy of materials as well as roughness-caused light scattering. In this part, we just consider the absorption loss caused by Er^{3+} ions in the co-doped films.

Experimentally, the output luminescence at one edge of the waveguide was measured while probing laser shining on the other edge. The intensity of output luminescence was attenuated when the light passed through the waveguide. If we assume the initial intensity from the probing edge is I_{PI}, the intensity from the other edge is I_P and the amplified intensity by pump laser is I_P', the relative gain would be $G = 10Log_{10}(I_P' / I_P)$. The absorbance of Er^{3+} ions is $A = – Log_{10}(I_P / I_{PI})$, so the net gain $g = G – 10A$.

In terms of modelling, optical gain is dominated by stimulated emission, which requires population inversion. If we assume that any transitional process above the $^4I_{13/2}$ level is relatively immediate and fast, so that the complicated spectral transitions for erbium could be simplified to be time-resolved distribution of population between the $^4I_{13/2}$ level and the ground $^4I_{15/2}$ level. The time resolved population at the excited states of 1.5

μm emission can be expressed as:

$$\frac{dN(t)}{dt} = [\mathrm{R_P}(N_0 - N(t)) - \mathrm{R_{1.5\mu m}}]N(t) \qquad (2\text{-}12)$$

A solution is $N(t) = [N_{\mathrm{tot}}\mathrm{R_P} / (\mathrm{R_P} + \mathrm{R_{1.5\mu m}})][1 - e^{-(\mathrm{R_P}+\mathrm{R_{1.5\mu m}})t}]$ and N_{tot} is the total population. R_P is the pumping rate from the ground state to the $^4I_{13/2}$ level, and $R_{1.5\mu m}$ is the decay rate for the $^4I_{13/2}$ level. In this equation, we can define a rise-rate of $R_{rise} = R_P + R_{1.5\mu m}$ that is the reverse of the rise-time for the 1.5 μm emission. When the time is infinite, the excited population is $N_{tot}R_P / (R_P + R_{1.5\mu m})$. The population inversion occurs at the condition that $R_P / (R_P + R_{1.5\mu m}) \geq 0.5$, which means that more than 50% population is excited. The R_P is related to the pump power.

Chapter 3. Results and Discussion

3.1. Enhanced quantum yield by fluorination: correlation of optics and structure

3.1.1. Absorption spectra and Judd-Ofelt parameters

The solutions in the absorption measurement were filled in the quartz cuvettes (1 cm × 1 cm × 10 cm). The UV-visible absorption spectra were taken using the Hitachi U-3000 spectrometer in steps of 2 nm. Samples of $CsEr(hfa)_4$, $Er(hfa)_3(H_2O)_2$ and $Er(acac)_3(H_2O)_2$ were each dissolved in THF, methanol and DMSO for preparing solute samples. $Er(tpip)_3$ was only dissolved in the chloroform and $Er(ftpip)_3$ was dissolved in the DMSO due to the poor solubility of $Er(tpip)_3$ and $Er(ftpip)_3$ in both THF and methanol. The IR absorption spectra of these solutions were excluded because the IR absorption of aqueous solvents would overcome the intrinsic absorption of Er^{3+} ions so that the IR absorption of Er^{3+} ions cannot be seen. The absorption spectra between 360 nm and 680 nm wavelength are displayed in figure 3.1, where the absorption cross-sections were determined from the Er^{3+} concentration in each solution.

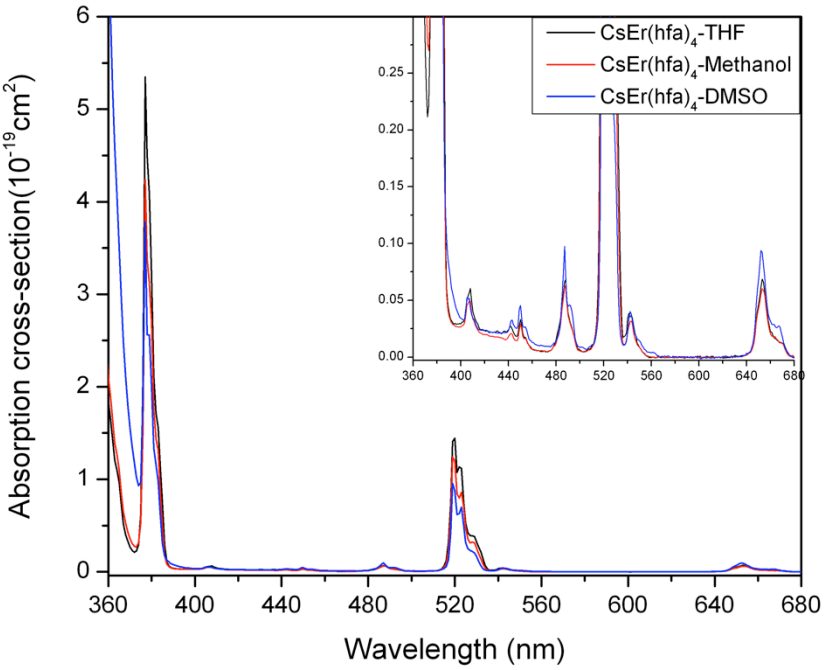

Figure 3.1.a. Absorption of $CsEr(hfa)_4$ in THF, methanol and DMSO.

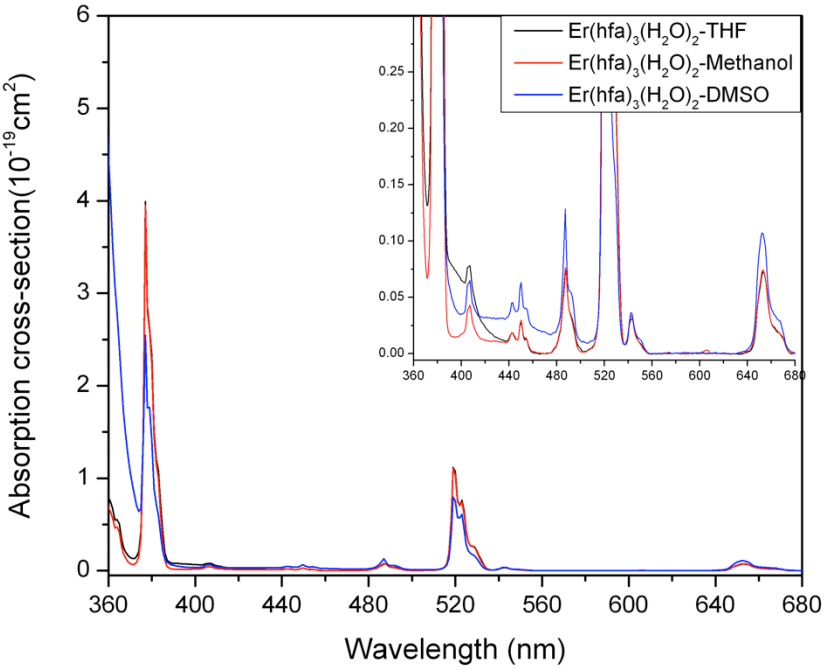

Figure 3.1.b. Absorption of $Er(hfa)_3(H_2O)_2$ in THF, methanol and DMSO.

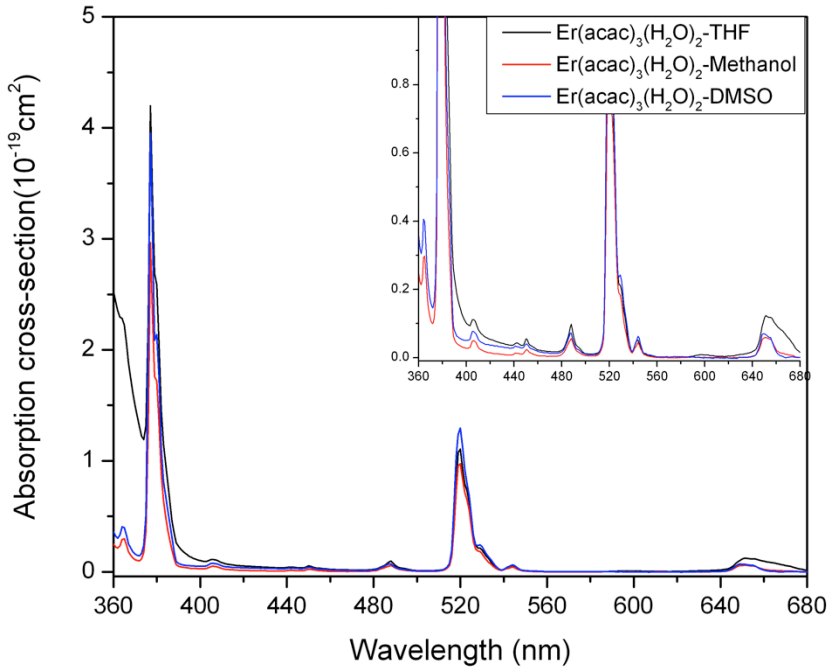

Figure 3.1.c. Absorption of $Er(acac)_3(H_2O)_2$ in THF, methanol and DMSO.

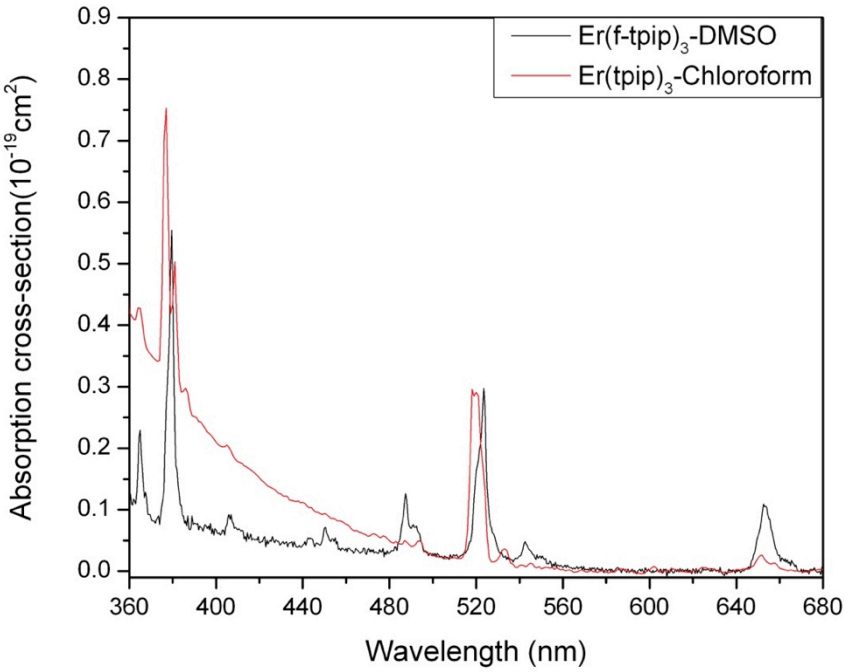

Figure 3.1.d. Absorption of $Er(ftpip)_3$ in DMSO and $Er(tpip)_3$ in chloroform.

The IR absorption of Er^{3+} ions can be measured in the crystals of these

complexes. The UV-visible-IR absorption of $CsEr(hfa)_4$, $Er(hfa)_3(H_2O)_2$, $[Er(acac)_3(H_2O)_2](H_2O)(CH_3CH_2OH)$, $Er(tpip)_3$ and $Er(ftpip)_3$ crystals were measured using a home-made single-beam micro-absorption setup. The spectra were extracted on a PC in steps of 2 nm. The absorption spectra from 360 nm to 680 nm, 900 nm to 1100 nm and 1400 nm to 1600 nm wavelengths are displayed in figure 3.2.

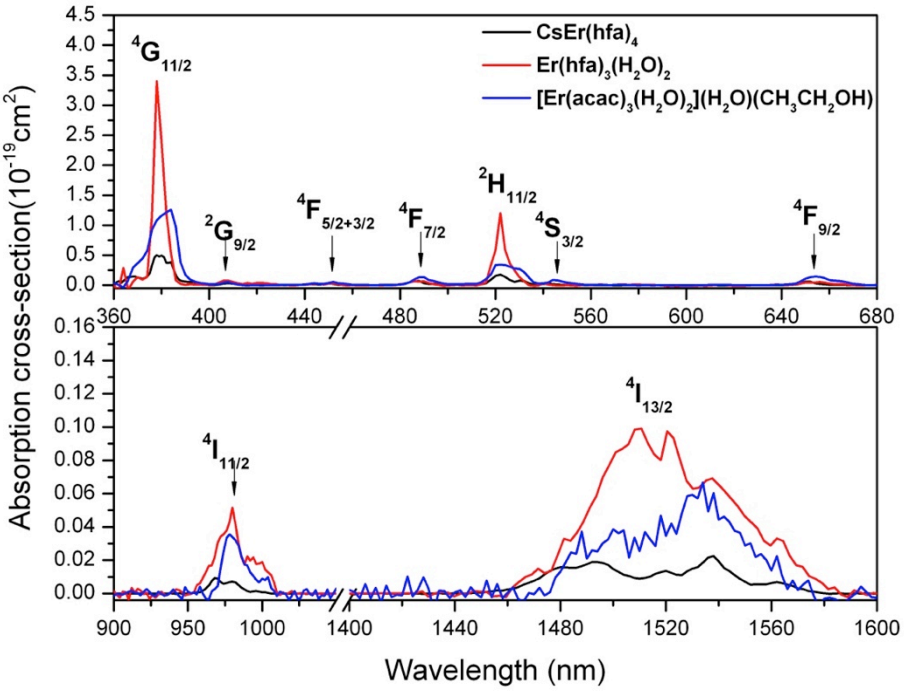

Figure 3.2.a. Absorption of $[Er(acac)_3(H_2O)_2](H_2O)(CH_3CH_2OH)$, $CsEr(hfa)_4$ and $Er(hfa)_3(H_2O)_2$ crystals

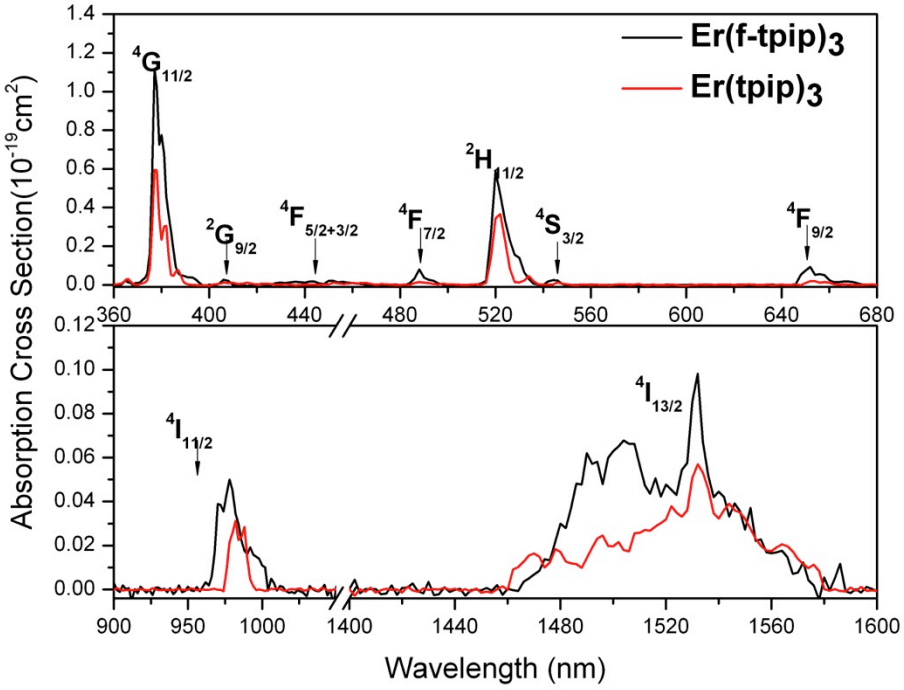

Figure 3.2.b. Absorption of $Er(ftpip)_3$ and $Er(tpip)_3$ crystals

Judd-Ofelt parameters for the complexes in solutions are listed in Table 3.1 together with the calculated radiative lifetimes at ~ 1.5 μm emission.

Material	Solvent	$\Omega_2\times10^{-20}$ (cm^2)	$\Omega_4\times10^{-20}$ (cm^2)	$\Omega_6\times10^{-20}$ (cm^2)	$\tau_r^{1.5\mu m}$ (ms)
$Cs[Er(hfa)_4]$	Methanol	26.86	0.43	0.89	18
$Er(hfa)_3(H_2O)_2$		23.66	0.69	1.05	17
$Er(acac)_3(H_2O)_2$		21.07	0.94	0.72	22
$Cs[Er(hfa)_4]$	DMSO	14.79	1.00	0.79	16
$Er(hfa)_3(H_2O)_2$		11.99	0.79	1.32	11
$Er(acac)_3(H_2O)_2$		23.52	0.57	0.80	15
$Cs[Er(hfa)_4]$	THF	33.57	-0.24	1.11	
$Er(hfa)_3(H_2O)_2$		22.60	0.47	1.12	13
$Er(acac)_3(H_2O)_2$		17.99	3.52	0.43	21
$Er(tpip)_3$	Chloroform	6.32	0.82	0.34	38
$Er(ftpip)_3$	DMSO	2.37	0.30	1.00	16

Table 3.1. Judd-Ofelt parameters and calculated radiative lifetimes for $Cs[Er(hfa)_4]$, $Er(hfa)_3(H_2O)_2$, $Er(acac)_3(H_2O)_2$, $Er(tpip)_3$ and $Er(ftpip)_3$ in solutions

In the solutions, the calculated radiative lifetime at ~ 1.5 μm emission for each complex was calculated using Judd-Ofelt parameters derived from the measured line strengths of the $^4I_{15/2}\rightarrow{}^4G_{11/2}$, $^4I_{15/2}\rightarrow{}^4G_{9/2}$, $^4I_{15/2}\rightarrow{}^4F_{5/2+3/2}$, $^4I_{15/2}\rightarrow{}^4F_{7/2}$, $^4I_{15/2}\rightarrow{}^2H_{11/2}$, $^4I_{15/2}\rightarrow{}^4S_{3/2}$ and $^4I_{15/2}\rightarrow{}^4F_{9/2}$ transitions in the

absorption spectra of the UV-visible band. The measured line strengths of the $^4I_{11/2} \rightarrow {}^4I_{15/2}$ (~ 980 nm) and $^4I_{13/2} \rightarrow {}^4I_{15/2}$ (~ 1.5 μm) transition were excluded from the measurements.

However, in the crystals, the radiative lifetime at ~ 1.5 μm emission for each complex has both calculated results and experimentally measured results. The Judd-Ofelt parameters for the complexes in crystals are listed in table 3.2.a along with the calculated raditive lifetimes (Calc. $\tau_{r1.5\mu m}$), measured radiative lifetimes (Meas. $\tau_{r1.5\mu m}$), calculated line strengths ($S_{calc1.5\mu m}$) and measured line strengths ($S_{meas1.5\mu m}$). In order to compare the results in solutions, the Judd-Ofelt parameters in crystals, without considering the IR transitions, are listed in Table 3.2.b along with the calculated line strengths ($S_{calc1.5\mu m}$) and the calculated radiative lifetimes (Calc. $\tau_{r1.5\mu m}$).

Crystal	JO param.		$S_{calc}^{1.5\mu m}$	$S_m^{1.5\mu m}$	$\tau_r^{1.5\mu m}$ Calc.	Meas.
	$\times 10^{-20}$ (cm^2)		$\times 10^{-20}$ (cm^2)	$\times 10^{-20}$ (cm^2)	(ms)	(ms)
$Cs[Er(hfa)_4]$	Ω_2	7.11	1.12	1.00	20.9	23.4
	Ω_4	0.35				
	Ω_6	0.65				
$Er(hfa)_3(H_2O)_2$	Ω_2	19.59	2.11	2.10	9.5	~ 9.5
	Ω_4	0.15				
	Ω_6	1.19				
$[Er(acac)_3(H_2O)_2]$ $(H_2O)(CH_3CH_2OH)$	Ω_2	9.77	1.17	1.20	17.4	16.9
	Ω_4	0.90				
	Ω_6	0.63				
$Er(tpip)_3$	Ω_2	4.06	0.91	0.94	19.0	18.4
	Ω_4	0.04				
	Ω_6	0.58				
$Er(ftpip)_3$	Ω_2	6.93	1.30	1.34	13.0	12.6
	Ω_4	1.00				
	Ω_6	0.73				

Table 3.2.a. Judd-Ofelt parameters, calculated/measured line strengths and calculated/measured radiative lifetimes of $Cs[Er(hfa)_4]$, $Er(hfa)_3(H_2O)_2$, $Er(tpip)_3$, $Er(ftpip)_3$ and $[Er(acac)_3(H_2O)_2](H_2O)(CH_3CH_2OH)$ in crystal format derived from UV-visible-IR absorption

Crystal		$\Omega_2\times10^{-20}$ (cm^2)	$\Omega_4\times10^{-20}$ (cm^2)	$\Omega_6\times10^{-20}$ (cm^2)	$S_{calc}^{1.5\mu m}$ (cm^2)	Calc. $\tau_r^{1.5\mu m}$ (ms)
$Cs[Er(hfa)_4]$	(1)	7.34	-0.17	1.15	1.77	13.2
$Er(hfa)_3(H_2O)_2$	(2)	19.84	-0.37	1.64	2.69	7.9
$[Er(acac)_3(H_2O)_2](H_2O)(CH_3CH_2OH)$	(3)	9.86	0.71	0.82	1.44	14.7
$Er(tpip)_3$	(4)	4.11	-0.07	0.66	1.02	17.4
$Er(ftpip)_3$	(5)	6.82	1.26	0.50	0.99	17.5

Table 3.2.b. Judd-Ofelt parameters and calculated radiative lifetimes of $Cs[Er(hfa)_4]$, $Er(hfa)_3(H_2O)_2$, $Er(tpip)_3$, $Er(ftpip)_3$ and $[Er(acac)_3(H_2O)_2](H_2O)(CH_3CH_2OH)$ in crystal format derived from UV-visible absorption without IR absorption

The investigation on the Judd-Ofelt parameters for each complex need to consider the errors derived from experimental measurements and mathematical calculations. The experimental error would be due to many factors: the measuring errors for the optical paths, calculating errors of the concentrations of Er^{3+} ions, and variations for refractive indices. The variation of the refractive index of each solvent is < 5% according to the information from the supplier (Aldrich-Sigma). The refractive index of each crystal was estimated using the Becke line test and Cargile refractive index liquids, which derives a measuring error < 2%. The variation of the concentration of Er^{3+} ions in a solution is due to the measuring error of the

scale used to weigh the mass of the complex. The variation of the concentration of Er^{3+} ions in crystals is due to the error of the measurement of the optical path that is the thickness of the crystal. The resolution of the scale used to weigh the powder was 0.5 mg and the resolution of the microscopy used to measure the thickness of crystals was ~ 5 μm. These errors for concentrations were controlled < 5%. Moreover, a numerical investigation that we did shows that the variations of the Judd-Ofelt parameters resulted from the variation of the concentration or refractive index at < 10%.

The error of the fitting is determined by the root-mean-square (rms) deviation in the least-square fitting between the calculated line strengths and measured line strengths. This error is due to the least-square fitting treating the difference between each set of calculated line strength and measured line strength as having the same weight in view of minimising the overall difference between the overall sets of all accounted calculated line strengths and measured line strengths. The total rms deviations identify the summation of all variations between each calculated line strength and measured line strength, so that the smallest total rms deviations means the best-fitted Judd-Ofelt parameters. The total rms deviations between the overall measured line strengths and calculated line strengths are listed in table 3.3. This table includes the total rms deviations for all complexes in solutions over the UV-vis band, corresponding crystals over the UV-vis

band and corresponding crystals over the UV-vis-IR band.

Material	Solvent	rms×10^{-20}	rms×10^{-20} (crystal UV-vis)	rms×10^{-20} (crystal UV-vis-IR)
$Cs[Er(hfa)_4]$	Methanol	5.03	1.96	1.66
	DMSO	2.49		
	THF	6.64		
$Er(hfa)_3(H_2O)_2$	Methanol	4.74	3.86	3.27
	DMSO	1.79		
	THF	4.35		
$Er(acac)_3(H_2O)_2$	Methanol	3.23	3.00	2.54
	DMSO	3.51		
Crystal: $[Er(acac)_3(H_2O)_2](H_2O)(CH_3CH_2OH)$	THF	2.75		
$Er(tpip)_3$	Chloroform	2.10	8.15 x10^{-2}	9.47 x10^{-2}
$Er(ftpip)_3$	DMSO	5.58	6.56 x10^{-2}	5.58 x 10^{-1}

Table 3.3. The total rms deviations for all complexes in solution format over UV-vis band, corresponding crystal format over UV-vis band and corresponding crystal format over UV-vis-IR band

In table 3.3, the fitting results for the line strengths of the fluorinated-related $CsEr(hfa)_4$ and $Er(hfa)_3(H_2O)_2$ in DMSO solutions have nearly half the total rms deviations compared to the total rms deviations in

methanol or THF solutions. In the hydrated-related $Er(acac)_3(H_2O)_2$, there is no remarkable difference among the fitting results in DMSO, methanol and THF solutions. In the $CsEr(hfa)_4$ crystal, the fitting results show an improvement compared to the fitting results in solutions. For example, the rms deviation for the $CsEr(hfa)_4$ crystal over the UV-vis-IR band is ~ 3 times less than the rms deviation for the $CsEr(hfa)_4$ in THF. The fitting results for the $Er(hfa)_3(H_2O)_2$ crystal and $Er(acac)_3(H_2O)_2$ related-crystal have the compatible rms deviations to the corresponding complexes in solutions. Moreover, the fitting results for the $Er(ftpip)_3$ crystal and $Er(tpip)_3$ crystal give ~ 10 to ~ 100 times less rms deviations than the rms deviations for the corresponding complexes in solutions. For instance, the rms deviation for the $Er(ftpip)_3$ crystal over the UV-vis-IR band is 6.56 (10^{-22}) cm^2, but the rms deviation for the $Er(ftpip)_3$ in DMSO is 5.58 (10^{-20}) cm^2. This result means that the least-square fitting on the measured line strengths, derived from the absorption spectra of the crystals of erbium complexes, could produce better fitting results for the calculated line strengths and Judd-Ofelt parameters.

3.1.2. Ω_2s of organic fluorinated and hydrogenated erbium complexes in solutions and crystals

In figure 3.1, the light scattering variously influences the absorption spectra of the Er^{3+} ions in the methanol, THF and DMSO below ~ 440 nm

wavelength, where the $^4G_{11/2} \rightarrow {}^4I_{15/2}$ transition at ~ 378 nm wavelength is included. In figure 3.1.a, the light scattering is strong for $CsEr(hfa)_4$ in DMSO, particularly for the band below ~ 400 nm wavelength, and light scatterings in THF and methanol are comparable. In figure 3.1.b, the light scattering in DMSO is also strong for $CsEr(hfa)_4$ in the band extending to ~ 500 nm wavelength, while the influences in methanol and THF are relatively weaker. But, in figure 3.1.c, the light scattering in THF for $Er(acac)_3(H_2O)_2$ is strongest than those in methanol and DMSO. And, in figure 3.1.d, the light scattering for $Er(ftpip)_3$ in DMSO is very intense. The solvent effect on the intensity, shape or bands in UV/visible absorption spectra strongly depends on the solvent-solute interactions and solvent nature. And, the attempts to relate to this effect are commonly complicated since they consider many physical solvent properties such as relative permittivity, dipole moment or refractive index.[114,115] These influences mean that when one absorption peak is integrated, the background of light scattering is subtracted so that the absolute value of the integrating peak is strongly varied, depending on the overlapping between the background of light scattering and intrinsic absorption spectrum of Er^{3+} ions.

An analysis based on the Judd-Ofelt parameters of $CsEr(hfa)_4$, $Er(hfa)_3(H_2O)_2$ and $Er(acac)_3(H_2O)_2$ in methanol, THF and DMSO could provide some information that the intrinsic spectral transitions of Er^{3+} complexes would be affected by solvent molecules coordinated with Er^{3+}

ions.

1: The symmetry of the surrounding environment to the central Er^{3+} ion increases with four hfa^- ligands coordinated to the Er^{3+} ion. Hence, the site-symmetry of the Er^{3+} ion in the $(hfa^-)_4$ environment is higher than that of the Er^{3+} ion in $(hfa^-)_3(H_2O)_2$, of which this phenomena can be observed from the molecular structures of $CsEr(hfa)_4$ and $Er(hfa)_3(H_2O)_2$. In addition, in the $Er(hfa)_3(H_2O)_2$, the dihydates sit opposite the group of $(hfa^-)_3$ on the counter-plane. This structure could further decrease the symmetry around the Er^{3+} ion. In this case, the hypersensitivity of the Er^{3+} ion in the $(hfa^-)_3(H_2O)_2$ ligand environment should be intrinsically higher than that of the Er^{3+} ion in the $(hfa^-)_4$ ligand-environment. However, in table 3.1, the Ω_2s of the Er^{3+} ion in the $(hfa^-)_3(H_2O)_2$ ligand environment in methanol and DMSO are unexpectedly smaller than those of the Er^{3+} ion in the $(hfa^-)_4$ ligand environment in methanol and DMSO. Moreover, it is observed that the $CsEr(hfa)_4$ in THF solution has a negative value of Ω_4, which is inconsistent with the Judd-Ofelt theory, since Judd-Ofelt parameters with negative values of Ωs have no physical significance, and the absorption of $CsEr(hfa)_4$ in the THF environment is more intense at the hypersensitive transitions than those in methanol and DMSO environments, as seen in figure 3.3.a. We assign this failure of the Judd-Ofelt theory on $CsEr(hfa)_4$-THF solutions might be due to the fact that THF molecules tend more towards coordination to the Er^{3+} ion or Cs^+ ion, so that the

environment of $(hfa^-)_4$ ligands surrounding the Er^{3+} ion might be distorted or destroyed by the coordinated THF molecules acting as a strong Lewis base. A Lewis base is a species that donates a pair of electrons to a Lewis acid to produce a Lewis adduct. In this case, the THF molecule can be a strong Lewis base and $CsEr(hfa)_4$ can be a Lewis acid. In addition, considering the fact that the Cs^+ ion can adopt a maximum coordination number greater than 6-coordination in solution, the acid base reaction could cause $CsEr(hfa)_4$ to decompose by the segregation of Cs(hfa) or Cs(THF), since the Cs^+ ion could form a complex with a Lewis base. This also matches the fact that some Cs(hfa) crystals were found after recrystallisation.

2: The various influences of the different solvents result in the uncertainties for quantifying the Ω_2 of an individual complex, especially for the fluorinated complexes. The Ω_2s of $CsEr(hfa)_4$ in methanol and DMSO have a variation of ~ 57% with the results that Ω_2 in methanol is 26.86 (10^{-20}) cm^2 and Ω_2 in DMSO is just 14.79 (10^{-20}) cm^2. The Ω_2s of $Er(hfa)_3(H_2O)_2$ in methanol, DMSO and THF have a variation up to ~ 60% with the results that the biggest Ω_2 in methanol is 23.66 (10^{-20}) cm^2 and the smallest Ω_2 in DMSO is 11.99 (10^{-20}) cm^2. On the other hand, the hydrogenated complex is observed to be less influenced by solvent molecules. The Ω_2s of $Er(acac)_3(H_2O)_2$ in methanol, DMSO and THF have a variation of < 30% with the results that the biggest Ω_2 in DMSO is

23.56 (10^{-20}) cm^2 and the smallest Ω_2 in THF is 17.99 (10^{-20}) cm^2. Moreover, another special fact is observed that DMSO reduces the Ω_2s for the fluorinated complexes $Er(hfa)_3(H_2O)_2$ and $CsEr(hfa)_4$, which might mean that some coordinated solvent molecules increase the site symmetry of Er^{3+} ions in the fluorinated complexes.

In crystals, the absorption spectra of crystal samples make a difference to the Judd-Ofelt parameters. First of all, the absorption spectra has no longer the background of light scattering, especially over the UV-visible band. Secondly, all crystal samples used in the measurement of absorption spectra are the same crystal samples determined by an x-ray diffraction measurement, so the solvent effect should be removed or clarified quantitatively. Thirdly, the molecular structure and site-symmetry of each complex can be identified to analyse the correlation of structural characteristics and Judd-Ofelt parameters.

1: The results show that the $(hfa^-)_3$ coordinated environment decreases the site-symmetry of the central Er^{3+} ions because the Ω_2s of $(hfa^-)_3$ coordinated $Er(hfa)_3(H_2O)_2$ and $(acac^-)_3$ coordinated $Er(acaca)_3(H_2O)_2$ are bigger than the Ω_2 of $(hfa^-)_4$ coordinated $Cs[Er(hfa)_4]$. It is observed that the absorptions of $Er(hfa)_3(H_2O)_2$ and $[Er(acac)_3(H_2O)_2]$ $(H_2O)(CH_3CH_2OH)$ crystals in figure 3.2.a are more intense than the absorption of $Cs[Er(hfa)_4]$ crystal, especially at the hypersensitive transitions of $^4I_{15/2}\rightarrow{}^4G_{11/2}$ and $^2H_{11/2}\rightarrow{}^4I_{15/2}$. The reason is clarified through a comparison among the

molecular structures of these complexes: the Er^{3+} ions in $CsEr(hfa)_4$ and in $Er(hfa)_3(H_2O)_2$ are coordinated to the same hfa^- ligand so that the electron distribution should be similar at the coordinated bond of Er-O for both complexes. In this case, the site-symmetry of Er^{3+} ions would dominate the strengths of the spectral transitions. The higher site-symmetry of the Er^{3+} ion in $(hfa^-)_4$ can be observed from the structure of $[Er(hfa)_4]^-$ that has the analogous square anti-prismatic shape formed by the central Er^{3+} ion and four ligands, This structure is more symmetrical than the trigonal-pyramidal shape formed by the central Er^{3+} ion and the $(hfa^-)_3(H_2O)_2$ group, since the dihydrates sit opposite to the $(hfa^-)_3$ ligand group. The lesser symmetry of $Er(hfa)_3(H_2O)_2$ consequently gives a bigger Ω_2.

Furthermore, a similar tendency occurs for the $[Er(acac)_3(H_2O)_2]$-$(H_2O)(CH_3CH_2OH)$ crystal, which has more hypersensitivity than $Cs[Er(hfa)_4]$. There is a group of one H_2O and one CH_3CH_2OH recrystallised away from the molecule of $Er(acac)_3(H_2O)$, because the group of $(H_2O)(CH_3CH_2OH)$ is believed to attach the molecule due to the hydrogen bond without the coordination with the Er^{3+} ion. Nevertheless, the $(acac^-)_3$-ligands sit opposite the dihydrates so that the site-symmetry of the Er^{3+} ion is lower than the site-symmetry of the Er^{3+} ion in the $(hfa^-)_4$ environment. Therefore, the calculation shows that the Ω_2 of $Er(acac)_3(H_2O)_2$ is bigger than the Ω_2 of $CsEr(hfa)_4$. This is also observed

in the absorption spectra where the spectral transitions of $Er(acac)_3(H_2O)_2$ are more intense than those of $Cs[Er(hfa)_4]$.

2: It is observed that the absorption of the fluorinated $Er(hfa)_3(H_2O)_2$ and fluorinated $Er(ftpip)_3$ are stronger than those of the corresponding hydrogenated $Er(acac)_3(H_2O)_2$ and hydrogenated $Er(tpip)_3$, respectively in figures 3.2.a and 3.2.b. This result is also observed that Ω_2s of fluorinated $Er(hfa)_3(H_2O)_2$ and fluorinated $Er(ftpip)_3$ are bigger that those of hydrogenated $Er(acac)_3(H_2O)_2$ and hydrogenated $Er(tpip)_3$.

The difference between the $acac^-$ and hfa^- ligand is that the hydrogen atoms on methyl ($-CH_3$) are fully replaced with the fluorine atoms ($-CF_3$), whilst the coordination bond of Er-O has remained. Similarly, fully replacing H with F is the only difference between $tpip^-$ ligand and $ftpip^-$ ligand. Besides, the similar molecular structures of the analogous trigonal-pyramidal shapes are expectedly observed in $Er(hfa)_3(H_2O)_2$ and $Er(acac)_3(H_2O)_2$, and the similar molecular structures of the analogous cubic shapes are expectedly found in $Er(tpip)_3$ and $Er(ftpip)_3$ either. These facts mean that the site-symmetry could not be causing the different hypersensitive transitions between a fluorinated erbium complex and its corresponding hydrogenated erbium complex. The reason might be the fact that the electronegativity of the fluorinated ligands withdraws the electrons on the 5s5p shell around the coordinated 4f electrons, so that the coordination bond of Er-O in a fluorinated complex is increased compared

to the coordination bond of Er-O in its corresponding hydrogenated complex.

3.1.3. Ω_6s of organic fluorinated and hydrogenated erbium complexes in solutions and crystals

In order to demonstrate the significance of the spectral transitions at the IR band to the Judd-Ofelt analysis for an individual erbium complex, table 3.2.b shows that the Judd-Ofelt analyses for $CsEr(hfa)_4$, $Er(hfa)_3(H_2O)_2$ and $Er(tpip)_3$ fail, since some negative Ω_4s occur without considering the spectral transitions of $^4I_{15/2} \rightarrow {}^4I_{11/2}$ at ~ 980 nm wavelength and $^4I_{15/2} \rightarrow {}^4I_{13/2}$ at ~ 1.5 μm wavelength. However, table 3.2.a shows that the Judd-Ofelt analyses for the corresponding complexes give positive Ω_4s instead. These results mean that spectral transitions over the IR band are required to rationalise the Judd-Ofelt calculations in crystals, especially for the fluorinated erbium complexes, with the exception of $Er(ftpip)_3$. Moreover, the results in table 3.2.a show that each fluorinated erbium complex has bigger Ω_6s than its corresponding hydrogenated erbium complex. For example, there is a relationship that Ω_6 of $Er(tpip)_3$ < Ω_6 of $Er(acac)_3(H_2O)_2(H_2O)(CH_3CH_2OH)$ < Ω_6 of $CsEr(hfa)_4$ < Ω_6 of $Er(hfa)_3(H_2O)_2$ and Ω_6 of $Er(tpip)_3$ < Ω_6 of $Er(ftpip)_3$. The stronger electronegativity of the fluorinated ligands withdraws the shielding 5s5p electrons and coordinated 6s electrons further from the 4f orbitals of the

Er^{3+} ion, so that the electron density shelling the erbium 4f coordination sphere is reduced. The consequent effect would be that the repulsion of the electrons on 4f or 4f5d orbitals towards the ligand is reduced so that the electron density on 4f or 4f5d orbitals is increased, of which the overlapping between 4f and 5d orbitals is increased. This makes the Ω_6s bigger for the fluorinated erbium complexes.

This is also observed in figure 3.2, where the Ω_6-dominated $^4I_{15/2}\rightarrow{}^4I_{13/2}$ transition of $Er(ftpip)_3$ is more intense than that of $Er(tpip)_3$, and the $^4I_{15/2}\rightarrow{}^4I_{13/2}$ transition of $Er(hfa)_3(H_2O)_2$ is the most intense among the complexes of $Er(acac)_3(H_2O)_2(H_2O)(CH_3CH_2OH)$, $CsEr(hfa)_4$ and $Er(hfa)_3(H_2O)_2$.

3.1.3. Shorter radiative lifetime of 1.5 μm emission and higher quantum yield of fluorinated erbium complex

The line strength of the $^4I_{15/2}\rightarrow{}^4I_{13/2}$ transition is quantified by the Judd-Ofelt parameters multiplying their reduced matrix element of $[U^{(6)}]^2 = 1.4299$, $[U^{(4)}]^2 = 0.1173$ and $[U^{(2)}]^2 = 0.0195$, in which the value of $[U^{(6)}]^2$ is nearly 70 times the value of $[U^{(2)}]^2$, whilst the Ω_2s are just < 30 times the Ω_6s in our erbium complexes. This indicates that the Ω_6s dominate the line strength of the $^4I_{15/2}\rightarrow{}^4I_{13/2}$ transition. And, in figure 3.2, the IR absorption of Er^{3+} ions in a fluorinated complex is obviously stronger than the absorption in its corresponding hydrogenated complex. The calculated line

strengths of $^4I_{15/2} \rightarrow {}^4I_{13/2}$ transitions and calculated radiative lifetimes at ~ 1.5 μm emission for the fluorinated and corresponding hydrogenated erbium complexes in table 3.3 show that the fluorinated erbium complexes have stronger line strengths of $^4I_{15/2} \rightarrow {}^4I_{13/2}$ transitions and a shorter calculated radiative lifetime at ~ 1.5 μm emission. For example, $S_{calc1.5\mu m}$s of $Er(hfa)_3(H_2O)_2$ and $Er(ftpip)_3$ are nearly twice as strong than those of $Er(acac)_3(H_2O)_2$ and $Er(tpip)_3$, and $\tau_{r1.5\mu m}$s of $Er(hfa)_3(H_2O)_2$ and $Er(ftpip)_3$ are nearly half those of $Er(acac)_3(H_2O)_2$ and $Er(tpip)_3$. The equation (1-7) indicates that the quantum yield of the $^4I_{15/2} \rightarrow {}^4I_{13/2}$ transition is proportional to $1/\tau_{r1.5\mu m}$, so a shorter $\tau_{r1.5\mu m}$ of the fluorinated erbium complex will improve its quantum yield. Also, this improved quantum yield of the fluorinated erbium complex is due to the longer emission lifetime at ~ 1.5 μm emission, extended by reduced hydrogenated quenching.

The quantum yields at ~ 1.5 μm emission of $CsEr(hfa)_4$, $Er(hfa)_3(H_2O)_2$, Er(ftpip), $Er(acac)_3(H_2O)_2$ and $Er(tpip)_3$ are listed in table 3.4. In the literature, the emission lifetimes of complexes refer to the average emission lifetime $<\tau_{1.5\mu m}>$ derived from the fitting results for the time-resolved photoluminescence at ~ 1.5 μm emission.[11,103]

Complex:	$Cs[Er(hfa)_4]$	$Er(hfa)_3(H_2O)_2$	$Er(acac)_3(H_2O)_2$	$Er(tpip)_3$	$Er(ftpip)_3$
$<\tau_{1.5\mu m}>$	1.8(μs)	1.83(μs)	60(ns)	5(μs)	~ 200(μs)
$<\eta>$	8.6×10^{-3} %	1.9×10^{-2} %	3.5×10^{-4} %	$2.6\ 10^{-2}$ %	1.7%

Table 3.4. The average emission lifetimes of studied complexes and quantum yields of studied complexes derived from calculated radiative lifetimes

It was noted that $Er(hfa)_3(H_2O)_2$ has nearly 54 times increased quantum yield compared to $Er(acac)_3(H_2O)_2$, whilst the emission lifetime of $Er(hfa)_3(H_2O)_2$ is only 30 times longer than that of $Er(acac)_3(H_2O)_2$. $Er(ftpip)_3$ has nearly 60 times increased quantum yield compared to $Er(tpip)_3$ while the emission lifetime of $Er(ftpip)_3$ is only 40 times longer than that of $Er(tpip)_3$.

3.2. Extraordinary sensitisation of $Zn(F\text{-}BTZ)_2$ to $Er(ftpip)_3$

3.2.1. Absorption, photoluminescence and electroluminescence of $Zn(F\text{-}BTZ)_2$

Before displaying and discussing the sensitisation effect from $Zn(F\text{-}BTZ)_2$ to $Er(ftpip)_3$, it is worth understanding the spectroscopic characteristics of $Zn(F\text{-}BTZ)_2$ molecules. Theoretically, a sufficient energy transfer requires that $Zn(F\text{-}BTZ)_2$ has spectral resonance between its excited singlet states (absorption band and fluorescence band), its excited triplet states (phosphorescence band) and the complicated excited states of Er^{3+} ions.

The absorption spectrum of $Zn(F\text{-}BTZ)_2$ was undertaken on a 250

nm-thick $Zn(F\text{-}BTZ)_2$ film deposited on a flat glass substrate under a vacuum < $5(10^{-6}$ $mbar^{-1})$. The absorption spectrum of the film over the UV-visible band was extracted using a Hitachi U-3000 spectrometer. The photoluminescence spectrum of $Zn(F\text{-}BTZ)_2$ was undertaken on $Zn(F\text{-}BTZ)_2$ powder excited by using a 405 nm laser. In order to clarify the singlet and triplet states of $Zn(F\text{-}BTZ)_2$, we present the electroluminescence of a $Zn(F\text{-}BTZ)_2$ based OLED. All the layers of the device were deposited in a high-vacuum (10^{-8} mbar) Kurt J. Lesker thermal evaporation system onto a clean patterned ITO substrate. The 3,3'-dimethyl-$N^4,N^4,N^{4\prime},N^{4\prime}$-tetra-*m*-tolyl-[1,1′-biphenyl]-4,4′-diamine (HMTPD) (50 nm) was used as the hole injection and transport layer. The emissive layer (EML) was a film of $Zn(F\text{-}BTZ)_2$ (20 nm). A 50 nm thickness film of aluminium 8-hydroxyquinolinate (AlQ_3) was used as the electron transport layer (ETL). The cathode consisted of 1 nm LiF with 100 nm of aluminium.[108] The absorption spectrum of the $Zn(F\text{-}BTZ)_2$ film, the photoluminescence spectrum of the $Zn(F\text{-}BTZ)_2$ powder and the electroluminescence of the $Zn(F\text{-}BTZ)_2$ based OLED over 400 nm to 700 nm wavelengths are displayed in figure 3.3.

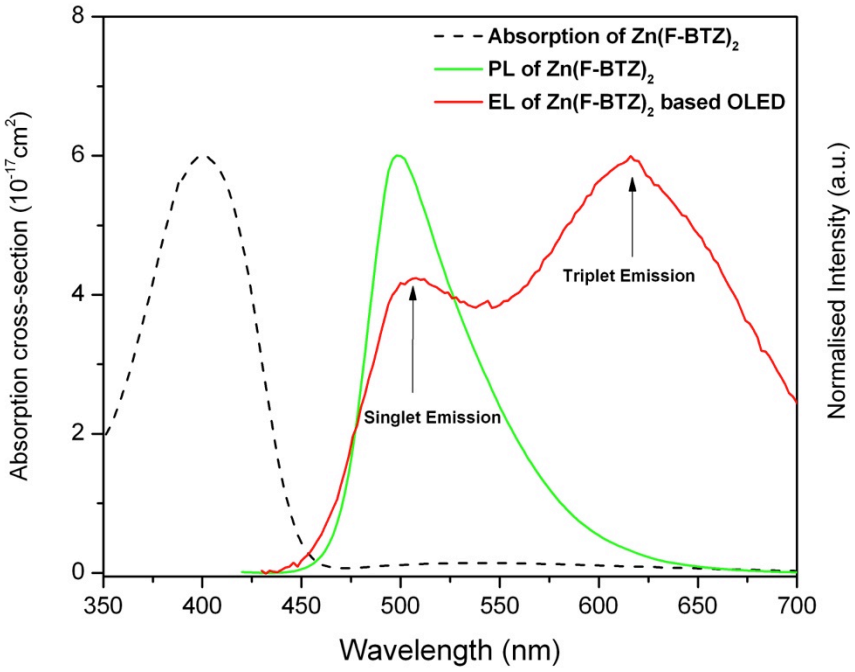

Figure 3.3. The absorption of the 250 nm-thick $Zn(F\text{-}BTZ)_2$ film, the PL spectrum of the pure $Zn(F\text{-}BTZ)_2$ powder and the EL of the $Zn(F\text{-}BTZ)_2$ based OLED.

In the electroluminescence spectrum, the higher energy peak, which is compatible to the photoluminescence band of $Zn(F\text{-}BTZ)_2$, is due to the singlet emission of $Zn(F\text{-}BTZ)_2$ and has a short lifetime of ~ 100 ns.[109] And, the lower energy peak is due to the triplet emission of $Zn(F\text{-}BTZ)_2$ and has a major component of the long lifetime of ~ 50 μs.[116] For the further investigation on the triplet emission, a measurement of the delayed-luminescence in the $Zn(F\text{-}BTZ)_2$ film was performed using an OPO (Vibrant II, Opotek) laser at 430 nm wavelength and detected using an iCCD S20 Gen II Horiba Jobin-Yvon intensified CCD.[109] The pulse of the OPO laser was ~ 7 ns. If detecting luminescence was delayed long enough to avoid the fluorescence and delayed-fluorescence (singlet

emission), the delayed-luminescence would mainly consist of the phosphorescence (triplet emission). The luminescence from the $Zn(F\text{-}BTZ)_2$ film was dispersed in a Triax 320 spectrometer. The lifetime of the delayed-luminescence was measured by integrating the 40 times averaged emission centred at 685 nm wavelength with a changing delay of 50-850 μs and counting for 1100 μs, as displayed in figure 3.4. The fitted curve was obtained by fitting the time-resolved photoluminescence data using a single exponential function, of which the fitting adjusted coefficients of determination R^2 were controlled to be > 0.99.

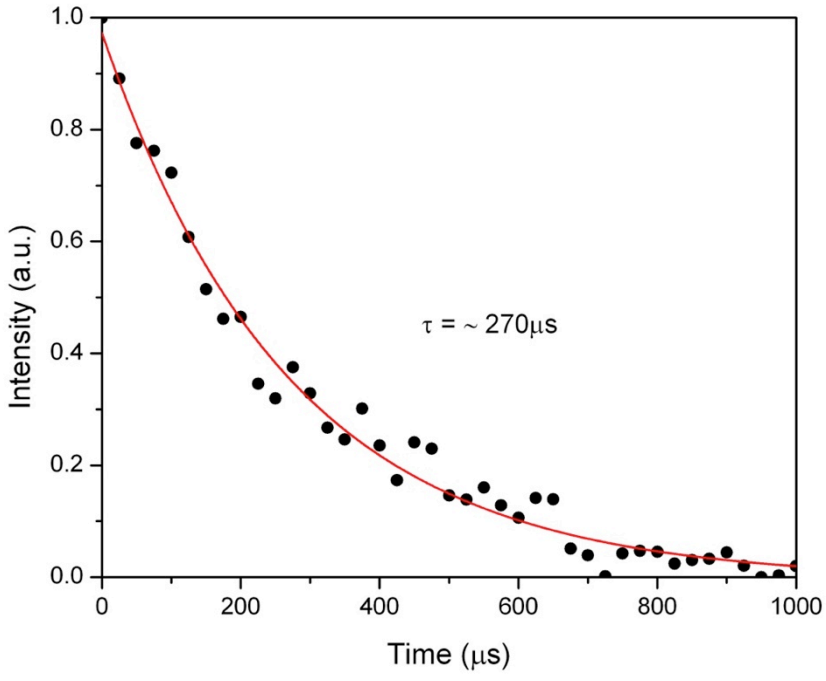

Figure 3.4. Time-resolved delayed-luminescence spectrum at 685 nm emission and fitted decay spectrum.

The fitted lifetime of the delayed luminescence is ~ 270 μs, longer than

the ~ 50 μs triplet emission in the OLED. The reason for this might be attributed to the quenching of the triplets in the OLED.[109] The delayed-luminescence spectrum is displayed in figure 3.5, which shows that the phosphorescence band (triplet emission) over 440 nm to 800 nm wavelengths matches the broad-lower energy band of the triplet emission observed in the OLED.

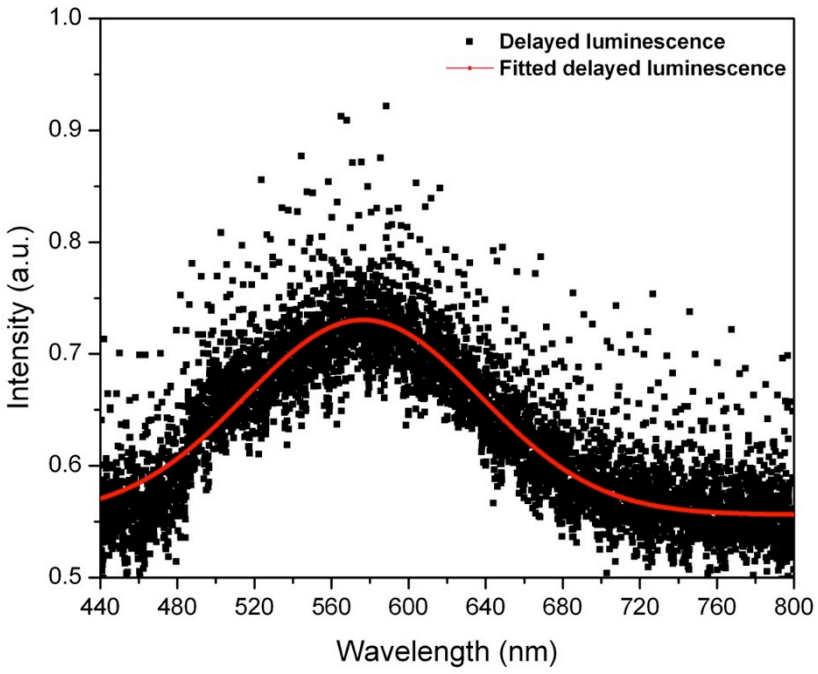

Figure 3.5. Delayed-luminescence spectrum over 440 nm to 800 nm wavelengths, and the fitted delayed-luminescence spectrum was fitted by a Gaussian function

3.2.2. Time-resolved photoluminescence of $Er(ftpip)_3$ and $Zn(F\text{-}BTZ)_2$ co-doped film

According to the absorption data of $Zn(F\text{-}BTZ)_2$ and $Er(ftpip)_3$, $Zn(F\text{-}BTZ)_2$ has a broad absorption over the UV-visible band to ~ 500 nm

wavelength, and $Er(tpip)_3$ has only some intrinsic monochromatic absorption without any organic sensitisation over the same visible band. A ~ 5 ns pulse OPO laser at 430 nm wavelength, at which $Er(ftpip)_3$ is transparent, was used to excite the $Zn(F\text{-}BTZ)_2$ in the co-doped system and an intense ~ 1.5 μm emission was detected. On the other hand, a ~ 5 ns pulse OPO laser at 520 nm wavelength, at which $Zn(F\text{-}BTZ)_2$ is nearly transparent, was used to directly excite the $Er(ftpip)_3$ in the co-doped system to emit ~ 1.5 μm emission. The time-resolved photoluminescence spectra of the 1.5 μm emission from a 300 nm-thick 30% $Er(ftpip)_3$ co-doped film as an example are displayed in figure 3.6. The spectra were integrated 255 times, probed by the Triax 550 spectrometer equipped with 600 lines/mm gratings and 2 mm slit width, and counting for 10 ms.

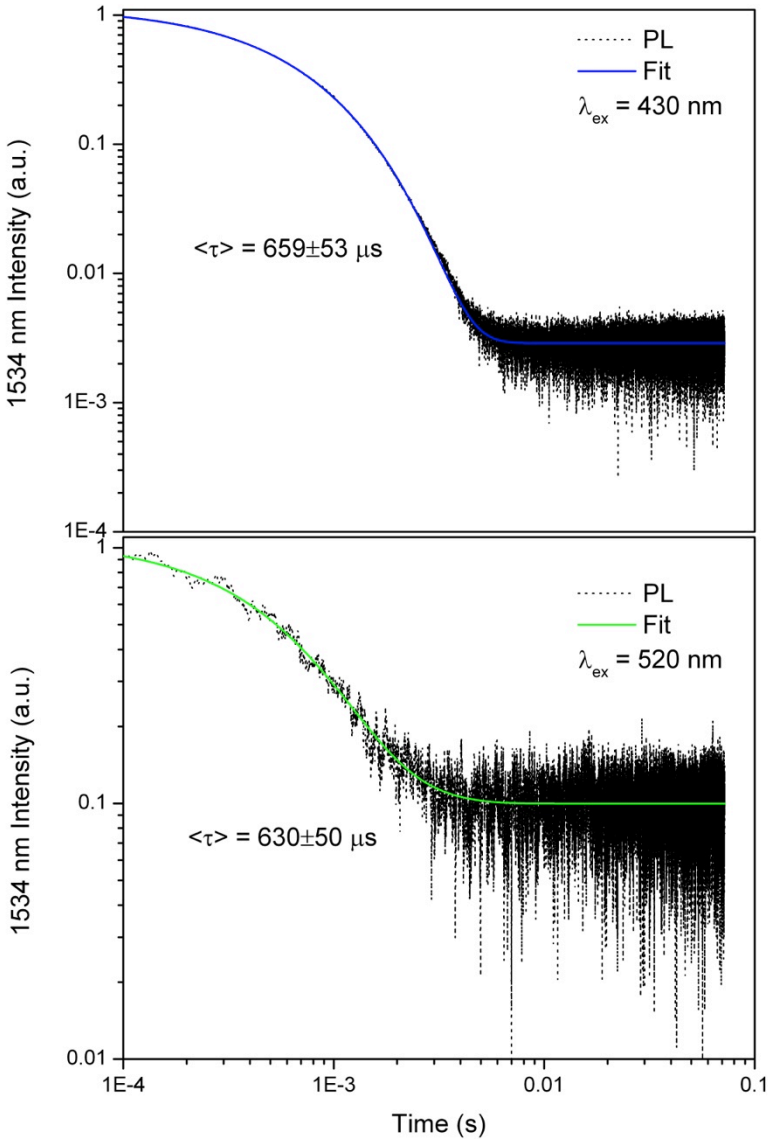

Figure 3.6. Time-resolved photoluminescence spectra (Log_{10} Plot) centred at 1534 nm emission and being excited at 430 nm and 520 nm wavelengths, respectively.

The fitted curves were obtained by fitting the data using a double exponential function, of which the fitting adjusted coefficients of determination R^2 were controlled to be > 0.99. The emission lifetime is presented by the average emission lifetime <τ>. Moreover, the experimental variation for extracting the time-resolved spectra could introduce further measuring errors on the fitted results. Here, we assume a total error of ~ 16% bar for fitting the average emission lifetimes at 1.5 μm

emission of this 300 nm-thick 30% $Er(ftpip)_3$ co-doped film, through fitting the varied time-resolved photoluminescence spectra. These photoluminescence spectra were extracted from different measurements, considering the different counting time, integrating times, emission wavelengths (~ 1534 ± 5 nm), angles of incident light ray on the sample, and objective images at the entrance slit of the Triax 550 spectrometer. In figure 3.6, the lifetime at 1534 nm wavelength derived from the indirect excitation of $Zn(F\text{-}BTZ)_2$ at 430 nm wavelength is 659±53 μs, and the direct excitation of $Er(ftpip)_3$ at 520 nm wavelength is 630±50 μs. With considering the measuring errors, it is demonstrated that the sensitisation from $Zn(F\text{-}BTZ)_2$ to $Er(ftpip)_3$ has not reduced the lifetime at 1534 nm emission of Er^{3+} ions in the co-doped system. The lifetime in this sample is longer than the lifetime of ~ 0.2 ms in pure $Er(ftpip)_3$ powder. This is believed to be due to the dilution of the Er^{3+} ions concentration in this sample.

So, it is worth investigating the lifetimes of 1534 nm emission at various $Er(ftpip)_3$ doped ratios in co-doped systems, where the concentrations of Er^{3+} ions are diluted by the doped $Zn(F\text{-}BTZ)_2$. The time-resolved photoluminescence measurements were undertaken on various co-doped films where the doped $Er(ftpip)_3$ ratios are 5%, 10%, 20%, 22%, 30%, 35%, 46%, 60%, 75% and 100%. The averaged emission lifetimes of these samples are displayed in figure 3.7, considering the 16%

error bar for the corresponding concentrations of Er^{3+} ions.

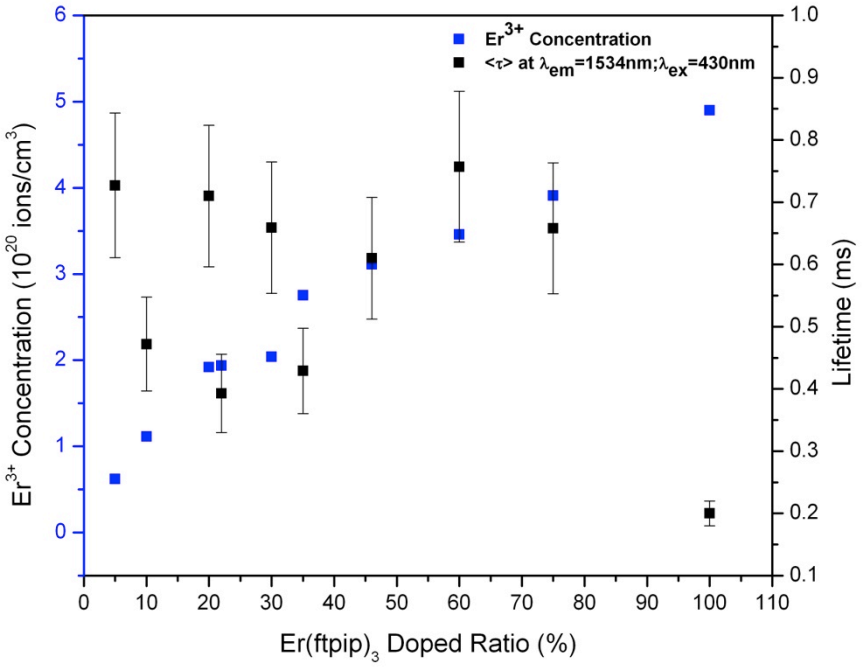

Figure 3.7. The average lifetimes of 1534 nm emission against the corresponding $Er(tpip)_3$ doped ratio and the corresponding concentrations of Er^{3+} ions in the co-doped system.

It is observed that the concentrations of $Er(ftpip)_3$ in co-doped films are < ~ 5 (10^{20}) cm^{-3}, even at the high dilution of 75%, and the average emission lifetimes of 1534 nm emission are approximately ~ 700 µs, considering the ~ 16% error bar. It might suggest that there was barely a concentration quenching for $Er(ftpip)_3$ in the co-doped system below a 75% doping ratio. The reason for this might be that the concentrations of Er^{3+} ions around ~ 1 to 5 (10^{20}) cm^{-3} are close to the quenching concentrations of Er^{3+} ions, which are identical to some values reported in some traditional

erbium-doped glasses or sol-gel thin films.[117,118]

3.2.3. Excitation and emission spectra of $Er(ftpip)_3$ and $Zn(F\text{-}BTZ)_2$ co-doped films

In order to demonstrate the sensitisation effect in the co-doped system, an excitation measurement was performed on a 300 nm-thick 30% $Er(ftpip)_3$ co-doped film. The monochromatic lights for exciting the sample was obtained by using a Triax 180 spectrometer to disperse the white light output from an Arc lamp. A 190 Model optical chopper modulated the monochromatic lights as 123 Hz giving 4 ms long pulse light. The power density of the monochromatic lights shone on the sample was in the range of ~ 7 mW/cm^2. The continuous monochromatic lights were aligned and reflected by a set of metallic mirrors, and focused by a set of convex lens onto the film. The 1534 nm emission was probed by a Triax 550 spectrometer equipped with a 2 mm slit width, recorded using a lock-in amplifier, and the spectrum was extracted on a PC. The sample was fixed on a home-made sample stage, which fixes its vertical and horizontal positions, and can rotate the angle of the sample to the incident light beam.

The excitation spectrum was corrected on the intensity spectrum of continuous monochromatic lights. The intensity spectrum of the monochromatic lights incident on the sample was detected using a 818-UV silicon diode detector and recorded using a lock-in amplifier, considering

the responsivity of 3510 Modulator versus wavelengths from the supplier. The responsivity versus wavelengths was one nonlinear relationship between the converted electric signal and the detected light intensity at wavelengths. The 818-UV silicon diode detector was settled on the exact position (vertical, horizontal and the angular position) of the co-doped sample. The corrected excitation spectrum recorded at 1534 nm emission from the 30% $Er(ftpip)_3$ co-doped system is displayed in figure 3.8, where the normalised absorption, photoluminescence and electroluminescence of $Zn(F\text{-}BTZ)_2$ are also plotted. The absorption of $Er(ftpip)_3$ crystal over the UV-visible band is also given along with the excitation spectrum.

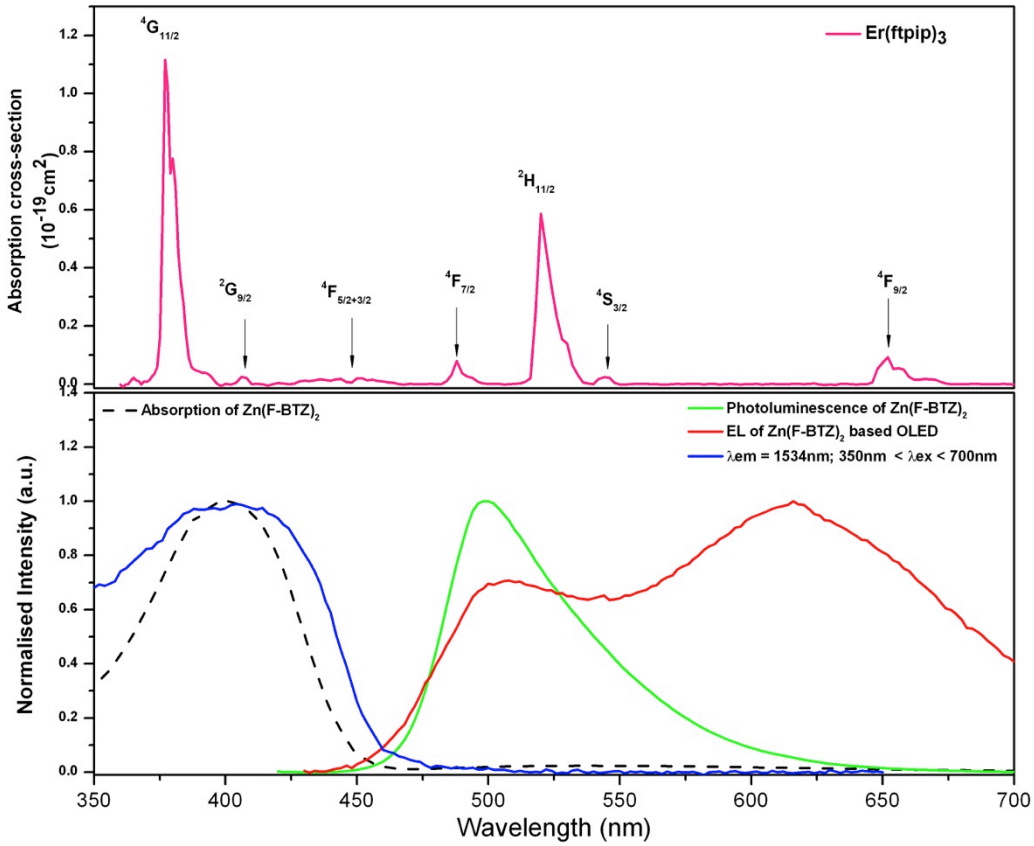

Figure 3.8. The excitation spectrum of a 30% $Er(ftpip)_3$ co-doped system over 350 nm to 700 nm wavelengths. The normalised absorption, photoluminescence and electroluminescence of $Zn(F\text{-}BTZ)_2$ are inserted over the same spectral band. The absorption of $Er(ftpip)_3$ crystal is compared over the same spectral band. That the wider excitation band than the absorption band of $Zn(F\text{-}BTZ)_2$ is due to these two spectra has been normalised in intensity.

In figure 3.8, it is observed that the absorption, and photoluminescence and electroluminescence of $Zn(F\text{-}BTZ)_2$ overlap a number of visible absorption bands of $Er(ftpip)_3$. And, the excitation band of the co-doped film is resonant with the absorption band of $Zn(F\text{-}BTZ)_2$ from 350 nm to 500 nm. This suggests that the sensitisation for the doped Er^{3+} ions would be due to the energy transfer from the excited states of $Zn(F\text{-}BTZ)_2$ to the excited states of $Er(ftpip)_3$.

It is noteworthy that the direct excitation of the hypersensitive $^2H_{11/2}$ transition at ~ 520 nm wavelength of $Er(ftpip)_3$ cannot be seen because it is below the sensitisation limitation in this sample. In the excitation spectrum, if we integrate the spectrum over an area from 350 nm to 510 nm wavelengths, and do the similar integration over an area from 515 nm to 530 nm considering the experimental noise of the data, the value of the integration (350 nm to 510 nm) over the integration (515 nm to 530 nm) is ~ 10,000, which gives a sensitisation effect of 10^4 times the intrinsic 520 nm excitation of the doped Er^{3+} ions.

Moreover, the absorption band of $Zn(F\text{-}BTZ)_2$ overlaps some intrinsic absorptions of Er^{3+} ions like the $^2G_{9/2}\rightarrow{}^4I_{15/2}$ transition, $^4F_{5/2+3/2}\rightarrow{}^4I_{15/2}$ transition and, especially, the hypersensitive $^4G_{11/2}\rightarrow{}^4I_{15/2}$ transition. Furthermore, both the photoluminescence and singlet emission bands of $Zn(F\text{-}BTZ)_2$ are blue-shifted to the absorption peak of the $^4I_{15/2}\rightarrow{}^2H_{11/2}$ hypersensitive transition of $Er(ftpip)_3$. This might indicate a possible energy transfer route from the single states of $Zn(F\text{-}BTZ)_2$ to the $^4F_{7/2}$, $^4S_{3/2}$ and $H_{11/2}$ levels of $Er(ftpip)_3$. In addition, both the broad delayed-luminescence and triplet emission bands also overlap the $^4I_{15/2}\rightarrow{}^2H_{11/2}$ hypersensitive transition at 520 nm wavelength, the $^4I_{15/2}\rightarrow{}^4S_{3/2}$ transition at 540 nm wavelength and the $^4I_{15/2}\rightarrow{}^4F_{9/2}$ transition at 655 nm wavelength of $Er(ftpip)_3$, which might indicate a sufficient energy transfer process from the triplet states of $Zn(F\text{-}BTZ)_2$ to the $^2H_{11/2}$,

$^4S_{3/2}$ and $^4F_{9/2}$ levels of $Er(ftpip)_3$.

The photoluminescence of the co-doped film at the excitation of a 405 nm laser is displayed in figure 3.9.a as well as the photoluminescence of $Er(ftpip)_3$ powder at the excitation of a 375 nm laser. It is observed that the emission of the co-doped film is ~ 3 nm blue-shifted to the emission band of $Er(ftpip)_3$ powder. This is due to the optical interference in the thin film. The optical interference effect is occurring because the light passes through two flat reflective surfaces. The tiny gap between the top and bottom reflective surface means the light rays have two distinct optical paths and interference when they combine. When the difference of the optical path is the even multiple of $\lambda/2$, the intensity of light rays will be reinforced, otherwise, when the difference of the optical path is the odd multiple of $\lambda/2$, the intensity of light rays will be cancelled. When the emission spectrum is especially broad, the various monochromatic light rays will have different optical interferences in a thin film, so that the emission spectrum could have blue or red shifts.

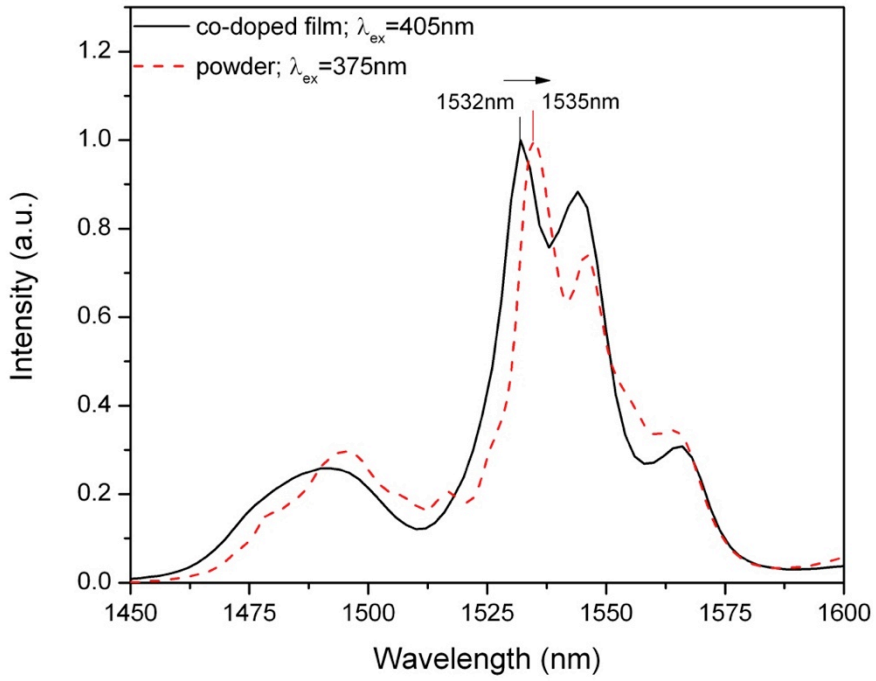

Figure 3.9.a The emission spectrum over ~ 1.5 μm band of the 300 nm-thick 30% $Er(ftpip)_3$ co-doped film and the emission spectrum of powdered $Er(ftpip)_3$

In order to demonstrate the optical interference for the emission spectrum over the 1534 nm band in the co-doped system, several emission spectra of the same co-doped film, displayed in figure 3.9.b, were extracted at different incident angles of the laser beam. The incident angle was the angle (45˚ ~ 90˚) between the laser ray and the film surface. A Triax 550 spectrometer equipped with the 600 lines/mm of gratings and 1 mm slit width probed the emission, where the linear dispersion was 1.5 nm/mm.

It is observed that the emission spectra at the incident angle of 45˚ and 60˚ are centred at 1532 ± 0.75 nm. The emission spectrum at the incident angle of 75˚ tends to be red-shifted though it is centred at 1532 ± 0.75 nm.

And the emission spectrum at the incident angle of 90˚ is centred at 1535 ± 0.75 nm, which matches the centred emission of $Er(ftpip)_3$ powder.

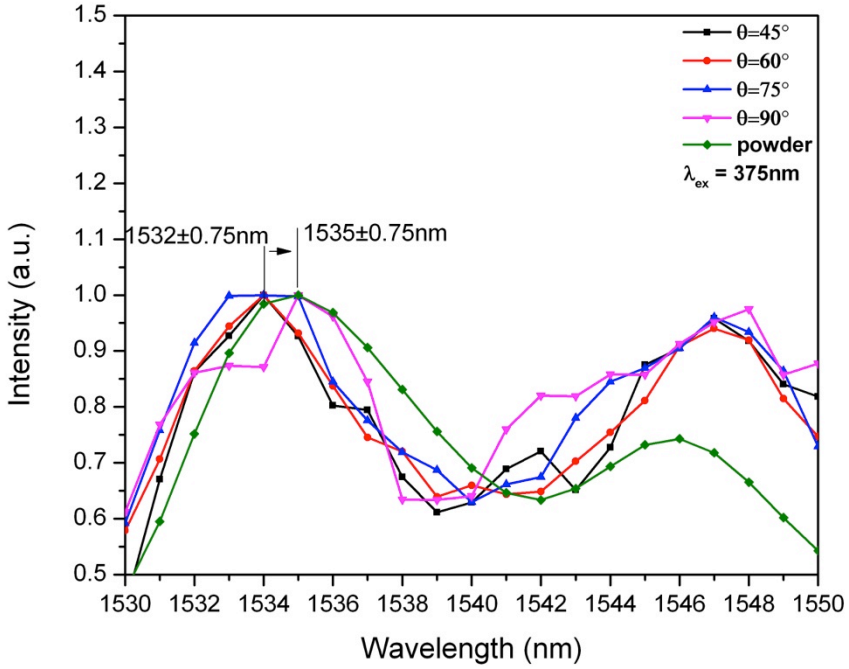

Figure 3.9.b. The red-shift of the emission spectra of the 300 nm-thick 30% $Er(ftpip)_3$ co-doped film due to the optical interference in the film

3.2.4. Demonstration of sensitisation and energy transfer

(1) The energy transfer process

It has been observed that, when the 300 nm-thick 30% $Er(ftpip)_3$ co-doped film is excited using a 5 ns pulse OPO laser, the rise-time τ_{rise} is ~ 0.6 μs. The pulse energy density was ~ 0.14 J/cm^2 in 5 ns (~ 28 MJ/ cm^2). The time-resolved photoluminescence of the 1534 nm emission using the 5 ns pulse OPO laser is displayed in figure 3.10.a.

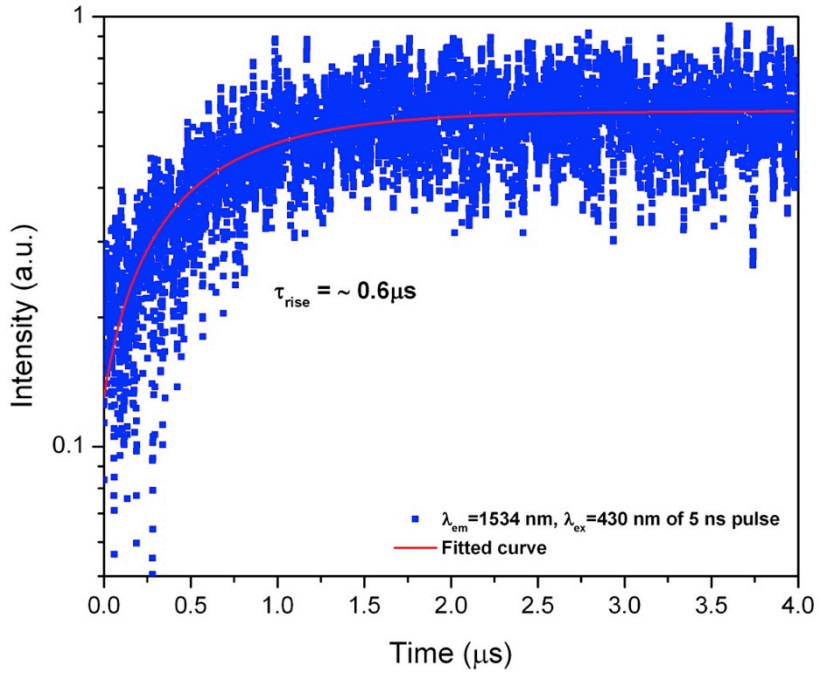

Figure 3.10.a. The time-resolved photoluminescence spectrum at 1534 nm emission for the rise-process and the fitted rise-curve at the excitation of the 5 ns OPO pulse laser

This ~ 0.6 μs rise-time could be due to both the fast energy transfer processes from $Zn(F\text{-}BTZ)_2$ to $Er(ftpip)_3$ and the internal transition processes between excited states of Er^{3+} ions. On the other hand, the time-resolve photoluminescence at 1534 nm emission using a 7 ms long-pulse 405 nm laser is displayed in figure 3.10.b.

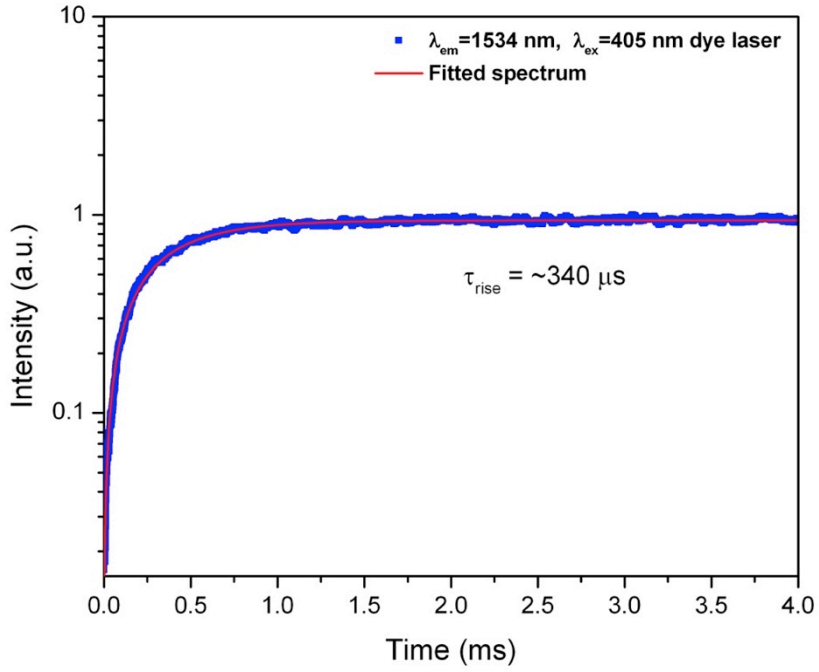

Figure 3.10.b. The time-resolved photoluminescence spectrum at 1534 nm emission for the rise-process and the fitted rise-curve at the excitation of a 7 mW long-pulse 405nm laser with 1 mW power

The power density was just ~ 10 mW/cm^2 compared to 5 ns pulse OPO laser, and the rise-time τ_{rise} was fitted to be ~ 340 μs by using a single exponential function, which is much longer than the rise-time obtained at the excitation of 5 ns pulse OPO laser. The reason for this is that, at the excitation of the 4 ms long-pulse laser with ~ 10 mW/cm^2, the rise-time for the 1534 nm emission is dependent to its long lifetime (~ 0.7 ms) according to the equation (2-6).

In order to demonstrate the difference of the sensitisation effect for Er(ftpip)$_3$ in the 4 ms long-pulse and the 5 ns pulse excitation, an excitation spectrum at the 1534 nm emission of a 500 nm 30% Er(ftpip) co-doped

film was measured by using continuous 5 ns pulse OPO lasers. The excitation spectrum from 410 nm to 570 nm wavelength derived from the 5 ns pulse OPO lasers is displayed in figure 3.11, and the excitation spectrum derived from the 123 Hz monochromatic lights in figure 3.8 is plotted also over the same band.

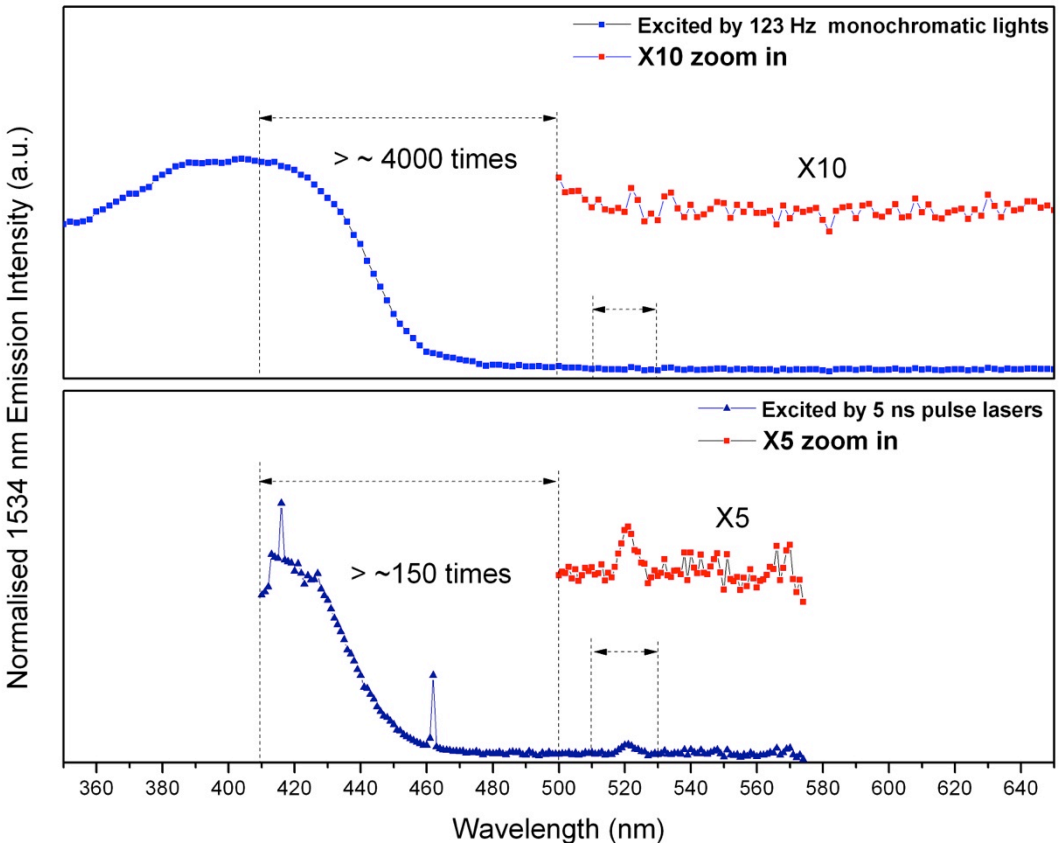

Figure 3.11. The excitation spectra of the 1534 nm emission excited by 123 Hz monochromatic lights and 5 ns pulse OPO lasers. The spike at 463 nm is due to the leaked Idler lasers. The dashed lines show the wavelength region used to integrate the spectra

In the excitation spectra, if we integrate the excitation spectrum derived from the 123 Hz monochromatic lights from 410 nm to 510 nm

wavelengths and do the integration over 515 nm to 530 nm wavelengths, the value of the integration (410 nm to 510 nm) over the integration (515 nm to 530 nm) gives a sensitisation effect of ~ 4000 times. And, if we do the similar integrations on the excitation spectrum derived from the continuous 5 ns pulse OPO lasers over the same band, it gives a sensitisation effect of ~ 150 times. At the excitation of the 5 ns pulse OPO lasers with ~ 28 MJ/cm^2 power, the singlet states of $Zn(F\text{-}BTZ)_2$ can be populated sufficiently due to the lifetime of the singlet emission is very short (< 100 ns), hence, the energy transfer process is believed to be mainly from the singlet states into the $Er(ftpip)_3$, which gives a ~ 150 times sensitisation effect for the Er^{3+} ions. However, at the excitation of the 123 Hz monochromatic lights, the exciting time is 4 ms much longer compared to 5 ns of the pulse OPO lasers, ~ 0.7 ms of the 1534 nm emission and ~ 270 μs of the triplet emission of $Zn(F\text{-}BTZ)_2$. And, it derives a ~ 4000 times sensitisation effect for the Er^{3+} ions. The reason for this might be that the exciting time is long enough to populate sufficient triplet states of $Zn(F\text{-}BTZ)_2$. Therefore, in the energy transfer process, the energy transfer from the triplet states of $Zn(F\text{-}BTZ)_2$ into $Er(ftpip)_3$ would become the main component, which gives the ~ 4000 times sensitisation effect rather than the ~ 150 times sensitisation effect mainly derived from the singlet states.

In order to further demonstrate the existence and importance of the

triplet states of $Zn(F\text{-}BTZ)_2$ in the energy transfer process, a co-doped OLED was fabricated, where the emissive layer was a 20 nm film of $Zn(F\text{-}BTZ)_2$ co-doped with 20% $Er(ftpip)_3$. The substrate, hole injection and transport layer, electron transport layer and cathode were the same with the pure $Zn(F\text{-}BTZ)_2$ un-doped OLED in section 3.2.1. The electroluminescence spectra of un-doped and co-doped OLEDs are plotted in figure 3.12.

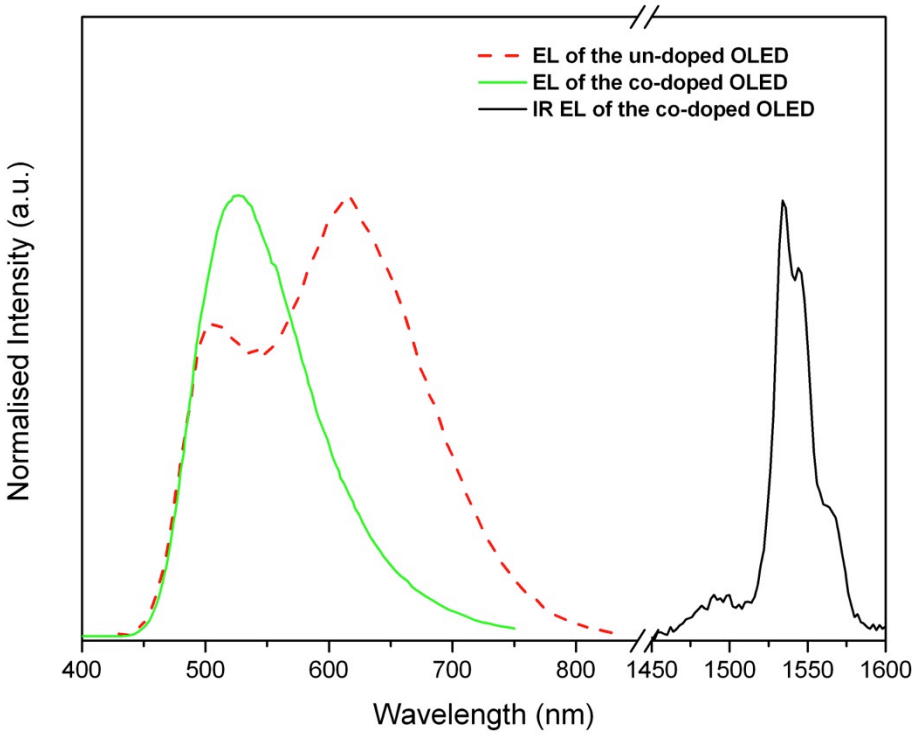

Figure 3.12. The electroluminescence spectra of the 20% $Er(ftpip)_3$ co-doped $Zn(F\text{-}BTZ)_2$ OLED and the un-doped $Zn(F\text{-}BTZ)_2$ OLED. The electroluminescence spectra over the visible and IR bands are normalised. The EL spectrum of the un-doped OLED is the same with the one in figure 3.3

In the electroluminescence of the $Er(ftpip)_3$ co-doped device, the triplet

emission from $Zn(F\text{-}BTZ)_2$ has been completely quenched and is replaced by an intense IR emission, which is from the $^4I_{13/2} \rightarrow {}^4I_{15/2}$ transition of the Er^{3+} ions. This evidence directly proves that the energy of the triplet states of Zn(F-BTZ) is more efficiently transferred into $Er(ftpip)_3$ than the energy transfer from the singlet states.

Then, a Jablonsiki diagram for the co-doped system highlighting the possible energy processes is displayed in figure 3.13. A Jablonski diagram is a diagram that illustrates the electronic states of a molecule and the transitions between them.

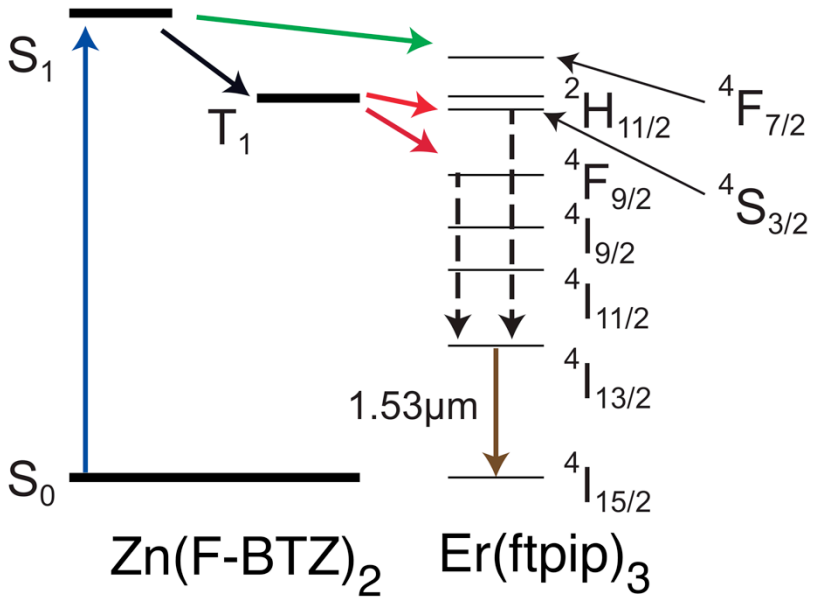

Figure 3.13. The Jablonski diagram for the co-doped system highlighting the energy transfer

In this diagram, the singlet states S_1 of $Zn(F\text{-}BTZ)_2$ are allowed to be excited rapidly in very short time, and the triplet states T_1 of $Zn(F\text{-}BTZ)_2$

are just populated through the intersystem crossing process. The energy can be transferred from the singlet and triplet states into the excited states of $^4F_{7/2}$, $^2H_{11/2}$, $^4S_{3/2}$ and $^4F_{9/2}$ because their energy levels match well the energy levels of the single states and triplet states of $Zn(F\text{-}BTZ)_2$.

(2). Saturated photoluminescence

In order to estimate the maximum luminescence of the doped $Er(ftpip)_3$, a comparison between the 1534 nm emission sensitised from $Zn(F\text{-}BTZ)_2$ using a 405 nm laser and the 1534 nm emission from directly exciting $Er(ftpip)_3$ using a 655 nm laser. The photon densities of the 405 nm and 655 nm laser ray shining on a 100 nm-thick 30% $Er(ftpip)_3$ co-doped film were calibrated to be the same. An aperture of 4 mm diameter was set in front of the film in order to ensure the same incident angle, shining position and focusing for both the 405 nm and 655 nm laser ray on the film. Both the 405 nm and 655 nm laser rays were modulated with 23 Hz, which gave the 20 ms length for the laser pulses. The signal intensities were measured using a Model 5029 lock-in amplifier. The emission intensities derived from the excitation of the 405 nm laser and the excitation of the 655 nm laser are displayed in figure 3.14.

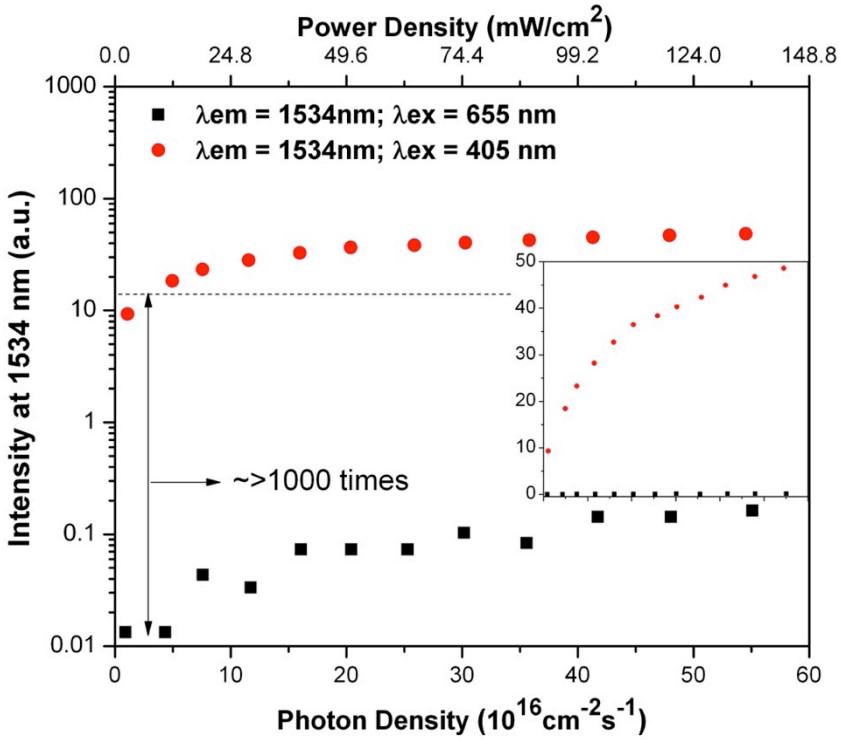

Figure 3.14. The intensities of 1534 nm emission from the 100 nm-thick 30% $Er(ftpip)_3$ co-doped film at the varied power densities of the 405 nm laser and the 655 nm laser. The corresponding photon density was ranged from ~ 1 (10^{16} $cm^{-2}s^{-1}$) to ~ 55 (10^{16} $cm^{-2}s^{-1}$). The inserted graph show the data plotted in the linear axis

The 1534 nm emission derived from the sensitisation effect tend toward saturation over a photon-density range of 10 (10^{16}) $cm^{-2}s^{-1}$ to 55 (10^{16}) $cm^{-2}s^{-1}$, whilst the emission derived from the direct excitation at 655 nm wavelength approximately linearly increases with the increasing photon density. This might suggest that the $Er(ftpip)_3$ molecules in the co-doped system would possibly achieve the population inversion due to the sensitisation effect. From the figure 3.14, the sensitised 1534 nm emission are less saturated below photon density < 10 (10^{16}) $cm^{-2}s^{-1}$ so that we could assume that the emission is approximately linear to the increasing photon

density. On the other hand, the 1534 nm emission derived from the direct excitation of the 655 nm laser is approximately linear to the increasing photon density because of the small intrinsic absorption cross-section of $Er(ftpip)_3$ (10^{-19} to 10^{-20} cm^2). Therefore, the comparison estimates that the sensitised emission is ≥ 1000 times the emission derived from the direct excitation, which determines at least a 1000 times sensitisation effect for $Er(ftpip)_3$ at the excitation of the 405 nm laser.

(3). High rise-rate at low exciting power and population inversion

In the equation (2-5), the rise-rate R_{rise} for an excited state is equal to both the pump rate R_p adding the decay rate $R_{1.5\mu m}$, when the material is excited at a long-pulse laser, longer than the decay lifetime of the excited state. In figure 3.10.b, for the 300 nm-thick 30% $Er(ftpip)_3$ co-doped film, the rise-time of the 1534 nm emission sensitised from the 7 ms long-pulse 405 nm laser with ~ 10 mW/cm^2 power density is ~ 340 μs, shorter than the lifetime of the 1534 nm emission (~ 0.7 ms). So, the corresponding rise-rate is ~ 2200 s^{-1}. In order to investigate rise-rates changing with increasing exciting power, the rise-rates (τ_{rise}^{-1}) of 1534 nm emission at varied exciting power densities of the 7 ms long-pulse 405nm laser are plotted in figure 3.15. The rise-times of the 1534 nm emission are obtained by fitting the time-resolved photoluminescence spectra of the 1534 nm emission using single exponential functions.

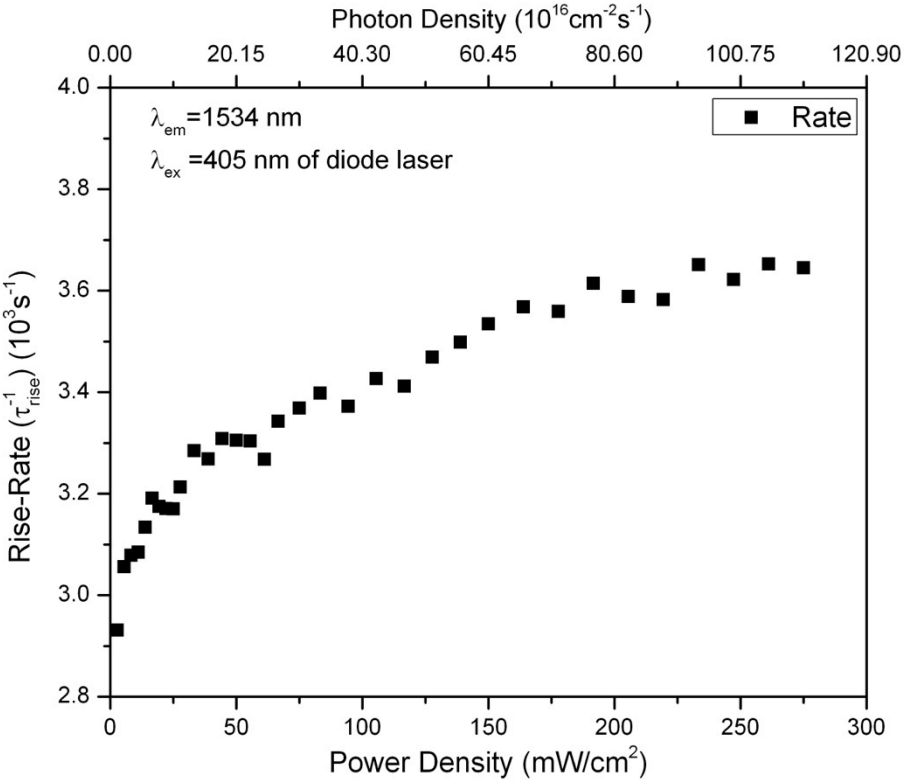

Figure 3.15. The rise-rates (τ_{rise}^{-1}) of the 1534 nm emission changing with increasing the power density (photon density) of the 7 ms long pulse 405 nm laser

It is observed that the rise-rates of 1534 nm emission are increased from ~ 3000 s^{-1} to 4000 s^{-1}, with increasing the exciting power densities of the 405 nm laser from ~ 1.5 mW/cm^2 to 275 mW/cm^2. According to the two-level modelling of the equation (2-12), the population percentage at the excited state can be evaluated by using the expression of R_p / (R_p + $R_{1.5\mu m}$), where a decay rate $R_{1.5\mu m} \approx 1/\langle\tau_{1.5\mu m}\rangle$ and the rise-rate (R_p + $R_{1.5\mu m}$) = τ_{rise}^{-1} for a 1534 nm emission. When the 50% population is at the excited state, the system goes to the population inversion. If we take the data that the emission lifetime $\tau_{1.5\mu m}$ = ~ 0.7 ms and the condition of R_p / (R_p + $R_{1.5\mu m}$)

= 0.5 for the population inversion, the ideal rise-rate for the population inversion is ~ 3100 s^{-1} for the co-doped system. In figure 3.15, the rise-rates in the co-doped system are obviously bigger than this ideal rise-rate with the photon density higher than the threshold of ~ 10 (10^{16}) $cm^{-2}s^{-1}$ (25 mW/cm^2), which is compatible to the power density (25 mW/cm^2) making the 1534 nm emission to tend saturation in figure 3.14. This also might suggest that the saturation of the sensitised 1534 nm emission in figure 3.14 is due to the population inversion in the co-doped system.

3.3. Gain and population inversion in the co-doped slab waveguide

3.3.1. Optical distribution in asymmetric slab waveguide

With the 10^4 times sensitisation effect, ~ 7% high quantum efficiency of ~ 1.5 μm emission, sensitised-saturating photoluminescence of 1534 nm emission at low exciting power (< 150 mW/cm^2) and high rise-rate at low threshold of exciting power (25 mW/cm^2), the $Zn(F\text{-}BTZ)_2$ and $Er(ftpip)_3$ co-doped system seems a potential gain material for fabricating an organic erbium doped waveguide amplifier.

Therefore, we fabricated an asymmetric slab waveguide, seen in figure 3.16, with a 2 μm co-doped core layer (1) of the refractive index n_1 = 1.64, a 700 nm-lower silicon-dioxide cladding layer (2) of the refractive index n_2 = 1.44, and air as the upper cladding layer (3) of the refractive index n_3 = 1.

There is an interface 13 between the upper cladding layer (air) and the core, and an interface 12 between the core and the lower cladding layer (silicon dioxide).

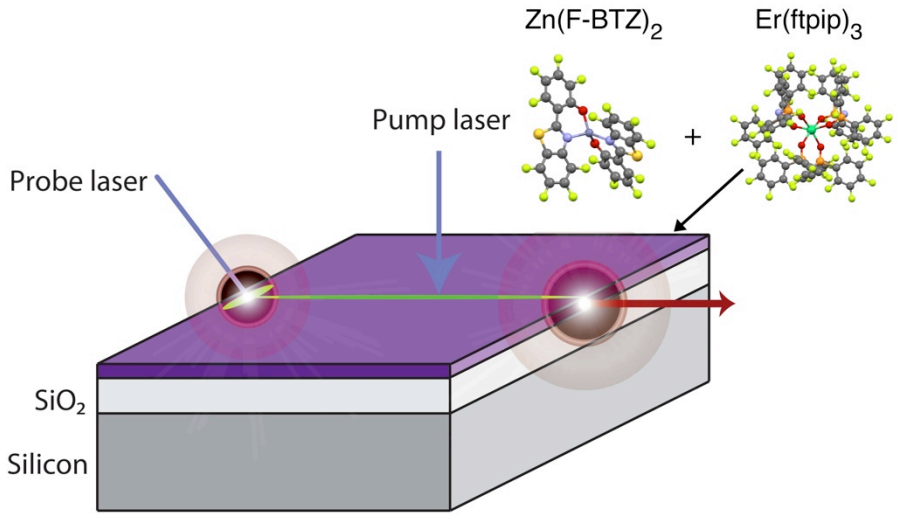

Figure 3.16. The slab waveguide of a 2 μm co-doped layer on a 700 nm SiO_2 cladding layer

The electromagnetic calculation for the 1.5 μm wavelength in our slab waveguide gives the results that there are multiple electromagnetic modes of TE0, TE1, TM0 and TM1. The simulation results for each mode are shown in table 3.5, including the propagation constants β, effective refractive index $n_{eff} = \beta/k_0$, penetration depth Δx_2 in SiO_2 and effective core thickness b_{eff}, according to the equations (2-9).

Mode	Propagation Constant β	Effective Refractive Index $n_{eff} = \beta/k_0$	Penetration Depth (Substrate) Δx_2	Effective Core Thickness b_{eff}
TE0	$6.761(10^6)$	1.614	328 nm	2.6 μm
TE1	$6.414(10^6)$	1.51	459 nm	2.7 μm
TM0	$6.755(10^6)$	1.613	272 nm	2.4 μm
TM1	$6.391(10^6)$	1.526	485 nm	2.7 μm

Table 3.5. The propagation constants, effective refractive index, penetration depth in SiO_2 and effective core thickness

Consequently, the normalised energy flux density along the propagation axis in the waveguide is displayed in figure 3.17, which can be calculated using the Poynting rule according to the equations (2-10) and (2-11).

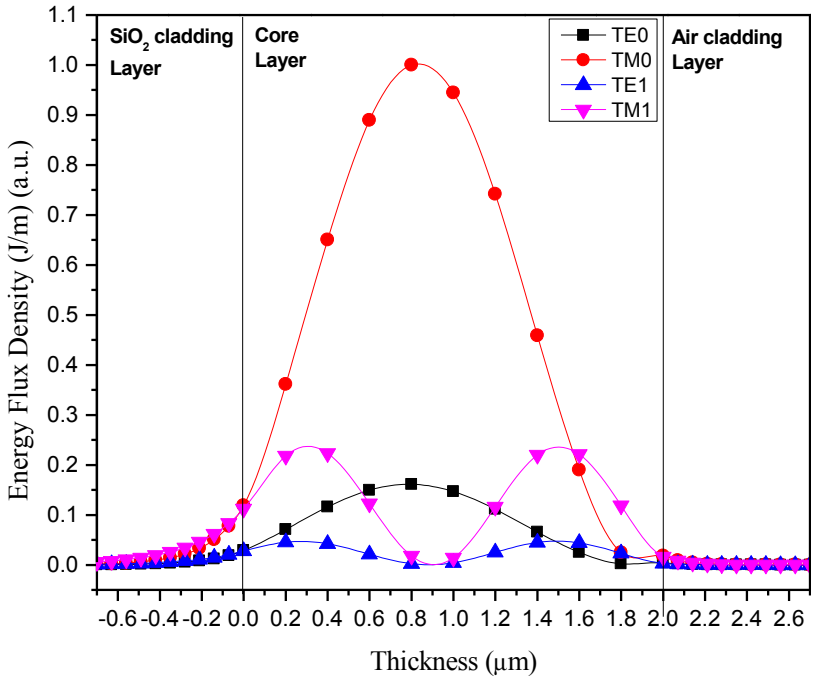

Figure 3.17. The normalised energy flux density in the unit of J/m in our asymmetrical slab waveguide

The calculation for the integration of the energy flux density along the effective core thickness shows that there is 96% optical energy restricted in the core layer.

3.3.2. Time-resolved gain measurement

The time-resolved gain measurement for the slab waveguide was operated using the probe and pump method. The probing 405nm laser ray modulated at 190 Hz was shone onto one edge of the waveguide. The pump laser modulated at 19 Hz with a power of 3 mW was focused as a line of 0.032 cm width and 0.8 cm length by a cylinder convex lens. The modulation was performed using the Model 190 Chopper. The propagating signals coming out from the other edge of the waveguide were probed by the Triax 550 spectrometer equipped with 2 mm slits and 600 lines/mm gratings at 1532 nm wavelength, and detected by the Hamamatsu R5509-72 nitrogen-cooled detector. The signal with 190 Hz was trigged by the reference of the signal with 19 Hz in the LeCroy Waverunner HD4000 oscilloscope. The time-resolved gain signal is displayed in figure 3.18.

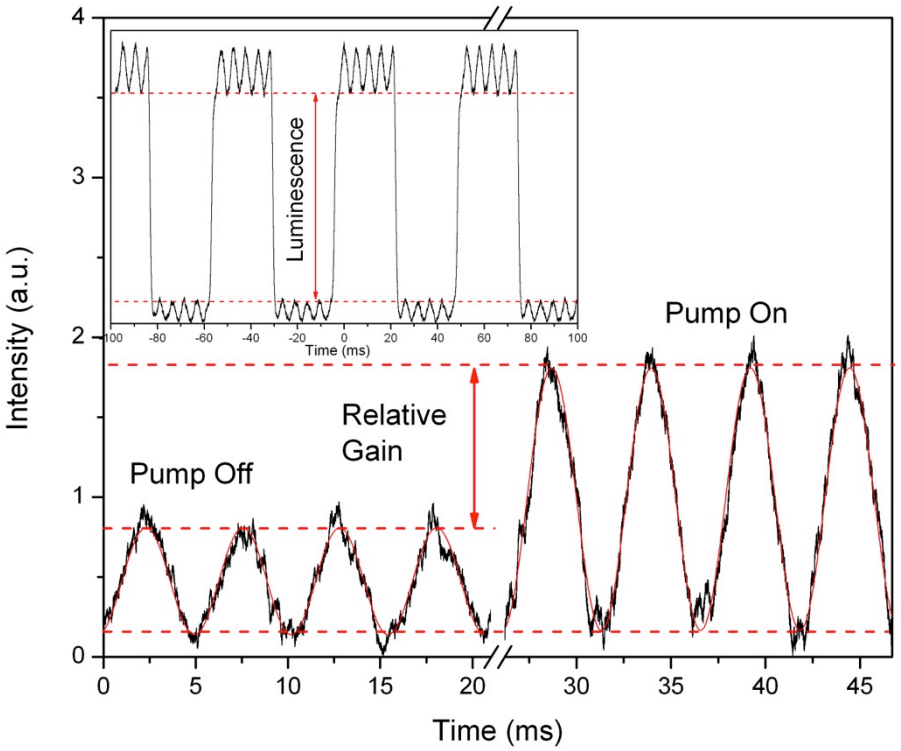

Figure 3.18. The subtracted time-resolved photoluminescence spectrum at 1532 nm emission with the pump laser off and the pump laser on, respectively. The insert graph is the un-subtracted time-resolved photoluminescence spectrum.

The photoluminescence signal was amplified as a factor of 1.9 with the pump on. The measured gain resulted from the magnified signal is 2.7 dB and the real length of the waveguide was 0.8 cm so that the relative gain is 3.4 dB/cm. In the inserted graph of the un-subtracted time resolved spectrum, the strong luminescence is due to the emission from the pump. In this slab waveguide, the absorption loss is due to the absorption of doped $Er(ftpip)_3$. The absorption loss derived from the absorption of $Er(ftpip)_3$ crystal is displayed in figure 3.19. So, the absorption loss in the waveguide is estimated to be -6 dB/cm around 1532 nm wavelength. Therefore, the net internal gain of the waveguide in this measurement is -3.3 dB/cm.

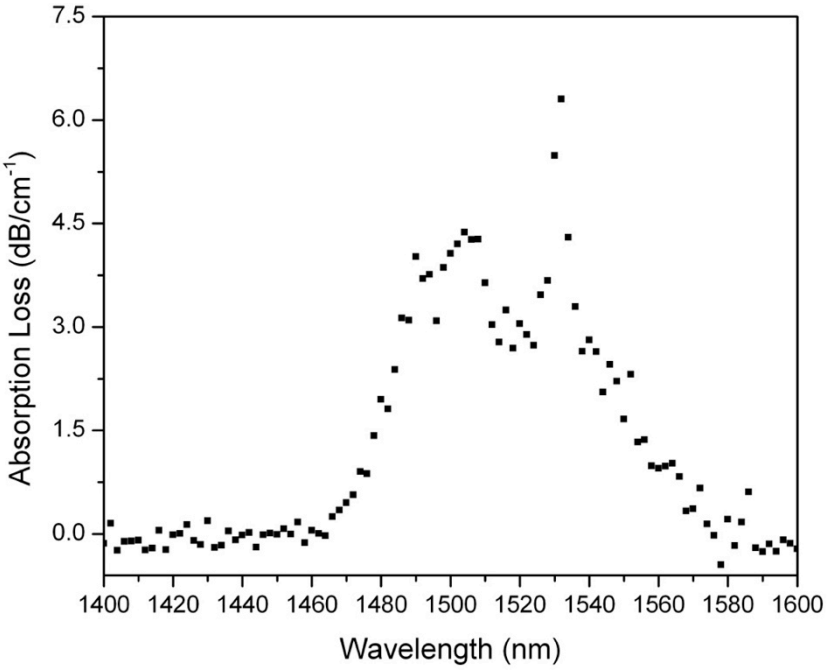

Figure 3.19. The absorption loss due to the absorption of $Er(ftpip)_3$ in the 30% $Er(ftpip)_3$ co-doped system.

In the absorption process, the 1532 nm propagating wave will lose 6 dB/cm since the 100% of the $Er(ftpip)_3$ molecules in the film can be excited into $^4I_{13/2}$ level. So, the 1532 nm propagating wave will lose 3 dB/cm when only 50% of the $Er(ftpip)_3$ molecules can be excited into $^4I_{13/2}$ level, (i.e. where the system approaches the edge of the population inversion). Therefore, the observation of the 3.4 dB/cm relative gain in the waveguide indicates that the pump laser has brought the system into the edge of population inversion.

The pump laser in the measurement was 3 mW on the area of 0.032 ± 0.001 cm × 0.8 cm, which gives a power density of ~ 117 ± 4 mW/cm^2 and a photon density of 38.2 × 10^{16} cm^{-2}s^{-1}. In figure 3.15, this power density

gives a rise-rate of ~ 3400 s^{-1} giving the ~ 58% $Er(ftpip)_3$ molecules being excited according to the equation (2-12). However, if we take the absorption coefficient of $Zn(F\text{-}BTZ)_2$ around 405 nm of ~ 7×10^4 cm^{-1} derived from 0.7 × absolute absorption of $Zn(F\text{-}BTZ)_2$, the 405 nm laser would penetrate into the depth of ~ 0.5 μm in the co-doped layer with the ~ 117 mW/cm^2 power density. Therefore, we estimate that only ~ 25% Er(ftpip) molecules in the co-doped layer has been excited, and the remaining 75% of the $Er(ftpip)_3$ molecules in the co-doped layer will continue to contribute to the absorption loss. The schematic of the light intensity distributing in the core-layer of the waveguide is displayed in figure 3.20.

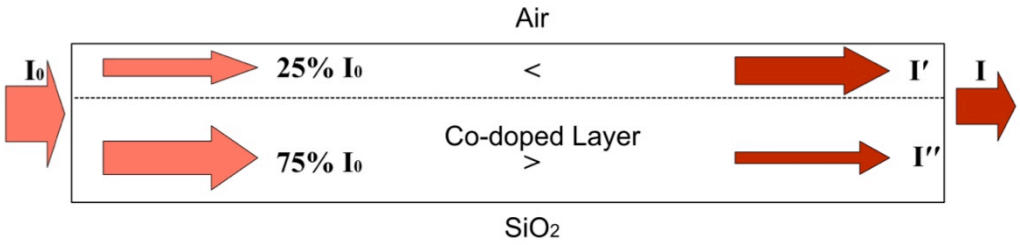

Figure 3.20. The schematic of the light intensity distributing in the core-layer of the waveguide. The I_0 is the intensity of the incident light and I is the transmitted light.

If we assume the intensity of incident light is I_0, the 25% I_0 intensity propagates in the top 25% layer and the 75% I_0 intensity propagates in the rest 75% layer. I′ is the amplified intensity due to the relative gain on the top 25% layer, G, and I″ is the reduced intensity due to the absorption loss

on the 75% layer. I is the intensity of the transmitted light amplified as 3.4 dB/cm. Therefore, the relation among these intensities is expressed:

$$I' = 25\% \times 10^{(G-6)(\mathrm{dB/cm})/10} I_0,$$

$$I'' = 75\% \times 10^{-6(\mathrm{dB/cm})/10} I_0,$$

$$I = I' + I'' = 10^{3.4(\mathrm{dB/cm})/10} I_0,$$

The solution for this set of equation gives the relative gain on the top 25% layer G = 14 dB/cm, which is > 6 dB/cm absorption loss. This suggests that a net gain has been obtained on the top 25% layer, and we have not achieved a net gain in the whole waveguide because the absorption loss exists in the rest 75% layer using the 405 nm laser with 117 mW/cm as pump.

Chapter 4. Summary and Conclusions

Firstly, we have reported a microscopic technique to directly measure the line strengths of the $^4I_{15/2}\rightarrow{}^4I_{13/2}$ and $^4I_{15/2}\rightarrow{}^4I_{11/2}$ transitions of Er^{3+} ions over IR bands in fluorinated organic complexes and hydrogenated organic complexes. These line strengths, which are measured in crystals of organic erbium complexes, are included in a systematic Judd-Ofelt analysis allowing comparison of the results for solutions and crystals. Moreover, our study provides a methodology to quantify the determination of the photoluminescence quantum yield of Er^{3+} ions for an individual organic erbium complex. A detailed summarisation for conclusions are listed below:

(1). The hypersensitive line strengths of Er^{3+} ions in organic erbium complexes in solutions are influenced by various solvent molecules because the Ω_2 of a erbium complex is changed in various solvents. In particular, the THF solvent causes the Judd-Ofelt calculations to fail for Cs^+ ion coordinated four-ligand erbium complexes. The main reason would be that some solvent molecules are easy to coordinate with Er^{3+} ions or even to cause the decomposition of complexes so that the 4f electronic transitions of Er^{3+} ions are consequently changed.

(2). A microscopic set-up for measuring the absorption of crystals is built up using microscopic objective lens to focus the light onto the size of

~ 10 - 20 μm^2. The line strengths of Er^{3+} ions over IR bands derived from measurements for crystals are included in the Judd-Ofelt calculations. The resulting Judd-Ofelt parameters show that the line strengths of IR bands are very crucial to determine the evaluation and success of Judd-Ofelt analyses for organic erbium complexes. Indeed, the Judd-Ofelt parameters including measured line strengths of IR bands demonstrate that the Ω_2s of Er^{3+} ions in complexes are influenced by the symmetry of molecular structures.

(3). It is demonstrated that the line strengths of Er^{3+} ions in fluorinated complexes are stronger than those in non-fluorinated complexes. The fluorination enhances the electronegativity of coordinated ligands to centred Er^{3+} ions so that the coordination bonds of erbium-ligands are stronger, and the results match the observation of larger Ω_2s and stronger hypersensitive transitions in fluorinated erbium complexes. Furthermore, the stronger electronegativity of fluorination also increases the electron densities on $4f^n$ or $4f^{n-1}5d$ orbitals via reducing the electron density on outer shells, so larger Ω_6s are obtained in fluorinated complexes. This result causes the larger line strengths of the $^4I_{15/2} \rightarrow {}^4I_{13/2}$ transition, and the shorter radiative lifetimes for the 1.5 μm emission, which will boost the photoluminescence efficiency by nearly double compared to the corresponding hydrogenated complexes.

Secondly, we have successfully mixed the fully fluorinated erbium complex, $Er(ftpip)_3$ having a long lifetime for the 1.5 μm emission, and

fully fluorinated organic zinc complex, $Zn(F\text{-}BTZ)_2$ having strong absorption and triplet emission, into a uniform film that is deposited on a substrate through co-evaporation for two materials using a vacuum-film-deposition evaporator. This co-doped system shows that there is an extraordinary sensitisation from $Zn(F\text{-}BTZ)_2$ to $Er(ftpip)_3$ at the excitation of broad visible wavelengths, of which the low power is compatible to LEDs or common lamps, whilst the lifetime of 1.5 μm emission for Er^{3+} ions in this co-doped system remains long. A detailed summarisation for conclusions are listed as follows:

(1). The excitation for the co-doped system is over a broad band centred at ~ 400 nm wavelength from UV to ~ 450 nm, which matches the absorption of $Zn(F\text{-}BTZ)_2$. Plus, the singlet and triplet emission of $Zn(F\text{-}BTZ)_2$ extend over the wide visible band centred at ~ 550 nm wavelength, which overlaps all UV-visible excited states of Er^{3+} ions in $Er(ftpip)_3$. Also, the triplet emission of $Zn(F\text{-}BTZ)_2$ disappears in the electroluminescence of the co-doped system based OLED, and is replaced by a very intense luminescence for the 1.5 μm band of Er^{3+} ions. All these results have demonstrated that there is good energy transfer from $Zn(F\text{-}BTZ)_2$ to the Er^{3+} ions in $Er(ftpip)_3$, which is mediated via the triplet states in the $Zn(F\text{-}BTZ)_2$.

(2). The lifetime of 1.5 μm emission sensitised from exciting $Zn(F\text{-}BTZ)_2$ in the co-doped system can be up to ~ 0.8 ms, which is a new

record of the photoluminescence efficiency of ~ 7% in organic erbium complexes. Also, concentration quenching for Er^{3+} ions in $Er(ftpip)_3$ is virtually eliminated by co-doping with $Zn(F\text{-}BTZ)_2$.

(3). The sensitisation effect for the 1.5 μm emission from $Zn(F\text{-}BTZ)_2$ is more than ~ 1000 times that of the intrinsic excitation for $Er(ftpip)_3$ at the excitation of a 405 nm wavelength. Moreover, the intensity of the 1.5 μm emission tends towards saturation at a power density for a 405 nm excitation as low as ~ 150 mW/cm^2. This also matches the observation of a large rise-rate for the 1.5 μm emission at such low exciting power density.

(4). The saturated luminescence, extraordinary sensitisation and large rise-rate have demonstrated that the $Er(ftpip)_3$ and $Zn(F\text{-}BTZ)_2$ co-doped system can be a gain medium for 1.5 μm wavelength at the excitation of visible lights with low power. The simplified modelling also shows that population inversion can be achieved at low pump power.

Finally, we fabricated a slab waveguide amplifier consisting of a 2 μm co-doped layer as a optical guiding film. We observed an absolute gain of 3.4 dB/cm for 1.52 μm wavelength in this fabricated waveguide with it being pumped by a 405 nm diode laser with 3 mW.

Chapter 5. Future work

In this work, there are some worthy methods to improve the application and technological potentials in the future. Firstly, in terms of the amplifier, a commercial blue or white LED can be used to pump the co-doped system. The advantage of this is that the white emission of LEDs is compatible with the broad sensitisation so more wavelengths can deeply penetrate into the co-doped layers in the waveguide for exciting more Er^{3+} ions. Also, a design of a hybrid waveguide can be made for integrating the co-doped system on silicon-based chips with integrated LED pump or directly integrating the co-doped system into an OLED pump in order to produce an electrically pumped waveguide amplifier.

Secondly, although the lifetime of 1.5 μm emission in the co-doped system is long enough to get reasonable population inversion, the emission lifetime is much shorter than the theoretical lifetime. This might be due to impurities, like some hydrocarbons or moisture, during the procedure of fabrication. An improved fabrication environment, for example using a cryopump in the main chamber to remove water and hydrocarbons for the vacuum, could help fabricate a more pure co-doped system for longer emission lifetimes.

Thirdly, in the view that this co-doped system can be a good gain medium, it can be integrated into an OLED in order to make a

electric-pumped vertical cavity-emitting laser at 1.5 μm wavelength as a telecommunication source. Or, the co-doped system can be deposited on some designed Bragg gratings integrated on silicon-based chips to make a distributed feedback laser at 1.5 μm wavelength.

Fourthly, replacing zinc ions with some heavier metallic ions, such as iridium, should enhance the intersystem crossing process. So, the sensitisation effect for the Er^{3+} ions can be increased. And, replacing the Er^{3+} ion with some other lanthanide ion such as Tm^{3+}, Yb^{3+} and Nd^{3+} etc., in coordination with $ftpip^-$ ligands, possibly produces more organic emitters with emitting other colours.

Finally, as for the modelling of the energy transfer process in this co-doped system, the fact that the organic sensitiser is isolated from the erbium complex could simplify the number of rate constants so that the challenge of calculation for the energy transfer processes could be reduced.

References

1 Eliseeva, S. V. & Bünzli, J.-C. G. Rare earths: jewels for functional materials of the future. *New Journal of Chemistry* **35**, 1165-1176 (2011).

2 Dutton, H. J. *Understanding optical communications*. (Prentice Hall PTR New Jersey, 1998).

3 Agrawal, G. *Fibre-optic telecommunication systems*. (Wiley (New York), 1997).

4 Becker, P. M., Olsson, A. A. & Simpson, J. R. *Erbium-doped fiber amplifiers: fundamentals and technology*. (Academic press, 1999).

5 Bünzli, J.-C. G. & Eliseeva, S. V. Basics of Lanthanide Photophysics. *Lanthanide Luminescence* **7**, 1-45 (2010).

6 Bünzli, J.-C. G. & Eliseeva, S. V. Lanthanide NIR luminescence for telecommunications, bioanalyses and solar energy conversion. *Journal of Rare Earths* **28**, 824-842 (2010).

7 Magennis, S. W. *et al.* Time-dependence of erbium(III) tris(8-hydroxyquinolate) near-infrared photoluminescence: implications for organic light-emitting diode efficiency. *Synth Met* **138**, 463-469 (2003).

8 Polman, A. & van Veggel, F. C. Broadband sensitizers for erbium-doped planar optical amplifiers: review. *JOSA B* **21**, 871-892 (2004).

9 Bünzli, J.-C. G. & Piguet, C. Taking advantage of luminescent lanthanide ions. *Chemical Society Reviews* **34**, 1048-1077 (2005).

10 Tan, R. H. C., Motevalli, M., Abrahams, I., Wyatt, P. B. & Gillin, W. P. Quenching of IR Luminescence of Erbium, Neodymium, and Ytterbium β-Diketonate Complexes by Ligand C−H and C−D Bonds. *The Journal of Physical Chemistry B* **110**, 24476-24479 (2006).

11 Mancino, G., Ferguson, A. J., Beeby, A., Long, N. J. & Jones, T. S. Dramatic Increases in the Lifetime of the Er^{3+} Ion in a Molecular Complex Using a Perfluorinated Imidodiphosphinate Sensitizing Ligand. *Journal of the American Chemical Society* **127**, 524-525 (2004).

12 Mech, A. *et al.* Sensitized NIR Erbium(III) Emission in Confined Geometries: A New Strategy for Light Emitters in Telecom Applications. *Journal of the American Chemical Society* **132**, 4574-4576 (2010).

13 Martin-Ramos, P. *et al.* Novel erbium(iii) fluorinated [small beta]-diketonate complexes with N,N-donors for optoelectronics: from synthesis to solution-processed devices. *Journal of Materials Chemistry C* **1**, 2725-2734 (2013).

14 Peng, Y. *et al.* Visible-Range Sensitization of Er^{3+}-Based Infrared Emission from Perfluorinated 2-Acylphenoxide Complexes. *The Journal of Physical Chemistry Letters* **5**, 1560-1563, (2014).

15 De Sa, G. *et al.* Spectroscopic properties and design of highly luminescent lanthanide coordination complexes. *Coordination Chemistry Reviews* **196**, 165-195 (2000).

16 Crosby, G., Whan, R. & Alire, R. Intramolecular energy transfer in rare earth chelates. Role of the triplet state. *The journal of chemical physics* **34**, 743-748 (2004).

17 Crosby, G., Whan, R. & Freeman, J. Spectroscopic studies of rare earth chelates. *The Journal of Physical Chemistry* **66**, 2493-2499 (1962).

18 Latva, M. *et al.* Correlation between the lowest triplet state energy level of the ligand and lanthanide (III) luminescence quantum yield. *Journal of Luminescence* **75**, 149-169 (1997).

19 Quochi, F. *et al.* Ultrafast Dynamics of Intersystem Crossing and Resonance Energy Transfer in Er (III)- Quinolinolate Complexes. *The Journal of Physical Chemistry Letters* **1**, 2733-2737 (2010).

20 Glover, P. B. *et al.* Fully Fluorinated Imidodiphosphinate Shells for Visible- and NIR-Emitting Lanthanides: Hitherto Unexpected Effects of Sensitizer Fluorination on Lanthanide Emission Properties. *Chemistry – A European Journal* **13**, 6308-6320 (2007).

21 Magennis, S. W. *et al.* Time-dependence of erbium(III) tris (8-hydroxyquinolate) near-infrared photoluminescence: implications for organic light-emitting diode efficiency. *Synthetic Metals* **138**, 463-469, (2003).

22 Görller-Walrand, C., Binnemans, K., Gschneidner Jr, K. & Eyring, L. Handbook on the Physics and Chemistry of Rare Earths, vol. 25, 1998. *Chapter* **167**, 101.

23 Gschneidner, K. A., Bünzli, J.-C. G. & Pecharsky, V. K. *Handbook on the physics and chemistry of rare earths*. vol. 37 (Elsevier, 2007).

24 Bethe, H. Termaufspaltung in Kristallen. *Annalen der Physik* **395**, 133-208 (1929).

25 Carnall, W., Goodman, G., Rajnak, K. & Rana, R. A systematic analysis of the spectra of the lanthanides doped into single crystal LaF_3. *The Journal of Chemical Physics* **90**, 3443-3457 (1989).

26 Hatanaka, M. & Yabushita, S. Theoretical Study on the f-f Transition Intensities of Lanthanide Trihalide Systems. *The Journal of Physical Chemistry A* **113**, 12615-12625 (2009).

27 Görller-Walrand, C. & Binnemans, K. in *Handbook on the Physics and Chemistry of Rare Earths* Vol. Volume 25 (eds Karl A. Gschneidner, Jr. & Eyring LeRoy) 101-264 (Elsevier, 1998).

28 Ofelt, G. S. Intensities of Crystal Spectra of Rare Earth Ions. *The Journal of Chemical Physics* **37**, 511-520 (1962).

29 Judd, B. Configuration Interaction in Rare Earth Ions. *Proceedings of the Physical Society* **82**, 874 (1963).

30 Carnall, W. T., Fields, P. R. & Rajnak, K. Electronic Energy Levels in the Trivalent Lanthanide Aquo Ions. I. Pr^{3+}, Nd^{3+}, Pm^{3+}, Sm^{3+}, Dy^{3+}, Ho^{3+}, Er^{3+}, and Tm^{3+}. *The Journal of Chemical Physics* **49**, 4424-4442 (1968).

31 Sardar, D. K., Gruber, J. B., Zandi, B., Hutchinson, J. A. & Trussell, C. W. Judd-Ofelt analysis of the $Er^{3+}(^4f_{11})$ absorption intensities in phosphate glass: Er^{3+}, Yb^{3+}. *Journal of Applied Physics* **93**, 2041-2046 (2003).

32 Rodríguez-Mendoza, U. R. *et al.* Optical characterization, 1.5 μm emission and IR-to-visible energy upconversion in Er^{3+}-doped fluorotellurite glasses. *Journal of Luminescence* **131**, 1239-1248 (2011).

33 Ebendorff-Heidepriem, H., Ehrt, D., Bettinelli, M. & Speghini, A. Effect of glass composition on Judd-Ofelt parameters and radiative decay rates of Er^{3+} in fluoride phosphate and phosphate glasses. *Journal of non-crystalline solids* **240**, 66-78 (1998).

34 Ansari, A. A., Hussain, H. A. & Iftikhar, K. Optical absorption spectroscopic studies on holmium(III) complexes with β-diketone and heterocyclic amines: The environment effect on 4f-4f

hypersensitive transitions. *Spectrochimica Acta Part A: Molecular and Biomolecular Spectroscopy* **68**, 1305-1312 (2007).

35 Wang, H., Qian, G., Wang, Z. & Wang, M. Spectroscopic properties and Judd-Ofelt theory analysis of erbium chelates. *Spectrochimica Acta Part A: Molecular and Biomolecular Spectroscopy* **62**, 146-152 (2005).

36 Karraker, D. G. Hypersensitive transitions of six-, seven-, and eight-coordinate neodymium, holmium, and erbium chelates. *Inorganic Chemistry* **6**, 1863-1868 (1967).

37 Kirby, A. F. & Palmer, R. A. Hypersensitive transition probability in tris(1,3-diphenyl-1,3-propanedionato)aquolanthanides(III). *Inorganic Chemistry* **20**, 4219-4222 (1981).

38 Slooff, L. H. *et al.* Optical properties of erbium-doped organic polydentate cage complexes. *Journal of Applied Physics* **83**, 497-503 (1998).

39 Liang, H., Zheng, Z., Chen, B., Zhang, Q. & Ming, H. Optical studies of Er (DBM)3Phen containing methyl methacrylate solution and poly (methyl methacrylate) matrix. *Materials chemistry and physics* **86**, 430-434 (2004).

40 Jørgensen, C. & Judd, B. R. Hypersensitive pseudoquadrupole transitions in lanthanides. *Molecular Physics* **8**, 281-290 (1964).

41 Judd, B. R. Ionic transitions hypersensitive to environment. *The Journal of Chemical Physics* **70**, 4830-4833 (1979).

42 Karraker, D. G. Coordination of lanthanide acetates. *Journal of Inorganic and Nuclear Chemistry* **31**, 2815-2832 (1969).

43 Karraker, D. G. Hypersensitive transitions of hydrated neodymium-(III)holmium-(III) and erbium-(III) ions. *Inorganic Chemistry* **7**, 473-479 (1968).

44 Henrie, D., Fellows, R. & Choppin, G. Hypersensitivity in the electronic transitions of lanthanide and actinide complexes. *Coordination Chemistry Reviews* **18**, 199-224 (1976).

45 Rajasekar, N. & Soundararajan, S. Complexes of lanthanide nitrates with 2-N-(6-picoIyl)-benzamide. *Proc. Indian Acad. Sci. (Chem. Sci.)* **89**, 263-267 (1980).

46 Pappalardo, R. Absorption Spectra of Erbium Tricyclopentadienide at Liquid-Helium Temperature. *The Journal of Chemical Physics* **49**,

1545-1554 (1968).

47 Krupke, W. F. Optical absorption and fluorescence intensities in several rare-earth-doped Y_2O_3 and LaF_3 single crystals. *Physical Review* **145**, 325 (1966).

48 Kisliuk, P., Krupke, W. F. & Gruber, J. B. Spectrum of Er^{3+} in Single Crystals of Y_2O_3. *The Journal of Chemical Physics* **40**, 3606-3610 (1964).

49 Kandpal, H. & Joshi, K. Temperature dependence of hypersensitive transitions of Eu^{3+} in different glass matrices. *Journal of non-crystalline solids* **101**, 243-248 (1988).

50 Choppin, G. R. & Fellows, R. L. HYPERSENSITIVITY IN COMPLEXES OF Nd(III) AND Ho(III) WITH MONOBASIC LIGANDS. *Journal of Coordination Chemistry* **3**, 209-215 (1974).

51 Fellows, R. L. & Choppin, G. R. HYPERSENSITIVITY IN COMPLEXES OF Nd(III) AND Ho(III) WITH DIBASIC AND POLYBASIC LIGANDS. *Journal of Coordination Chemistry* **4**, 79-85 (1974).

52 Henrie, D. & Henrie, B. Oscillator strengths of ff transitions in hexachloroneodymium (III) anion. *Journal of Inorganic and Nuclear Chemistry* **36**, 2125-2128 (1974).

53 Peacock, R. in *Rare Earths* Vol. 22 *Structure and Bonding* Ch. 3, 83-122 (Springer Berlin Heidelberg, 1975).

54 Blasse, G. in *Spectra and Chemical Interactions* Vol. 26 *Structure and Bonding* Ch. 2, 43-79 (Springer Berlin Heidelberg, 1976).

55 Jørgensen, C. K. Electron transfer spectra of lanthanide complexes. *Molecular Physics* **5**, 271-277 (1962).

56 Barnes, J. C. & Pincott, H. Electron transfer spectra of some solid lanthanide(III) complexes. *Journal of the Chemical Society A: Inorganic, Physical, Theoretical*, 842-845 (1966).

57 Newman, D. & Balasubramanian, G. Parametrization of rare-earth ion transition intensities. *Journal of Physics C: Solid State Physics* **8**, 37 (1975).

58 Mason, S. F., Peacock, R. D. & Stewart, B. Ligand-polarization contributions to the intensity of hypersensitive trivalent lanthanide transitions. *Molecular Physics* **30**, 1829-1841 (1975).

59 Peacock, R. D. The charge-transfer contribution to the intensity of hypersensitive trivalent lanthanide transitions. *Molecular Physics* **33**, 1239-1246 (1977).

60 Peacock, R. D. The intensities of laporte forbidden transitions of the d-and f-block transition metal ions. *Journal of Molecular Structure* **46**, 203-227 (1978).

61 Mason, S., Peacock, R. & Stewart, B. Dynamic coupling contributions to the intensity of hypersensitive lanthanide transitions. *Chemical Physics Letters* **29**, 149-153 (1974).

62 Kirby, A. F. & Palmer, R. A. Single-crystal electronic absorption of tris(1,3-diphenyl-1,3-propanedionato)aquoneodymium(III): oscillator strength of the $^4I_{9/2}$ .fwdarw. $^4G_{5/2}$ hypersensitive transition. *Inorganic Chemistry* **20**, 1030-1033 (1981).

63 Jørgensen, C. K. & Reisfeld, R. Judd-Ofelt parameters and chemical bonding. *Journal of the Less Common Metals* **93**, 107-112 (1983).

64 Tanabe, S., Sugimoto, N., Ito, S. & Hanada, T. Broad-band 1.5 μm emission of Er^{3+} ions in bismuth-based oxide glasses for potential WDM amplifier. *Journal of luminescence* **87**, 670-672 (2000).

65 Tanabe, S., Ohyagi, T., Todoroki, S., Hanada, T. & Soga, N. Relation between the Ω_6 intensity parameter of Er^{3+} ions and the ^{151}Eu isomer shift in oxide glasses. *Journal of Applied Physics* **73**, 8451-8454 (1993).

66 Tanabe, S., Ohyagi, T., Soga, N. & Hanada, T. Compositional dependence of Judd-Ofelt parameters of Er^{3+} ions in alkali-metal borate glasses. *Physical Review B* **46**, 3305 (1992).

67 Nageno, Y., Takebe, H., Morinaga, K. & Izumitani, T. Effect of modifier ions on fluorescence and absorption of Eu^{3+} in alkali and alkaline earth silicate glasses. *Journal of non-crystalline solids* **169**, 288-294 (1994).

68 Tanabe, S. Optical transitions of rare earth ions for amplifiers: how the local structure works in glass. *Journal of non-crystalline solids* **259**, 1-9 (1999).

69 Daldosso, N. *et al.* Absorption cross section and signal enhancement in Er-doped Si nanocluster rib-loaded waveguides. *Applied Physics Letters* **86**, 261103 (2005).

70 Lourenço, M., Gwilliam, R. & Homewood, K. Extraordinary optical

gain from silicon implanted with erbium. *Applied Physics Letters* **91**, 141122-141123 (2007).

71 Slooff, L. H. *et al.* Rare-earth doped polymers for planar optical amplifiers. *Journal of Applied Physics* **91**, 3955-3980 (2002).

72 Li, Z. *et al.* 1.54μm Near-infrared photoluminescent and electroluminescent properties of a new Erbium (III) organic complex. *Organic Electronics* **9**, 487-494 (2008).

73 Martín-Ramos, P. *et al.* Charge Transport and Sensitized 1.5 μm Electroluminescence Properties of Full Solution-Processed NIR-OLED based on Novel Er(III) Fluorinated β-Diketonate Ternary Complex. *The Journal of Physical Chemistry C* **117**, 10020-10030 (2013).

74 Bünzli, J.-C. G. Lanthanide Luminescence for Biomedical Analyses and Imaging. *Chemical Reviews* **110**, 2729-2755 (2010).

75 Eliseeva, S. V. & Bünzli, J.-C. G. Lanthanide luminescence for functional materials and bio-sciences. *Chemical Society Reviews* **39**, 189-227 (2010).

76 Slooff, L. *et al.* Optical properties of erbium-doped organic polydentate cage complexes. *Journal of applied physics* **83**, 497-503 (1998).

77 Gillin, W. & Curry, R. Erbium (III) tris (8-hydroxyquinoline)(ErQ_3): A potential material for silicon compatible 1.5 μm emitters. *Applied physics letters* **74**, 798-799 (1999).

78 Hasegawa, Y., Wada, Y. & Yanagida, S. Strategies for the design of luminescent lanthanide (III) complexes and their photonic applications. *Journal of Photochemistry and Photobiology C: Photochemistry Reviews* **5**, 183-202 (2004).

79 Valeur, B. & Berberan-Santos, M. N. *Molecular fluorescence: principles and applications*. (John Wiley & Sons, 2013).

80 Köhler, A., Wilson, J. S. & Friend, R. H. Fluorescence and phosphorescence in organic materials. *Advanced Engineering Materials* **4**, 453 (2002).

81 Burrows, H. D. *et al.* S1～> T1 intersystem crossing in π-conjugated organic polymers. *The Journal of Chemical Physics* **115**, 9601-9606 (2001).

82 Wilson, J. *et al.* Spin-dependent exciton formation in π-conjugated compounds. *Nature* **413**, 828-831 (2001).

83 Reineke, S., Walzer, K. & Leo, K. Triplet-exciton quenching in organic phosphorescent light-emitting diodes with Ir-based emitters. *Physical Review B* **75**, 125328 (2007).

84 Wilkinson, F. & Abdel-Shafi, A. A. Mechanism of quenching of triplet states by molecular oxygen: Biphenyl derivatives in different solvents. *The Journal of Physical Chemistry A* **103**, 5425-5435 (1999).

85 Wilkinson, F., Helman, W. P. & Ross, A. B. Quantum yields for the photosensitized formation of the lowest electronically excited singlet state of molecular oxygen in solution. *Journal of physical and chemical reference data* **22**, 113-262 (1993).

86 Hertel, D., Bässler, H., Guentner, R. & Scherf, U. Triplet-triplet annihilation in a poly (fluorene)-derivative. *The Journal of Chemical Physics* **115**, 10007-10013 (2001).

87 Milián Medina, B., Beljonne, D., Egelhaaf, H.-J. & Gierschner, J. Effect of fluorination on the electronic structure and optical excitations of π-conjugated molecules. *The Journal of Chemical Physics* **126**, 111101 (2007).

88 Zhou, J., Liang, Q. & Dong, J. Enhanced spin-orbit coupling in hydrogenated and fluorinated graphene. *Carbon* **48**, 1405-1409 (2010).

89 Baldo, M., Thompson, M. & Forrest, S. High-efficiency fluorescent organic light-emitting devices using a phosphorescent sensitizer. *Nature* **403**, 750-753 (2000).

90 Curry, R., Gillin, W., Knights, A. & Gwilliam, R. 1.5 μm electroluminescence from organic light emitting diodes integrated on silicon substrates. *Optical Materials* **17**, 161-163 (2001).

91 Curry, R. & Gillin, W. Electroluminescence of organolanthanide based organic light emitting diodes. *Current Opinion in Solid State and Materials Science* **5**, 481-486 (2001).

92 Montes, V. A., Pohl, R., Shinar, J. & Anzenbacher, P. Effective Manipulation of the Electronic Effects and Its Influence on the Emission of 5-Substituted Tris (8-quinolinolate) Aluminum (III) Complexes. *Chemistry-A European Journal* **12**, 4523-4535 (2006).

93 Steemers, F. J., Verboom, W., Reinhoudt, D. N., van der Tol, E. B. & Verhoeven, J. W. New Sensitizer-Modified Calix[4]arenes Enabling Near-UV Excitation of Complexed Luminescent Lanthanide Ions. *Journal of the American Chemical Society* **117**, 9408-9414, (1995).

94 Hofstraat, J. W. *et al.* Near-IR Luminescent Rare Earth Ion–Sensitizer Complexes. *Journal of Fluorescence* **8**, 301-308, (1998).

95 Katkova, M. A. *et al.* Lanthanide imidodiphosphinate complexes: Synthesis, structure and new aspects of electroluminescent properties. *Synthetic Metals* **159**, 1398-1402 (2009).

96 Martín-Ramos, P. *et al.* Novel erbium (iii) fluorinated β-diketonate complexes with N, N-donors for optoelectronics: from synthesis to solution-processed devices. *Journal of Materials Chemistry C* **1**, 2725-2734 (2013).

97 Zheng, Y. *et al.* Near IR luminescent rare earth 3, 4, 5, 6-tetrafluoro-2-nitrophenoxide complexes: Synthesis, X-ray crystallography and spectroscopy. *Polyhedron* **27**, 1503-1510 (2008).

98 Zheng, Y., Pearson, J., Tan, R. H. C., Gillin, W. P. & Wyatt, P. B. Erbium bis(pentafluorophenyl)phosphinate: a new hybrid material with unusually long-lived infrared luminescence. *J Mater Sci: Mater Electron* **20**, 430-434 (2009).

99 Mech, A. *et al.* Sensitized NIR erbium (III) emission in confined geometries: A new strategy for light emitters in telecom applications. *Journal of the American Chemical Society* **132**, 4574-4576 (2010).

100 Snoeks, E., Kik, P. & Polman, A. Concentration quenching in erbium implanted alkali silicate glasses. *Optical Materials* **5**, 159-167 (1996).

101 Tan, R., Pearson, J., Zheng, Y., Wyatt, P. & Gillin, W. Evidence for erbium-erbium energy migration in erbium (III) bis (perfluoro-p-tolyl) phosphinate. *Applied Physics Letters* **92**, 103303 (2008).

102 Hernández, I., Tan, R. H. C., Pearson, J. M., Wyatt, P. B. & Gillin, W. P. Nonradiative De-excitation Mechanisms in Long-Lived Erbium(III) Organic Compounds $Er_xY_{1-x}[(p\text{-}CF_3\text{-}C_6F_4)_2PO_2]_3$. *The Journal of Physical Chemistry B* **113**, 7474-7481 (2009).

103 Winkless, L. *et al.* Quenching of Er(III) luminescence by ligand C-H

vibrations: Implications for the use of erbium complexes in telecommunications. *Applied Physics Letters* **89**, - (2006).

104 Van Deun, R., Fias, P., Driesen, K., Binnemans, K. & Görller-Walrand, C. Halogen substitution as an efficient tool to increase the near-infrared photoluminescence intensity of erbium (III) quinolinates in non-deuterated DMSO. *Physical Chemistry Chemical Physics* **5**, 2754-2757 (2003).

105 Ma, H., Jen, A. K.-Y. & Dalton, L. R. Polymer-based optical waveguides: materials, processing, and devices. *Advanced materials* **14**, 1339-1365 (2002).

106 Shin, J. H. *et al.* Si nanocluster sensitization of Er-doped silica for optical amplet using top-pumping visible LEDs. *Selected Topics in Quantum Electronics, IEEE Journal of* **12**, 783-796 (2006).

107 Han, H.-S., Seo, S.-Y. & Shin, J. H. Optical gain at 1.54 μm in erbium-doped silicon nanocluster sensitized waveguide. *Applied Physics Letters* **79**, 4568-4570 (2002).

108 Kik, P. & Polman, A. Gain limiting processes in Er-doped Si nanocrystal waveguides in SiO_2. *Journal of Applied Physics* **91**, 534-536 (2002).

109 Zhang, K. & Li, D. *Electromagnetic theory for microwaves and optoelectronics*. (Springer, 2008).

110 Palmer, C. A., Loewen, E. G. & Thermo, R. *Diffraction grating handbook*. (Newport Corporation Springfield, OH, 2005).

111 Li, Z. *et al.* Luminescent Zinc (II) Complexes of Fluorinated Benzothiazol-2-yl Substituted Phenoxide and Enolate Ligands. *Inorganic chemistry* **52**, 1379-1387 (2013).

112 Yu, G., Yin, S., Liu, Y., Shuai, Z. & Zhu, D. Structures, electronic states, and electroluminescent properties of a zinc (II) 2-(2-hydroxyphenyl) benzothiazolate complex. *Journal of the American Chemical Society* **125**, 14816-14824 (2003).

113 Li, Z. Fluorinated zinc and erbium complexes based on benzothiazole derived ligands for optoelectronic devices. *PhD Thesis* (2013).

114 Leach, S. J. & Scheraga, H. A. Effect of Light Scattering on Ultraviolet Difference Spectra1. *Journal of the American Chemical Society* **82**, 4790-4792 (1960).

115 Zakerhamidi, M. *et al.* Solvent Effects on the UV/Visible Absorption Spectra of Some Aminoazobenzene Dyes. *Chem. Sci. Trans* **1**, 1-8 (2012)

116 Ye, H. *et al.* Organo-erbium systems for optical amplification at telecommunications wavelengths. *Nature Materials* **13**, 382-386 (2014).

117 Jenouvrier, P., Langlet, M., Rimet, R. & Fick, J. Influence of crystallisation on the photoluminescence properties of $Y_{2-x}Er_xTi_2O_7$ sol-gel thin films. *Appl Phys A* **77**, 687-692 (2003).

118 Feng, X., Tanabe, S. & Hanada, T. Spectroscopic properties of erbium-doped ultraphosphate glasses for 1.5 μm amplification. *Journal of Applied Physics* **89**, 3560-3567 (2001).